

Department Chemie  
Technische Universität München

On the Mechanism of Photoinduced Electron  
Transfer in Bridged Donor/Acceptor Systems:  
Ferrocenophane/Nileblue and  
Rhodamine6G Endcapping the DNA Duplex

**Till von Feilitzsch**

Vollständiger Abdruck der von der Fakultät für Chemie der Technischen  
Universität München zur Erlangung des akademischen Grades eines

**Doktors der Naturwissenschaften**  
(Dr. rer. nat.)

genehmigten Dissertation.

Vorsitzende: Univ.-Prof. Dr. S. Weinkauff

Prüfer der Dissertation: 1. Univ.-Prof. Dr. M.-E. Michel-Beyerle, i. R.  
2. Univ.-Prof. Dr. H. J. Neusser

Die Dissertation wurde am 19.08.2004 bei der Technischen Universität München  
eingereicht und durch die Fakultät für Chemie am 14.09.2004 angenommen.



# Contents

<b>1</b>	<b>Introduction</b>	<b>5</b>
<b>2</b>	<b>Experimental Methods</b>	<b>11</b>
2.1	Time resolved spectroscopy . . . . .	11
2.1.1	Femtosecond pump / probe spectroscopy . . . . .	11
2.1.2	Time resolved fluorescence . . . . .	15
2.2	Steady state spectroscopy . . . . .	16
2.2.1	Absorption . . . . .	16
2.2.2	Fluorescence . . . . .	16
<b>3</b>	<b>Theoretical Basics</b>	<b>17</b>
3.1	Electron transfer theory . . . . .	17
3.1.1	Electronic coupling . . . . .	18
3.1.2	Franck-Condon factor . . . . .	20
<b>4</b>	<b>Picosecond Magnetic Field Effect</b>	<b>27</b>
4.1	The ferrocenophane-nileblue system . . . . .	28
4.1.1	Samples . . . . .	28
4.1.2	Structural calculations . . . . .	29
4.1.3	Spectroscopic characterisation . . . . .	29
4.1.4	Redox potentials . . . . .	31
4.1.5	EPR experiments . . . . .	32
4.2	Time resolved spectroscopy . . . . .	35
4.2.1	Forward electron transfer . . . . .	35
4.2.2	Back electron transfer and magnetic field dependence . . . . .	36
4.3	Analysis of the magnetic field effect . . . . .	38
4.3.1	Model . . . . .	38
4.3.2	Modeling the experimental data . . . . .	41
4.4	Mechanism of spin relaxation . . . . .	44
4.5	Mechanistic aspects of electron transfer . . . . .	46

4.5.1	Driving forces, ET-rates and their temperature dependence . . . . .	46
4.5.2	Interpretation of ET rates . . . . .	46
<b>5</b>	<b>Rhodamine labeled DNA</b>	<b>51</b>
5.1	Samples . . . . .	51
5.1.1	Dyes and buffers . . . . .	51
5.1.2	Oligomers and reference names . . . . .	52
5.1.3	Hybridisation and melting curves . . . . .	56
5.1.4	NMR-structure . . . . .	57
5.1.5	Spectroscopic characterisation . . . . .	60
5.1.6	Redox potentials and driving forces . . . . .	63
5.2	Different modes of kinetic experiments . . . . .	64
5.2.1	Assignment of difference absorbance signals . . . . .	64
5.2.2	Data analysis . . . . .	66
5.3	Excited state dynamics of R6 <sup>+</sup> free in solution . . . . .	67
5.3.1	Processes in excited state . . . . .	69
5.3.2	Dimer formation . . . . .	71
5.4	Kinetic characterisation of modified oligomers . . . . .	72
5.4.1	Femtosecond transient absorption spectroscopy . . . . .	72
5.4.2	Time resolved fluorescence experiments . . . . .	78
5.5	Results . . . . .	84
<b>6</b>	<b>Summary</b>	<b>91</b>
	<b>Bibliography</b>	<b>94</b>
	<b>List of publications</b>	<b>105</b>
	<b>Acknowledgements</b>	<b>107</b>

# Chapter 1

## Introduction

Electron transfer (ET) is one of the fundamental molecular reactions. While single step ET reactions are reasonably well understood [1–3], charge transport phenomena on the nanoscale are still subject both to experimental and theoretical study [4]. The understanding of processes on this scale is, however, very important for applications in molecular electronics, such as sensors, photonics and solar photoconversion [5].

In this work, two mechanistic aspects of ET reactions with donor–acceptor distances shorter than 15 Å are studied:

1. The influence of singlet–triplet spin conversion on the charge recombination process of a transition metal containing radical ion pair.
2. The distance dependence of guanine (G) and 7-deaza-guanine (Z) oxidation by photoexcited Rhodamine6G (R6<sup>+</sup>) covalently linked to the 5' end of a DNA duplex.

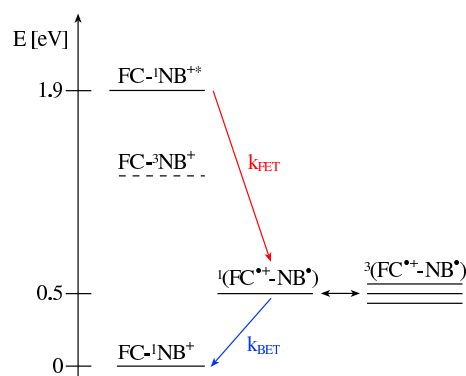
Both molecular systems have been studied by femto- to nanosecond time resolved spectroscopy in polar solvents. In both cases, the intramolecular ET systems undergo a charge shift reaction, where the influence of Coulomb interaction within the radical ion pair is minimal.

### Picosecond magnetic field effect

The spin states of electrons are conserved during photoinduced charge transfer. Consequently, when a radical ion pair is formed by a photoinduced ET process in the singlet manifold, the unpaired electrons in both radicals initially carry opposite spin. With increasing distance between the two radical ions the exchange energy becomes smaller, in other words, the Pauli exclusion principle is not fully applicable any more, and *spin relaxation* leads to an

increasingly isotropic distribution of the spin states of the two lonely radical electrons. This is reflected in an isotropic population of singlet and triplet states if the ion pair is regarded as a single supermolecule. In organic radical pairs, spin relaxation occurs on a  $\mu\text{s}$  time scale [6]; when transition metals are involved, this process can even occur on a ps time scale [7]. In addition to spin relaxation, different  $g$ -values for both radical ions lead to an oscillating population of the singlet and the  $T_0$  state of the supermolecule [8]. The frequency of this oscillation depends on an externally applied magnetic field. As a consequence of spin relaxation and singlet-triplet oscillation, the radical ion pair, which had purely singlet character when it was formed, gains more and more triplet character over time.

**Figure 1.1:** Magnetic field dependent reaction pathway for  $\text{FC} - \text{NB}^+$  after photoexcitation.



If only a singlet state can be reached by charge recombination for energetic reasons, spin relaxation leads to a delayed repopulation of the ground state as part of the molecules are in their non-reactive triplet state. If these processes (charge recombination and spin relaxation) and the oscillation between singlet and triplet states occur on the same time scale, back electron transfer (BET) kinetics are magnetic field dependent and spin relaxation can be measured optically with a high time resolution.

The nature of the spin relaxation process is discussed as being induced by fluctuations of the magnetic field correlated to the rotational relaxation of the molecule [7] or in terms of fluctuations of an electric field due to solvent fluctuations influencing the electron spin via spin orbit coupling [9].

A model was developed to describe spin relaxation and magnetic field effects on charge transfer processes [10], its applicability to a system with spin relaxation and ET dynamics on the ps time scale was demonstrated [11,12]. It was shown that the charge recombination kinetics in an intermolecular charge transfer system where the electron acceptor oxazine-1 ( $\text{OX}^+$ ) is dissolved in ethylferrocenium (**ethylFC**) is multiexponential and depends on magnetic fields up to 9 T. Application of the adapted model [13] allowed to extract

a single time constant for BET (1.3 ps) and for the spin relaxation process (6.5 ps).

## Charge injection into DNA

At the beginning of the 1990ies ET in DNA was subject to controversial discussion, as some experiments indicated almost distance independent charge transport in DNA [14–17], on one hand seemingly violating conventional ET theory, on the other hand giving rise to the hope of DNA acting as a “molecular wire” which would be of great interest for molecular electronics. Further theoretical [18] and experimental [19] work could explain the weak distance dependence as a consequence of a so-called “hopping”-mechanism allowing for long range hole transport via the easiest to oxidize nucleobase G.

The actual charge injection step, as studied utilising stilbene hairpin DNA sequences, shows an exponential decrease of the charge transfer rate  $k_{\text{ET}}$  with increasing donor/acceptor distance  $R$ , empirically described by an attenuation parameter  $\beta = 0.6 - 0.7 \text{ \AA}^{-1}$  [20, 21] with  $k_{\text{ET}} = k_0 e^{-\beta R}$ .

Experimental evidence of a much steeper distance dependence of charge injection into DNA reflected in attenuation parameters of  $\beta > 1.5 \text{ \AA}^{-1}$  for oxidation of G and Z by protonated 9-amino-6-chloro-2-methoxyacridine (ACMA,  $\text{X}^+$ ) [22, 23] lead to the conclusion that in addition to the electronic coupling, the activation energy  $E_a$  must also be distance dependent [23, 24]. It is well known, that distance dependent activation energies may arise from the distance dependence of both the driving force  $\Delta G$  and the reorganisation energy  $\lambda$  on purely electrostatic grounds [1, 25]. An important simplification for the  $\text{X}^+$  system is that for charge shift reactions,  $\Delta G$  is expected to have little or no distance dependence, in contrast to charge separation reactions. Therefore, the distance dependence of  $E_a$  for charge shift reactions should be due solely to the distance dependence of  $\lambda$ .

In the present work, the distance dependence of charge injection into a second DNA system is investigated, where  $\text{R6}^+$  is expected to spontaneously endcap the DNA duplex. In this case the distance dependence of  $\lambda$  should be larger than for intercalated systems as the system is more exposed to the polar solvent environment. Endcapping charge injectors have a principle advantage above intercalated charge injectors, as they do not disturb the DNA base stack (Figure 1.2).

## Goals of this dissertation

The novel covalently bridged ferrocenophane-nileblue (FC –  $\text{NB}^+$ ) compound [26, 27] is studied in transient absorption experiments in a high magnetic field

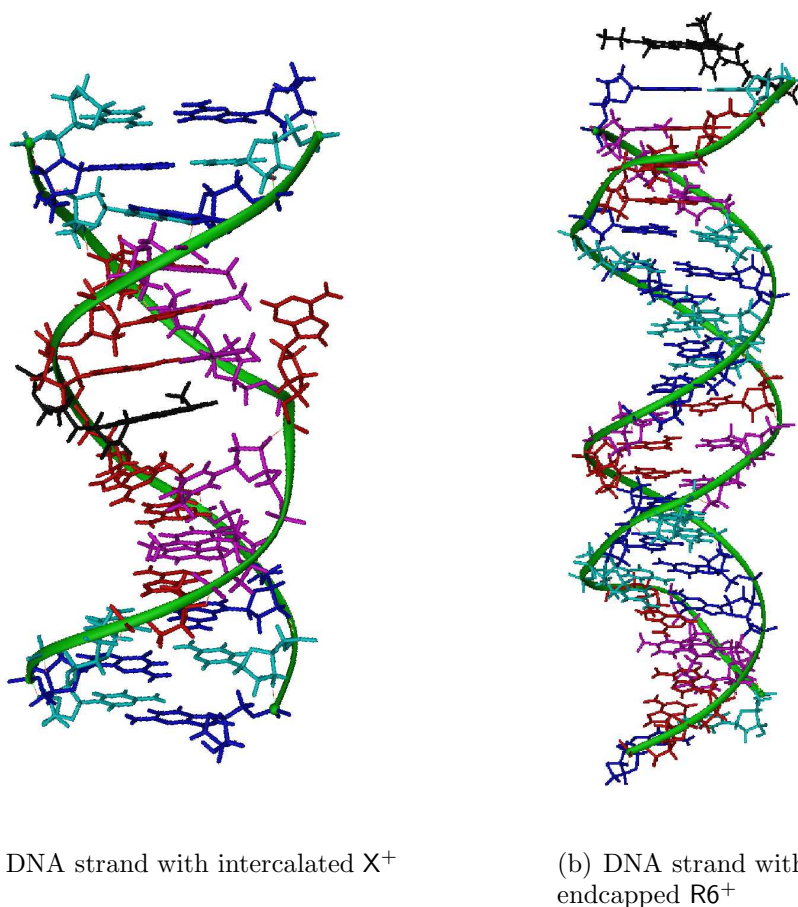


**Figure 1.2:** NMR structure of DNA strands. Color code: dye, G, C, A, T

of up to 7 T. These experiments are presented in Chapter 4 where following issues are addressed:

1. The mechanism of spin relaxation is investigated, based on the temperature dependence of the spin relaxation rate.
2. The nature of the ET processes is investigated, based on an estimate of the driving forces for FET and BET derived from cyclic voltammetry and on the ET rates as a function of temperature.

A series of DNA duplexes with end-capped  $R6^+$  is investigated by transient absorption and fluorescence experiments and discussed under following aspects in Chapter 5:



1. The distance dependence of charge injection is studied comparing ET rates for duplexes with the potential hole acceptor **G** and easier to oxidize **Z** in nearest neighbour position to excited  $R6^{+*}$  and with one and two intermittant **A : T** base pairs.
2. The charge injection pattern is dicussed on the basis of NMR structures on identical modified DNA sequences.

Conclusions from the experiments on both systems are drawn in Chapter 6.



# Chapter 2

## Experimental Methods

### 2.1 Time resolved spectroscopy

#### 2.1.1 Femtosecond pump / probe spectroscopy

##### Principles of transient difference absorption spectroscopy

In transient difference absorption spectroscopy the changes of the absorbance of a sample as a function of time after excitation by a short pump pulse are measured by a second probe pulse (pump / probe). Information on the kinetics is gained by probing at different time intervals after excitation.

Absorption of the sample is measured by a low intensity probe pulse without ( $A(\lambda)$ ) and with ( $A^*(\lambda)$ ) prior excitation by a pump pulse as a function of the probe beam intensity before ( $I_0$ ) and behind ( $I$ ) the sample. According to Lambert–Beer’s law, both  $A(\lambda)$  and  $A^*(\lambda)$  are proportional to the molar extinction coefficient  $\varepsilon_i$  and the concentration  $c_i$  of photoactive species  $i$ , if where reabsorption and saturation effects are small.

$$\begin{aligned} A(\lambda) &= -\log\left(\frac{I}{I_0}\right) \\ &= \sum_i \varepsilon_i(\lambda)c_i l \end{aligned} \tag{2.1}$$

$A^*(\lambda)$ , and thus the concentration of photoactive species and their transient evolution after excitation, can be followed for various time delays  $\Delta t$  between photo–excitation of the sample and arrival of the probe pulse at the sample. The change of absorbance, or difference absorbance,

$$\begin{aligned}\Delta A(\lambda, \Delta t) &= A^*(\lambda, \Delta t) - A(\lambda) \\ &= l \sum_i \varepsilon_i(\lambda)(c_i^* - c_i)\end{aligned}\tag{2.2}$$

is the usual measure in transient absorption experiments and is influenced by several processes:

**Excited state absorption** Depending on the excitation probability, the concentration of the excited state is higher after  $c_i^*$  than before  $c_i$  excitation and  $(c_i^* - c_i)$  becomes positive. The positive signal due to excited state absorption decays with the lifetime of the excited state.

**Product absorption** If, originating from the excited state, products (e.g. radicals in case of charge transfer reactions) are formed after excitation, they also give rise to a positive difference absorbance signal. The kinetics of the signal can show rise and decay characteristics of this product.

**Ground state bleaching** Excitation reduces the concentration of the chromophore in its ground states (“bleaching”), thus  $(c_i^* - c_i)$  becomes negative. Consequently the repopulation of the ground state can be detected as the recovery of a negative ground state bleaching signal.

**Stimulated emission** If a chromophore is in its excited state, and a photon of the subsequent probe pulse matches the  $S_{1 \rightarrow 0}$  transition energy, it can force the chromophore back to its ground state while a second photon with the same energy and in phase with the first (probe) photon is emitted (“stimulated emission”).

In terms of quantum physics, absorption of a photon inducing a transition of the chromophore from its ground state  $|1\rangle$  to its excited state  $|2\rangle$  is proportional to the Einstein  $B_{12}$  coefficient, the number of chromophores in state  $|1\rangle$  ( $N_1$ ) and the number of photons in resonance with the energy gap  $E_{12}$  between  $|1\rangle$  and  $|2\rangle$ . Stimulated emission from state  $|2\rangle$  is treated equivalently with the Einstein  $B_{21}$  coefficient and is proportional to the number of chromophores in state  $|2\rangle$  ( $N_2$ ) and also to the number of photons in resonance with the energy gap  $E_{12}$ . As a consequence, stimulated emission can be treated in parallel to absorption from product states, only with a negative “extinction” coefficient, since one photon is emitted in addition to the incident photon

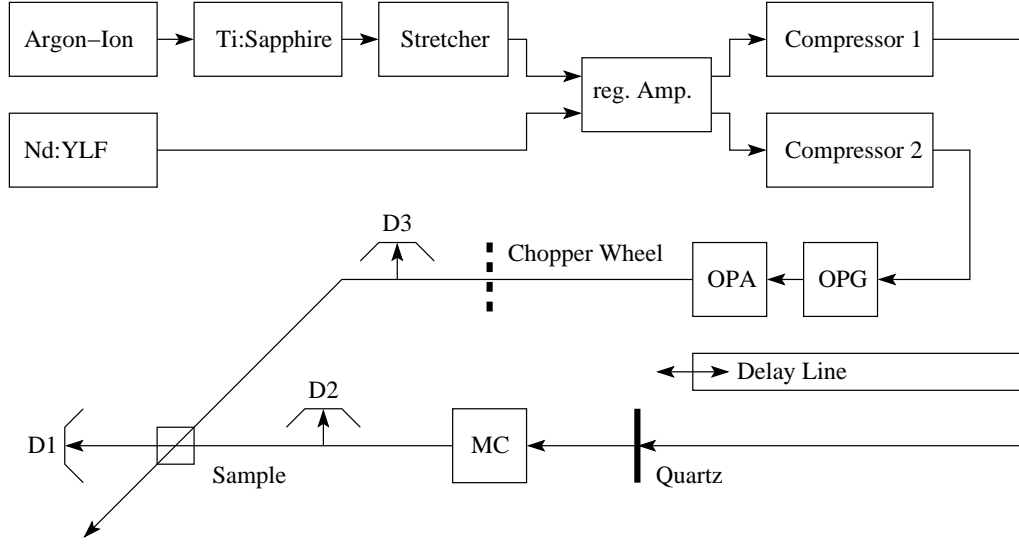


**Figure 2.1:** fs-absorption setup as described in the text

instead of being absorbed. In particular, stimulated emission is proportional to the concentration of the chromophore in its excited state. As the concentration of the excited state increases upon excitation and  $(c_i^* - c_i)$  becomes positive, the “negative extinction coefficient” leads to a negative signal and stimulated emission can be used to monitor the population of the excited state.

The spectral characteristics of stimulated emission and fluorescence are closely related, as the Einstein  $A_{21}$  coefficient for spontaneous emission (fluorescence) can be expressed as a function of  $B_{21}$ :

$$A_{21} = \frac{8\pi h}{\lambda^3} B_{21} \quad (2.3)$$

### Femtosecond transient absorption setup

Most time resolved absorption experiments were performed with a setup extensively described in [28, 29]. In this section a short overview on the setup is given as well as on the integration of a superconducting magnet.

A setup containing a regenerative amplifier is suitable to achieve the short and intense light pulses needed to gain the high photon flux density needed in the OPG (optical parametric generation) stage. In this system a Titan:Sapphire laser (Coherent MIRA 900 F Basic) pumped with 7.5 W by an Argon-Ion laser (Coherent Innova 310) is typically operated at a central

wavelength of 780 nm, a pulse width of 80 fs (FWHM, full width at half maximum) and at a repetition rate of 76 MHz. Before amplification, the pulses are stretched by a factor of 1000. The amplifier (B.M.I. Alpha-S/P-1000) is pumped by a synchronized 1 kHz Nd:YLF laser (B.M.I. 621.D) with a pulsewidth of about 200 ns at 10 W and seeded by the stretched pulses from the Titan:Sapphire laser. After amplification, the beam has an intensity of approximately 1.3 W and a repetition rate of 1 kHz. These pulses are split at an intensity ratio of 30:1 to yield separate pump and probe pulses, and afterwards compressed.

The pump pulse is frequency doubled by a quartz plate and focused into a two-stage optical parametric generation (OPG) and amplification (OPA) device. This allows to tune the wavelength from little more than 450 nm up to about 2000 nm with sufficient intensity for difference absorption measurements. After the OPA stage, the intensity is typically around 10 mW at 500 nm. A chopper wheel is used to block every second pulse in order to allow comparison of the absorbance from the excited and unexcited sample.

The probe pulse can be delayed in time with respect to the pump pulse on a 1.5 m delay line, opening an accessible time window of 5 ns. After the delay line, a white light continuum reaching from 450 nm into the infrared region is generated in a quartz plate. The wavelength needed for the experiment can be selected by a monochromator (MC).

The angle between pump and probe beam at the point where they intersect in the sample was minimized ( $\approx 10^\circ$ ). This leads to a larger overlap between both beams in the sample. To eliminate influences by rotational depolarisation processes in the sample, the angle between the polarisation axis of the pump and probe pulse was set to  $54.7^\circ$  (“magic angle”).

The light intensity of the probe pulses before (D2) and after (D1) the sample as well as the intensity of the pump pulses (D3) was measured by photodiodes with rise characteristics of 2 ns using the so called gated integrator technique. The signals of the diodes are only recorded during a time window of  $\approx 100$  ns around the expected arrival of the light pulses and then digitized. This technique allows a very high signal to noise ratio.

The time resolution of the setup is limited by the duration of the pump and probe pulses and varies between 150 fs and 200 fs depending on the wavelengths for pumping and probing.

### **Superconducting magnet**

To perform magnetic field dependent experiments at high fields larger than 1 T, a liquid helium cooled superconduction magnet (SM-4000-9, Oxford Instruments) was included in the fs transient absorption setup. In order to

decrease influences on the optical setup by the high magnetic field, the use of paramagnetic material was reduced to a minimum within a radius of 1.5 m around the magnet. To further decrease influences of the magnetic field on the optical elements close to the magnet a  $\mu$ -metal shield was used. A very sensitive test for the influence of the magnetic field onto the optical elements is the overlap of the pump and probe beam and thus the difference absorbance signal at  $t = 0$ . Between 0 T and 7 T, the overlap had not to be readjusted.

## 2.1.2 Time resolved fluorescence

### Time correlated single photon counting

Time resolved fluorescence experiments were performed with a time correlated single photon counting (TCSPC) setup described in [30,31]. With this technique, fluorescence decay is measured by recording the time delay between excitation of the sample and the arrival of a single emitted photon at the detector. Excitation is attenuated so that typically only one photon per 100 excitation pulses is recorded. Accumulation of these signals yields a histogram reflecting the time dependence of the fluorescence signal.

The sample is photoexcited by a Ti:Sapphire oscillator (Coherent Mira) pumped with 8 W by an Argon-Ion laser (Coherent Innova 310). Depending on the mirror set in the Ti:Sapphire oscillator, its emission wavelength can be tuned from 720 nm to 900 nm. The output power is typically around 700 mW at a repetition rate of 76 MHz (1 pulse per 13 ns) and a pulsewidth of 80 fs. This is equivalent to an energy of about 100 kJ/pulse. For experiments on samples absorbing in the visible region, the pulses are frequency doubled. To allow experiments on samples with lifetimes not much shorter than the duration between the laser pulses from the Ti:Sapphire laser, a pulse picker was included, reducing the repetition rate to 3.8 MHz (1 pulse per 260 ns).

The detection wavelength is selected by two double grid monochromators (Jobin Yvon H10); the polarisation axis of the monitored emitted light is selected by a thin film polariser. Unless for fluorescence depolarisation experiments, the angle between the polarisation of detection and excitation is set to  $54.7^\circ$  (“magic angle”) to suppress influences of rotational depolarisation. In order to determine rotational depolarisation time constants, this angle can be set to parallel or perpendicular mode.

The time resolution is in the order of 30 ps and limited by electronic response. For each experiment, the apparatus response function is recorded as the response of the scattering signal. During data analysis, this response function is used to deconvolute the recorded decay of fluorescence.

**Fluorescence depolarisation:** Absorption probability of polarised light

depends on the angle between the polarisation axis of the excitation beam and the transition dipole moment for absorption fixed to the coordinate system of a chromophore. Consequently, excitation with polarised light induces anisotropy. The emission dipole moment for fluorescence is collinear with the absorption dipole moment with respect to the chromophore, allowing to measure the photoinduced anisotropy of the sample by observing fluorescence light parallel ( $I_{\parallel}$ ) and perpendicular ( $I_{\perp}$ ) to the polarisation axis of the excitation beam. The decay of the fluorescence signal  $r$

$$r = \frac{I_{\parallel} - I_{\perp}}{I_{\parallel} + 2I_{\perp}} \quad (2.4)$$

is a measure for rotational diffusion of the chromophore.

## 2.2 Steady state spectroscopy

### 2.2.1 Absorption

Steady state absorption measurements were performed on commercially available systems, either on a Perkin Elmer Lambda 2S or a Varian Cary 100 Bio. The spectral resolution of both systems is 2 nm or better.

### Melting points

To record melting curves especially of DNA samples, the Varian spectrometer is equipped with a temperature control unit allowing to determine absorption of the sample in a temperature range of  $-5^{\circ}\text{C}$  to  $100^{\circ}\text{C}$ . The temperature of the sample can be varied by Peltier elements at a rate of up to 1 K/s and monitored by a thermoelement in a reference cuvette. The melting temperatures ( $T_m$ ) of the oligonucleotides are determined as the inflexion points of the melting curves.

### 2.2.2 Fluorescence

Fluorescence emission and excitation spectra were recorded with a “Fluorolog-2” fluorimeter (Spex). The spectral resolution strongly depends on the width of the entrance and exit slits of the first and second monochromator. Typically, the spectral resolution is better than 1.7 nm, unless the fluorescence signal is at the limit of sensitivity of the apparatus.



# Chapter 3

## Theoretical Basics

### 3.1 Electron transfer theory

Electron transfer (ET) is one of the most important types of elementary reactions in chemical and biological systems and is covered in literature in great detail [1–3, 32–35].

ET can be described as a transition of a “supermolecule” consisting of an electron donor **D**, an electron acceptor **A** and the surrounding medium. To describe the charge separation process in this supermolecule the Born-Oppenheimer approximation is applied: Due to the large difference in mass between electrons and nuclei, processes referring to electrons can be well separated from nuclear motion. In other words, nuclear wavefunctions can be separated from electronic wavefunctions. In addition, it is assumed that the electronic configuration reacts instantly on a change of the nuclear configuration (Franck-Condon principle). The initial state  $a = (\text{D}^*\text{A})$  and the charge separated state  $b = (\text{D}^+\text{A}^-)$  of the supermolecule can be described as follows:

$$\begin{aligned} |a\nu\rangle &= \Psi_a(r, q)\chi_{a\nu}(q) \\ |b\omega\rangle &= \Psi_b(r, q)\chi_{b\omega}(q) \end{aligned} \tag{3.1}$$

where  $\Psi$  and  $\chi$  are electronic and nuclear wavefunctions,  $r$  and  $q$  electronic and nuclear coordinates;  $\nu$  and  $\omega$  two sets of vibrational quantum numbers. The electronic states  $a$  and  $b$  can be described by multidimensional potential surfaces  $U_a(q)$  and  $U_b(q)$  mainly dependent on a generalised nuclear reaction coordinate  $q$  of the system.

### 3.1.1 Electronic coupling

ET is induced by coupling between the two states<sup>1</sup> with an exchange interaction  $V_{av,b\omega}$ :

$$V_{av,b\omega} = \iint \Psi_a^*(r, q) \chi_{av}^*(q) \hat{V} \Psi_b(r, q) \chi_{b\omega}(q) dq dr \quad (3.2)$$

$\hat{V}$  couples every vibronic substate of the initial state  $|a\nu\rangle$  with an energy  $E_{|a\nu\rangle}$  to a multiplicity of vibronic charge separated states  $\{|b\omega\rangle\}$  and energies  $E_{|b\omega\rangle}$ , which are quasi-degenerate with the initial state.

The electronic transition takes place instantly without change of nuclear coordinates (Born-Oppenheimer approximation); the electronic wave function depends only weakly on the nuclear coordinates (Franck-Condon principle). The double integral in equation (3.2) can then be separated:

$$\begin{aligned} V_{av,b\omega} &= \langle a\nu | \hat{V} | b\omega \rangle \\ &= \langle \Psi_{a,\nu}(r, q) | \hat{V} | \Psi_{b,\omega}(r, q) \rangle \langle \chi_{a,\nu} | \chi_{b,\omega} \rangle \\ &\approx V \langle \chi_{a,\nu} | \chi_{b,\omega} \rangle \end{aligned} \quad (3.3)$$

For ET reactions, only the overlap of nuclear wavefunctions and electronic coupling is relevant. Depending on the magnitude of the electronic coupling  $V$  two limiting cases can be separated:

1. For large  $V$ , the potential surfaces are disturbed strongly in the region of transition, so that the potential surfaces for the initial and product state cannot be separated any more and an adiabatic transition from  $U_a(q)$  to  $U_b(q)$  takes place.
2. For smaller  $V$  the states of ( $D^*A$ ) and ( $D^+A^-$ ) do not effectively mix any more. A transition between the potential surfaces  $U_a(q)$  to  $U_b(q)$  is a statistical process depending on how often the point of intersection is reached, and on the transition probability proportional to  $V^2$ .

Long range ET processes with  $D - A$  distances larger than their van-der-Waals distance can usually be described in the framework of non-adiabatic theory and two regimes for the electronic coupling can be separated.

**Direct coupling** If only the tails of the electronic wavefunctions contribute to the overlap integral, the matrix element for electronic coupling can be approximated by an exponential distance dependence:

---

<sup>1</sup>one electron two-center exchange interaction

$$V(R) = V_0 e^{-\beta R} \quad (3.4)$$

where  $R$  is the mean distance between donor and acceptor. The attenuation parameter  $\beta$  is an empirical constant which is, according to studies on the distance dependence of ET processes in the order of  $\beta \approx 0.6^{-1}$  in DNA [20] with higher values for short range processes [22,23]. The pre-exponential factor  $V_0$  depends on the form of the wave function and the orientation of the D and A molecules towards each other. Even though the expression contains no explicit temperature dependence, the value of the electronic coupling can change due to temperature dependent conformational changes.

**Superexchange coupling** If a molecular bridge **B** is located between **D** and **A**, the interaction between **D** and **A** can be drastically increased by mixing of **B** states into the donor-acceptor coupling. [36,37]. In this “superexchange” model, the states of **B** are only virtually occupied; therefore also energetically higher states can influence the exchange interaction. First order perturbation theory adds a second contribution  $V_{SE}$  to the direct coupling  $V_{dir}$ :

$$V = V_{dir} + V_{SE} = V_{dir} + \frac{V_{DB}V_{BA}}{\delta E_B} \quad (3.5)$$

The energy gap between the potential surface of *B* and the point of intersection of the potential surfaces of **D** and **A** enters the equation as  $\delta E_B$ . For large **D** – **A** distances, the superexchange contribution can exceed direct coupling by far.

In the framework of non-adiabatic ET, the transition from the initial state  $|a\nu\rangle$  to a multiplicity of charge separated states  $\{|b\omega\rangle\}$  can be treated with first order perturbation theory. The microscopic transition rate  $k_{|a\nu\rangle \rightarrow \{|b\omega\rangle\}}$  can be derived from Fermi’s Golden Rule:

$$k_{|a\nu\rangle \rightarrow \{|b\omega\rangle\}} = \frac{2\pi}{\hbar} \sum_{\omega} |V_{a\nu,b\omega}|^2 \delta(E_{b\omega} - E_{a\nu}) \quad (3.6)$$

The  $\delta$  function ensures energy conservation between reactant and product states with energies  $E_{a\nu}$  and  $E_{b\omega}$ .

Due to vibronic excitation, ET transfer does not originate from a single state  $|a\nu\rangle$ , consequently also the reactant state has to be treated as a multiplicity. Within this multiplicity relaxation takes place on a typical time

scale of 100 fs up to a few ps. If this relaxation is fast compared to ET reaction, the ET rate  $k$  can be regarded as a weighted sum of the microscopic rates described in equation 3.6:

$$k = \sum_{\nu} \rho_{\nu} k_{|a\nu\rangle \rightarrow \{|b\omega\rangle\}} \quad (3.7)$$

with

$$\rho_{\nu} = \frac{e^{-\frac{E_{a\nu}}{k_B T}}}{\sum_{\nu} e^{-\frac{E_{a\nu}}{k_B T}}} \quad (3.8)$$

where  $\rho_{\nu}$  represents the thermal occupation of the reactant's vibronic states. The macroscopic transition rate in equation 3.7 can also be written as:

$$k = \frac{2\pi}{\hbar} |V|^2 \text{FC} \quad (3.9)$$

with a thermally averaged Franck-Condon factor FC:

$$\text{FC} = \sum_{\nu} \sum_{\omega} \rho_{\nu} |\langle \chi_{a,\nu} | \chi_{b,\omega} \rangle|^2 \delta(E_{b\omega} - E_{a\nu}) \quad (3.10)$$

The transition rate for non-adiabatic ET as in equation (3.9) depends on the product of the squared electronic transition matrix element and the Franck-Condon factor as a thermal mean of the overlap of the nuclear wave functions.

### 3.1.2 Franck-Condon factor

The Franck-Condon factor describes the response of the nuclear configuration to the ET process with a changed equilibrium situation. It takes into account the vibrational state of the system including the surrounding solvent.

#### Single mode approximation

In single mode approximation all vibrational states of the reactant ( $\text{D}^*\text{A}$ ) and the charge separated product ( $\text{D}^+\text{A}^-$ ) are summarized as a single mode with a mean frequency  $\omega$ . The multi dimensional potential surfaces of both states can then be reduced to one dimension and approximated by square potential wells and describe two parabolas:

$$\begin{aligned} U_a(q) &= \frac{\hbar\omega}{2} q^2 \\ U_b(q) &= \frac{\hbar\omega}{2} (q - \Delta)^2 + \Delta G \end{aligned} \quad (3.11)$$

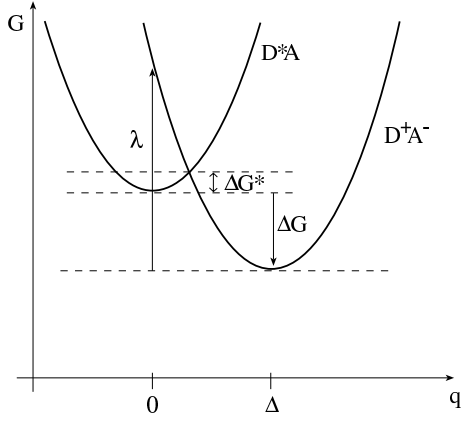


**Figure 3.1:** One dimensional representation of potential energy surfaces for reactant  $D^*A$  and product  $D^+A^-$  state as a function of the (nuclear) reaction coordinate  $q$

$\Delta$  is the value of the generalised reaction coordinate  $q$  for the equilibrium situation the product, assuming  $q = 0$  at equilibrium of the reactant. The difference between the free enthalpies in the potential minimum for both states is the driving force  $\Delta G$ , which is negative for exoergic reactions. The difference in energy of the product at the point of equilibrium of the reactant  $U_b(0)$  and at its own point of equilibrium  $U_b(\Delta)$  is the reorganisation energy  $\lambda$ :

$$\lambda = \frac{\hbar\omega}{2}\Delta^2 \quad (3.12)$$

As a consequence of the Franck-Condon principle the actual change between the potential energy surfaces has to occur at fixed nuclear coordinates (vertical transition). As the transition is radiationless, energy remains conserved (horizontal transition). Both conditions are only met simultaneously at the point of intersection of the parabolas. From this consideration the activation energy can be derived:

$$E_A = \frac{(\Delta G + \lambda)^2}{4\lambda} \quad (3.13)$$

In single mode approximation the Franck-Condon factor in equation (3.10) can be given in an analytical form [3]:

$$FC = \frac{1}{\hbar\omega} e^{-S(2\nu+1)} I_p(2S\sqrt{\nu(\nu+1)}) \left(\frac{\nu+1}{\nu}\right)^{\frac{p}{2}} \quad (3.14)$$

with modified Bessel functions  $I_p$  of the order  $p$  and the dimensionless parameters

$$S = \frac{\Delta^2}{2} = \frac{\lambda}{\hbar\omega}$$

$$p = \frac{|\Delta G|}{\hbar\omega} \quad (3.15)$$

and the temperature dependent Bose factor  $\nu = (e^{\hbar\omega/k_B T} - 1)^{-1}$ .

At low temperatures ( $k_B T \ll \hbar\omega$ ), equation (3.14) can be reduced to:

$$\text{FC} = \frac{1}{\hbar\omega} e^{-S} \left( \frac{S^p}{p!} \right) \quad (3.16)$$

describing temperature independent tunneling from the lowest vibrational reactant state to the isoenergetic vibrational product state.

For high temperatures ( $k_B T \gg \hbar\omega$ ), equation (3.14) evolves to the so-called Marcus relation:

$$\text{FC} = \frac{1}{\sqrt{4\pi k_B T}} e^{-E_a/k_B T} \quad (3.17)$$

This reflects the classical Arrhenius type temperature dependence with  $E_a$  as in equation (3.13). The limit between high and low temperature treatment is at  $k_B T \approx \hbar\omega/4$  [38]. For vibrational frequencies of  $100 \text{ cm}^{-1}$  to  $300 \text{ cm}^{-1}$  this corresponds to a range from 35 K to 100 K.

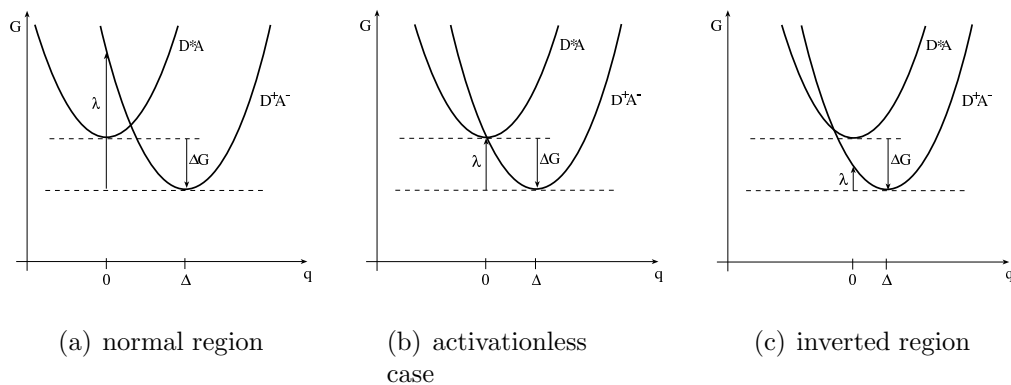


**Figure 3.2:** Relative position of potential energy surfaces for the three different relations of  $\Delta G$  and  $\lambda$

In the framework of high temperature approximation, three different regimes can be separated depending on the relative position of the reactant's and product's potential surfaces:

1. The so-called “normal” region with  $-\Delta G < \lambda$ , where the electron transfer rate  $k_{\text{ET}}$  increasing with temperature and the absolute value of the driving force.

2. The activationless case with  $-\Delta G = \lambda$ , where the ET rate is almost temperature independent.
3. The “inverted” region with  $-\Delta G > \lambda$ , where, counter-intuitively, the electron transfer rate decreases while absolute value of the driving force increases.

**Driving force** The driving force  $\Delta G$  for a photoinduced ET reaction can be estimated applying the Rehm-Weller formalism [39]. The primary ET process originating from the photoexcited state ( $(D^*A) \rightarrow (D^+A^-)$ ) depends on the  $E_{0,0}$  transition energy, the electrochemical potentials of the ET partners  $E^0(D/D^{+\bullet})$  and  $E^0(A/A^{-\bullet})$  as well as on a Coulomb term  $E_{\text{Coulomb}}$ :

$$\Delta G_{\text{FET}} = E^0(D/D^{+\bullet}) - E^0(A/A^{-\bullet}) - E_{0,0} + E_{\text{Coulomb}} \quad (3.18)$$

Under the assumption that the product ions are spherical with radii  $r_D$  and  $r_A$  the Coulomb energy change resulting from ET over a  $D - A$  distance  $R$  can be estimated with

$$E_{\text{Coulomb}} = \frac{e^2}{8\pi\epsilon_0} \left( \frac{1}{2r_D} + \frac{1}{2r_A} - \frac{1}{R} \right) \left( \frac{1}{\epsilon} - \frac{1}{\epsilon_{\text{Ref}}} \right) - \frac{q^2}{4\pi\epsilon_{\text{Ref}}\epsilon_0 R} \quad (3.19)$$

where  $\epsilon$  is the dielectric constant of the medium and  $\epsilon_{\text{Ref}}$  the static dielectric constant of the solvent used to measure  $E^0(D/D^{+\bullet})$  and  $E^0(A/A^{-\bullet})$  [40]. The last term in equation (3.19) is the Coulomb stabilization of the product ions and the second to last term arises from the separation-distance-dependent solvation energy of the ion pair.

It follows from equation (3.19) that for a charge shift reaction originating from  $A^{+*}$ , as it is the case for all ET reactions covered in this work, and donor and acceptor molecules of similar size and in similar environments, the distance dependence of  $\Delta G$  can be neglected [41].

**Reorganisation energy** From Figure 3.1 a physical meaning of the reorganisation energy can be deduced:  $\lambda$  is the change in free energy required for the (atomic structure of the) system to react on the new charge distribution induced by the ET process.  $\lambda$  contains contributions from the vibrations of the molecules (inner-sphere or intramolecular reorganisation energy  $\lambda_v$ ) and from the polarization changes in the

dielectric solvent environment (outer-sphere or medium reorganisation energy  $\lambda_s$ ).

$$\lambda = \lambda_v + \lambda_s \quad (3.20)$$

The standard estimate for the latter was obtained by R. Marcus applying a model in which reactants and products were modeled as conducting spheres and the medium as a dielectric continuum [42]:

$$\lambda_s = \frac{e^2}{4\pi\epsilon_0} \left( \frac{1}{2r_D} + \frac{1}{2r_A} - \frac{1}{R} \right) \left( \frac{1}{\epsilon_{\text{optical}}} - \frac{1}{\epsilon_s} \right) \quad (3.21)$$

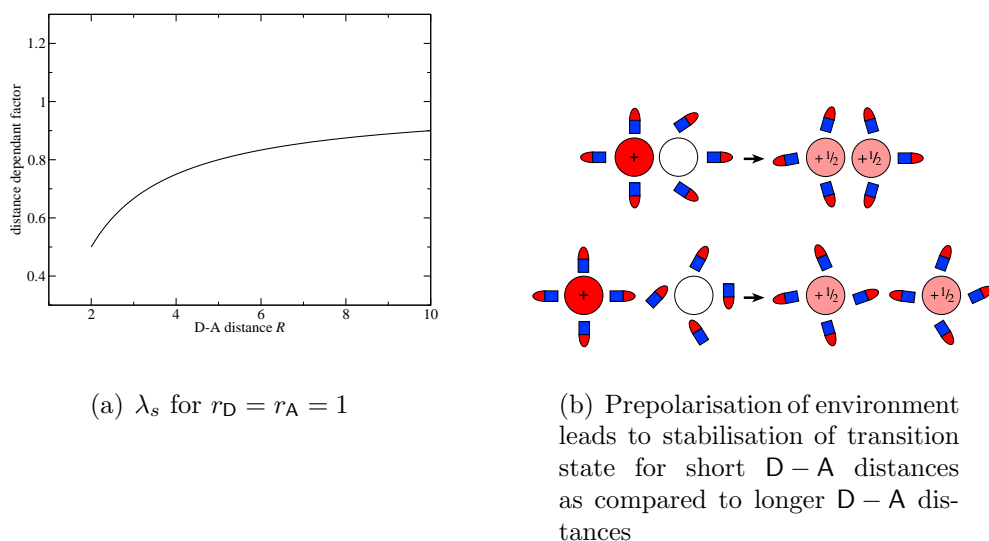


**Figure 3.3:** Influence of D – A distance on the reorganisation energy

In this equation  $\epsilon_{\text{optical}}$  and  $\epsilon_s$  are the optical frequency and the static dielectric constant of the medium. The difference in the inverse dielectric constants (Pekar factor) relates to the fact that nuclear degrees of freedom cannot readjust instantaneously to the motion of the electrons, a manifestation of the Born-Oppenheimer approximation [42]. Notably, for D – A distances in the range of the radii of D and A, the distance dependence of  $\lambda_s$  is rather strong, while at larger distances, this effect can be neglected (Figure 3.3).



### Multi mode approximation

The vibrational pattern of complex molecules is only described roughly by single mode approximation. In multi mode approximation, in addition to a mean low frequency mode, a second - also averaged - high frequency mode is considered. The ET process is now also allowed to the  $n$ th vibrational state ( $D^+A^-$ ) <sub>$n$</sub>  of this high frequency mode. The driving force ( $-\Delta G$ ) for these reactions is then lower by  $n\hbar\omega$  as compared to ET to the lowest vibrational state of the product. The Franck-Condon factor in the high temperature case in this model is [3]:

$$FC = \frac{1}{\sqrt{4\pi\lambda_s k_B T}} e^{-S_\nu} \sum_n \frac{S_\nu^n}{n!} e^{-\frac{(\Delta G + \lambda_s + n\hbar\omega)}{4\lambda_s k_B T}} \quad (3.22)$$

with the so-called Huang-Rhys factor

$$S_\nu = \lambda_i \hbar\omega \quad (3.23)$$

In this equation,  $\lambda_s$  denotes the (low frequency) solvent reorganisation energy, high frequency intramolecular vibrations enter the Franck-Condon factor via  $\lambda_i$ . The Huang-Rhys factor describes the electron phonon coupling of the high frequency mode. For small coupling  $S_\nu$  tends to zero and the Franck-Condon factor meets the Marcus relation for single mode approximation as in equation (3.17).

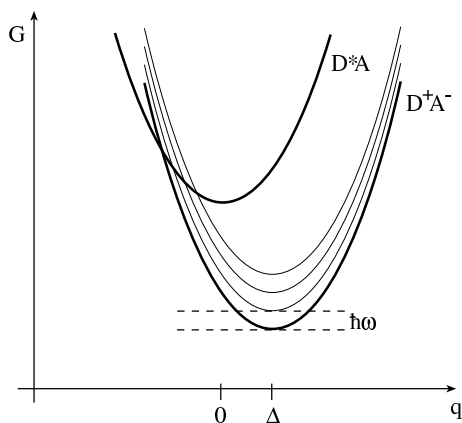


**Figure 3.4:** High frequency modes in the Marcus inverted region

In the normal Marcus region and in the activationless case, the activation energy for transitions into higher vibronic states is higher as for the lowest vibrational product state. Consequently, the ET rates are comparable in multi mode and single mode approximation. This is not the case in the Marcus inverted region. Here, the transitions to higher vibrational product states are subjected to a decreased activation energy. Therefore, in the inverted region,

the treatment in multi mode approximation yields higher ET rates than in single mode approximation. Additionally, the dependence of the rate on the driving force and on temperature is lower than in single mode approximation.

# Chapter 4

## Picosecond Magnetic Field Effect

Magnetic field effects on the kinetics of radical pair (RP) recombination processes are well-established phenomena in molecular photo-chemistry [43]. These effects are based on the principle of spin conservation in elementary chemical reactions and on the hyperfine and Zeeman interactions affecting spin states of the RP. The hyperfine interaction in organic RPs induces transitions between the RP's spin states (one singlet  $S$  and three triplet states  $T_+$ ,  $T_0$  and  $T_-$ ). In an external magnetic field the Zeeman splitting removes degeneracy of two triplet levels ( $T_+$  and  $T_-$ ) with the singlet state, thus reducing singlet–triplet mixing. The saturation field of such effects is determined by the magnitude of the hyperfine interaction, which is  $\sim 0.005$  T in organic RPs. This field range also determines the time scale for these effects to evolve ( $\sim 10$  ns) [6, 44]. In this regime, magnetic field effects have been successfully used to separate spin processes and elementary chemical processes such as ET and bond formation [45–47].

The first magnetic field dependent experiments on the ps time scale were performed on a positively charged dye molecule oxazine-1 ( $\text{OX}^+$ ) excited in its first singlet state and dissolved in the electron donor ethyl-ferrocenium (ethylFC) [11, 12]. This system undergoes an ET process from ethylFC to  $\text{OX}^{+*}$  forming the radical pair  $\text{OX}^\bullet / \text{ethylFC}^{+\bullet}$ . The radical pair decays with non-exponential kinetics recovering the ground state species. On the basis of energetics only radical pairs with singlet character are reactive. Since externally applied magnetic fields up to 9 T influence the transition probability between singlet and triplet states, recombination in high fields is delayed without affecting the dynamics of the singlet-phased ET process. Beyond the Zeeman effect, spin relaxation plays the decisive role, thus the ps time resolved magnetic field effect offers a unique route to determine the spin

relaxation rate in its time domain.

The  $\text{OX}^+ / \text{ethylFC}$  intermolecular ET system where the solvent acts as an ET partner suffers from the following limitations: (i) The temperature dependence of spin and in particular ET processes cannot be studied in absorption, due to poor solubility and opacity problems. (ii) the nature of the primary ET process is not clear in the presence of about 20 ethylFC reaction partners.

To overcome the problems (i) and (ii), a novel ferrocenium-nileblue ( $\text{FC} - \text{NB}^+$ ) compound has been synthesized [26], where the nileblue ( $\text{NB}^+$ ) electron acceptor is covalently linked to a ferrocenophane ( $\text{FC}$ ) electron donor (Figure 4.1)

## 4.1 The ferrocenophane-nileblue system

### 4.1.1 Samples

Nileblue ( $\text{NB}^+\text{Cl}^-$ ) as shown in Figure 4.1 (b) was purchased from Sigma-Aldrich as well as ethanol ( $\text{EtOH}$ ) and methanol ( $\text{MeOH}$ ) (spectroscopic grade) and used without further purification. Unless stated otherwise, a mixture of 77%  $\text{EtOH}$  and 33% of  $\text{MeOH}$  has been used in order to open the window to low temperatures as far as possible by optimized glass formation. 2 Vol% acetic acid have been added to inhibit deprotonation (Section 4.1.3).

The single compound ferrocenophane  $\text{FC}$  and the novel ferrocenophane-nileblue compound  $\text{FC} - \text{NB}^+$  (Figure 4.1) were synthesized by M. Stöckl and P. Härter [26].

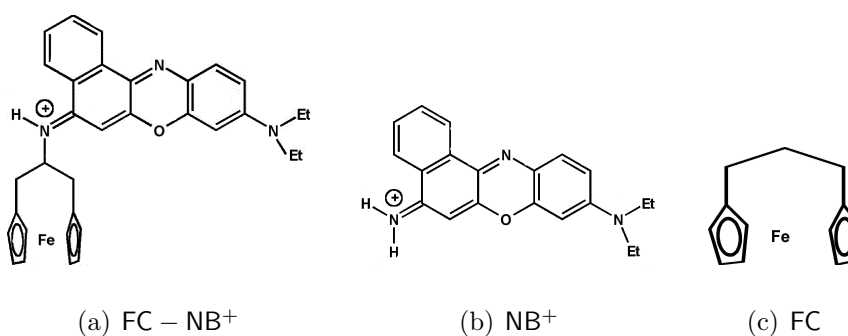


**Figure 4.1:** Covalently linked ET system (a) and isolated moieties (b) and (c)

CHN elementary analysis indicated a purity of better than 99.5% [27],

thin film chromatography in alcoholic solution indicated a faint amount of a second species.

### 4.1.2 Structural calculations

A crude structural estimate of FC – NB<sup>+</sup> can be derived from quantumchemical calculations [48]. Figure 4.2 shows the structure with minimal energy.

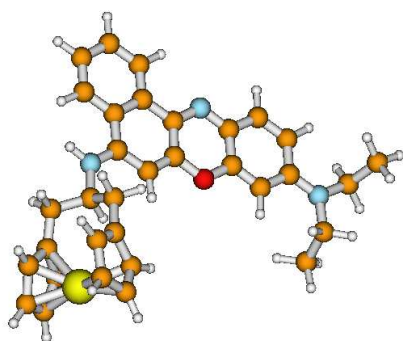


**Figure 4.2:** Quantumchemically calculated structure of FC – NB<sup>+</sup>

The calculations show that the link between the FC and NB<sup>+</sup> moiety is flexible with respect to the rotation around the C – N bonds and of the C – N – C angle. The optimised geometry in gas phase suggests a Fe – O distance of 8.6 Å. As another result, the calculations show that the C<sub>3</sub> bridge forces the cyclopentadienyl rings of the ferrocenophane out of a coplanar configuration by about 30°.

### 4.1.3 Spectroscopic characterisation

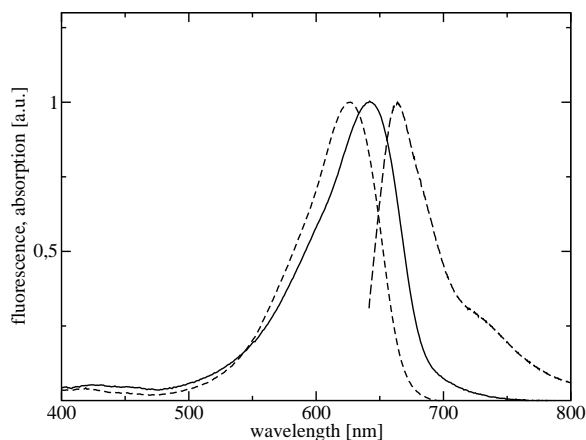
The absorption spectrum of NB<sup>+</sup> has its maximum at 626 nm, the fluorescence spectrum peaks at 664 nm. The absorption spectrum of FC – NB<sup>+</sup> is red shifted by 400 cm<sup>-1</sup> with respect to NB<sup>+</sup> with a maximum at 642 nm. The absorption spectrum of FC – NB<sup>+</sup> is - at half maximum - broadened by 90 cm<sup>-1</sup> with respect to the free dye. The spectra are identical in EtOH, MeOH and the EtOH/MeOH mixture.

Fluorescence of FC – NB<sup>+</sup> cannot be observed; faint residual fluorescence follows the spectrum of free NB<sup>+</sup> dye.

#### Comment on the addition of acetic acid to standard solution

The absorption spectrum of FC – NB<sup>+</sup> in EtOH and the EtOH/MeOH mixture, and to a much lower degree also the absorption spectrum of NB<sup>+</sup>,

**Figure 4.3:** Absorption and fluorescence spectra of  $\text{NB}^+$  (---) and  $\text{FC} - \text{NB}^+$  (—) in standard alcoholic solution.



develops a second absorption band at 500 nm (— in Figure 4.4) when in contact with laboratory glassware. Upon addition of 10 mM of the base diisopropyl-amine this effect was drastically enhanced at the expense of the main absorption band at 642 nm ( $\cdots$  in Figure 4.4). This effect could be reversed by the addition of acetic acid.

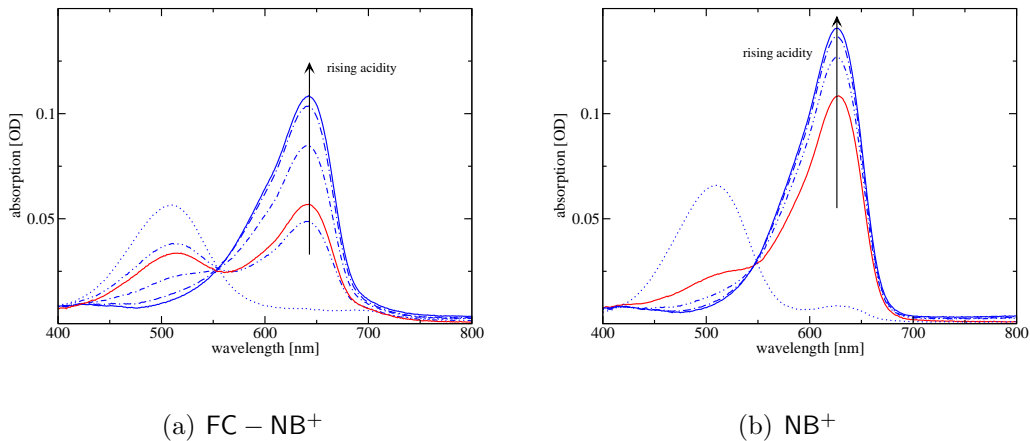


**Figure 4.4:** Absorption spectra of  $\text{FC} - \text{NB}^+$  and  $\text{NB}^+$  in EtOH (—) and in EtOH upon addition of 10 mM diisopropyl-amine ( $\cdots$ ). The spectra (—) show the influence of an increasing concentration of acetic acid.

The existence of a clear isosbestic point at 550 nm is indicative of an equilibrium between the protonated dye and its deprotonated state. It also points to a basic environment to which the solution is exposed to on the walls of the cuvette or other glass instrumentation. Most interestingly, the effect is

stronger in the bridged system than in the free dye pointing to an increased acidity of the N – H bond in the FC – NB<sup>+</sup> compound. The deprotonation effect is suppressed upon addition of 2 Vol% of acetic acid to the standard alcoholic solution. Consequently, all experiments were performed in presence of 2 Vol% of acetic acid.

#### 4.1.4 Redox potentials

The redox potentials of the ET partners in FC – NB<sup>+</sup> have been studied by cyclic voltammetry at a concentration of 500 μM in the presence of 0.1 M LiClO<sub>4</sub> [C. Qijin and J. Ulstrup, Danish Technical University Lyngby]. The oxidation potential  $E(\text{FC}^{\bullet+}/\text{FC}) = -0.17\text{ V}$  of the electron donor and the reduction potential  $E(\text{NB}^+/\text{NB}^{\bullet}) = 0.35\text{ V}$  of the electron acceptor are indicated in Figure 4.5. The plot also shows a cyclic voltammogram (CV) of a solution containing both ET partners simultaneously. The presence of the respective partner does not influence the redox potentials.

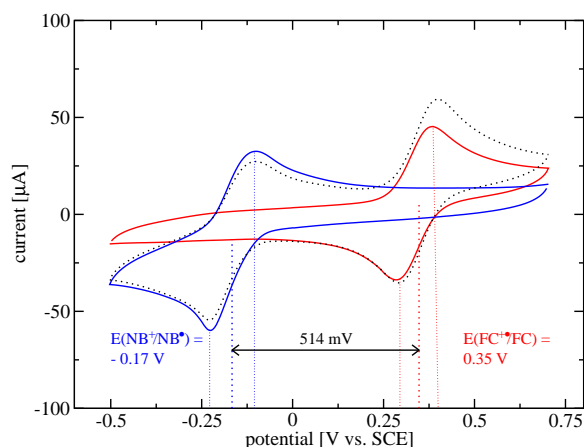
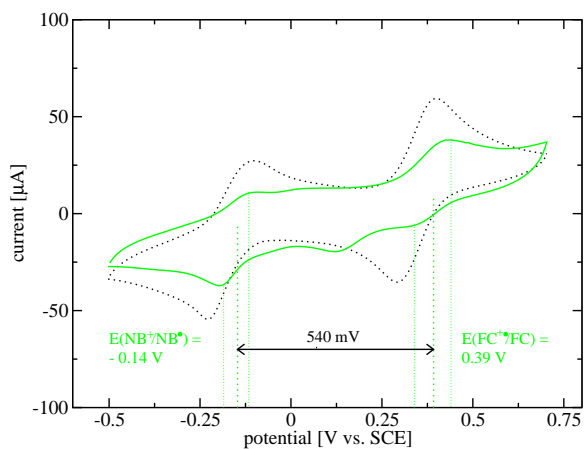


**Figure 4.5:** Cyclic voltammogram of NB<sup>+</sup> (—) and FC (—) measured separately as well as mixed (···) in standard solution; scan speed: 100 mVs<sup>-1</sup>

Figure 4.6 shows CVs of the bridged FC – NB<sup>+</sup> compound in comparison to the separate molecules FC and NB<sup>+</sup>. The redox potentials as derived from this less structured CV are slightly changed: the oxidation potential of the FC moiety is slightly increased to  $E(\text{FC}^{\bullet+}/\text{FC}) = -0.14\text{ V}$ ; the reduction potential of the NB<sup>+</sup> moiety is also slightly increased to  $E(\text{NB}^+/\text{NB}^{\bullet}) = 0.39\text{ V}$ . In contrast to the CVs of the separated ET partners, the CVs of the bridged system are less pronounced. This trend is in agreement with the expectation of a smaller diffusion coefficient of the larger molecule. Surprisingly, there is a third redox peak at around 0.15 V.

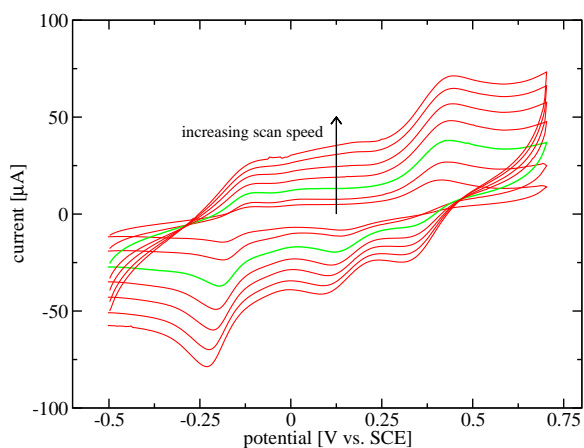
In order to learn more about the origin of this additional peak, scan speed dependent CVs have been taken of the bridged compound. The relative

**Figure 4.6:** CV of FC – NB<sup>+</sup> (—) and FC and NB<sup>+</sup> measured in the same solution (···); scan speed: 100 mVs<sup>-1</sup>



intensity of the peaks is independent of the scan speed between 20 mVs<sup>-1</sup> and 300 mVs<sup>-1</sup> Figure (4.7). This indicates that the third redox peak is not a result of a side reaction.

**Figure 4.7:** CV of FC – NB<sup>+</sup> measured at scan speeds from 20 mVs<sup>-1</sup> to 300 mVs<sup>-1</sup> (—). CV taken at 100 mVs<sup>-1</sup> is highlighted (—).



Thus, the third peak is either due to a side product of the synthesis which does not show up in the CHN analysis, but could be reflected in thin film chromatography (Section 4.1.1), or due to multiple conformations in agreement with quantumchemical calculations (Section 4.1.2).

#### 4.1.5 EPR experiments

DFT calculations on the ferrocenophane moiety FC suggest that the cyclopentadienyl rings are forced out of their coplanar configuration by the C<sub>6</sub> bracket [48]. The components of the *g*-tensor parallel and perpendicular



( $g_{\parallel}$  and  $g_{\perp}$ ) to the molecular axis depend on its symmetry: the  $3d$  orbitals of the Fe atom split in the field of the two cyclopentadienyl rings, which also influences the spin orbit coupling of the unpaired electron located at the Fe atom [49]. The anisotropy of the  $g$  tensor is caused by the field induced by the two cyclopentadienyl rings. As the rings are forced out of their coplanar configuration by the bracket, the anisotropy of the field and consequently of the  $g$  tensor should be reduced.

Since the value for the difference  $\Delta g$  between  $g_{\parallel}$  and  $g_{\perp}$  is needed to model the magnetic field effect, the  $g$  values have been determined by EPR (electron paramagnetic resonance) experiments [O. Schiemann, Institute for Physical Chemistry, University of Frankfurt].

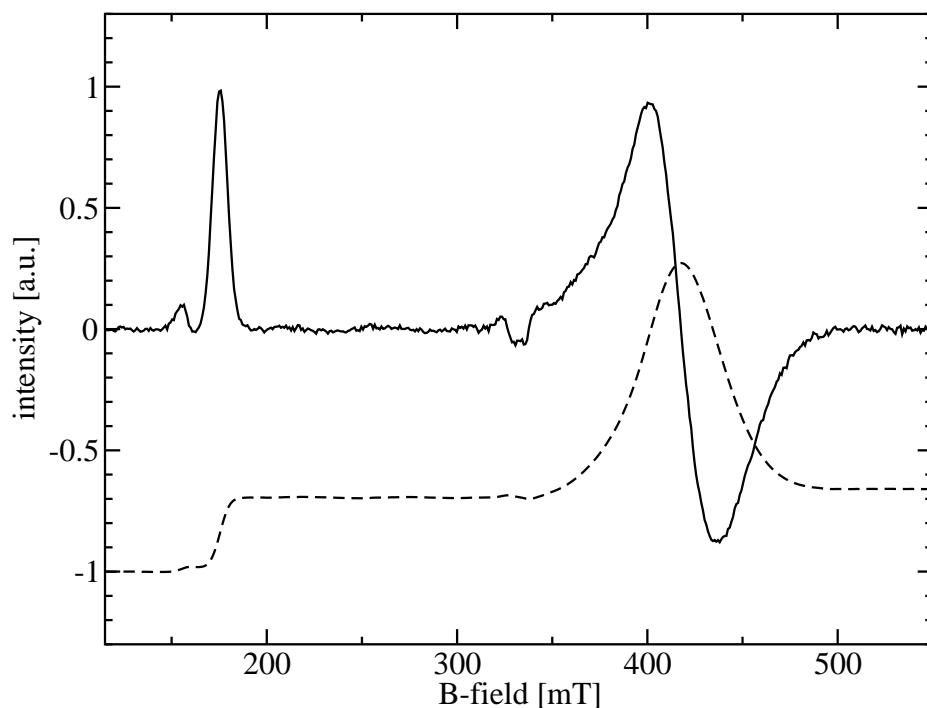


**Figure 4.8:** EPR spectrum of FC in its usual representation as a differentiated spectrum (—) and as an absorption spectrum (---) measured at 10 K at a frequency of 9.42 GHz. Conditions: 0.5 mM FC, 0.5 mM  $\text{AgBF}_4$  in MeOH

Figure 4.8 shows the EPR spectrum of the ferrocenophane. It is a typical spectrum for an isotropic orientation of the molecules with respect to the external magnetic field (“powder spectrum”). The high frequency ( $\nu = 9.4$  GHz) field is absorbed if it is in resonance with the Zeeman splitting between the spin states of the unpaired electrons of the radical:

$$h\nu = g\mu_B B \quad (4.1)$$

This resonance condition is met for  $g_{\parallel}$  in a broad range of magnetic fields and for  $g_{\perp}$  only at a certain value of the magnetic field.  $g_{\parallel}$  can consequently be derived from the onset of the plateau (or peak in the derivative spectrum) and  $g_{\perp}$  can be derived from the absorption band (or S-form signal in the derivative spectrum). The components of the  $g$ -tensor then are  $g_{\parallel} = 3.86$  and  $g_{\perp} = 1.61$  ( $\Delta g = 2.25$ ). As expected,  $\Delta g$  is smaller than for the undistorted ethylFC  $\Delta g = 3.1$ .

## 4.2 Femto- and picosecond time resolved spectroscopy

Time resolved transient absorption experiments have been performed to determine the kinetics of the formation and decay of the radical pair state. These experiments have been carried out utilising two different setups: (i) a laser system with a ultrahigh time resolution of 15 fs was used to resolve the ultrafast forward ET (FET) reaction [27, 48] and (ii) the laser system described in section 2.1.1 with a time resolution of 150 fs including the superconducting magnet to apply a magnetic field of up to 8 T and to vary the temperature. This setup was used to monitor the back ET (BET) process.

### 4.2.1 Forward electron transfer

The FET process in  $\text{FC} - \text{NB}^+$  can be followed by transient absorption experiments as a decay of the stimulated emission signal in the spectral region of fluorescence of  $\text{NB}^+$  at 700 nm. As the time resolution of setup (ii) was too low for experiments on FET, they were performed on the setup (i). The red line in Figure 4.9 shows the difference absorbance signal at 700 nm after excitation at 630 nm. A bi-exponential fit yields time constants of 90 fs and 400 fs with similar amplitudes [27]. An oscillation with a half-period of about 50 fs is superimposed on this signal. These oscillations are in very good agreement with resonance Raman lines at  $600 \text{ cm}^{-1}$ , observed in  $\text{FC} - \text{NB}^+$  and  $\text{NB}^+$ . DFT calculations on the  $\text{NB}^+$  system identify these oscillations as vibrations of the oxygen and nitrogen located in the center of the aromatic system of the dye [48].

The amplitude spectrum of the 90 fs component has a minimum at 650 nm and follows the fluorescence spectrum of  $\text{NB}^+$ , as expected for stimulated emission. The minimum of the 400 fs spectrum is shifted to 690 nm. In addition, the spectrum has a positive component in the range from 600 nm to 650 nm [48]. These characteristics of the 400 fs component point rather to another species than to a different conformation with altered charge transfer properties. This interpretation would be consistent with a second component which could be the origin of the third peak in the CV (Section 4.1.4) and the faint second component in thin film chromatography (Section 4.1.1).

Excitation at 530 nm and 630 nm resulted in equal kinetics, apart from a delayed start of oscillations for excitation at 530 nm [48].

Temperature-dependent measurements in the range from 295 K to 170 K on the setup (ii) showed that the lifetime of the stimulated emission signal does not exceed the time resolution of about 150 fs. As expected [11, 12, 50],

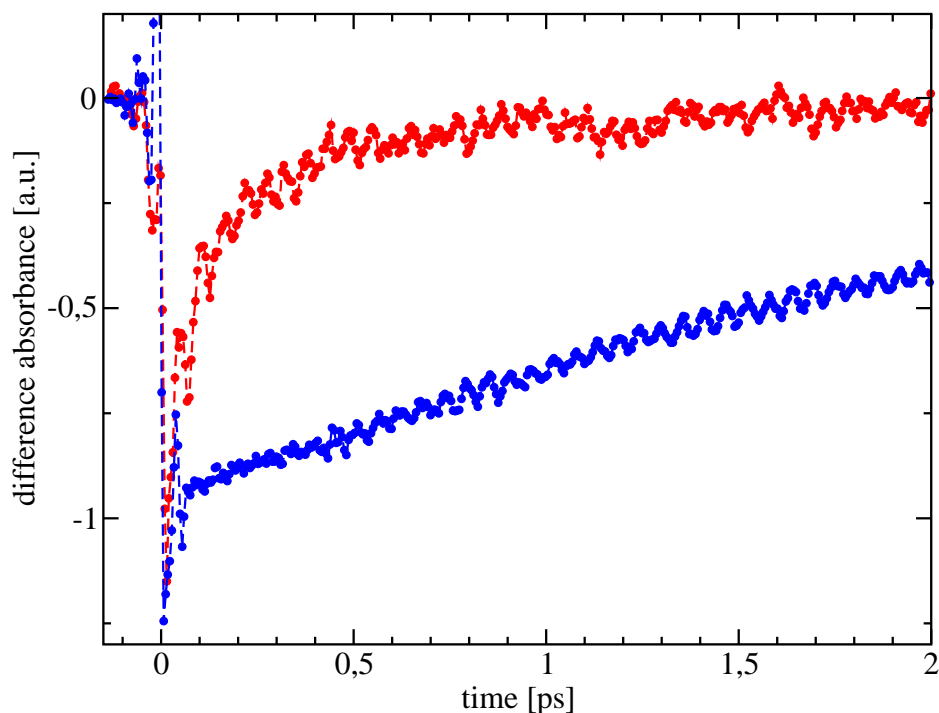


**Figure 4.9:** Difference absorbance signal of  $\text{FC} - \text{NB}^+$  probing stimulated emission at 700 nm (—) and ground state bleaching at 600 nm (—) after excitation at 630 nm.

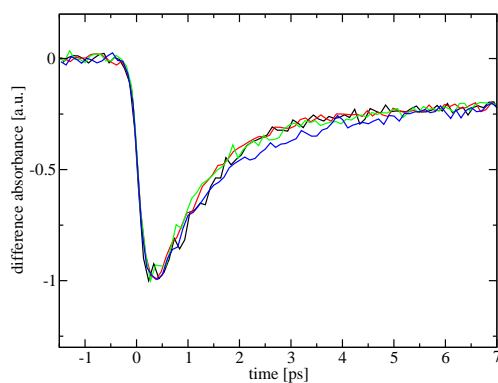
no magnetic field dependence of the FET could be observed.

### 4.2.2 Back electron transfer and magnetic field dependence

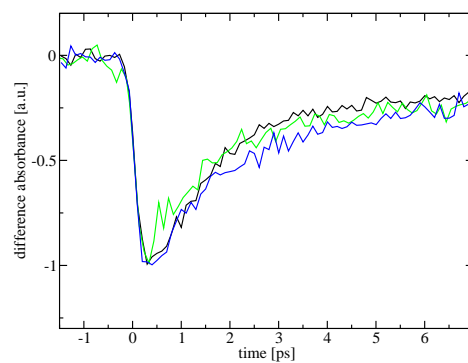
The decay of the  $\text{FC}^{+\bullet} - \text{NB}^{\bullet}$  radical pair leads to a recovery of ground state absorption. The blue time trace in Figure 4.9 shows that these recovery dynamics are much slower than the FET dynamics and oscillations with the same frequency can be observed on the signal [27, 48].

The BET dynamics are multiexponential. Unlike the FET process, the time traces depend on an external magnetic field as well as on temperature (Figure 4.10).

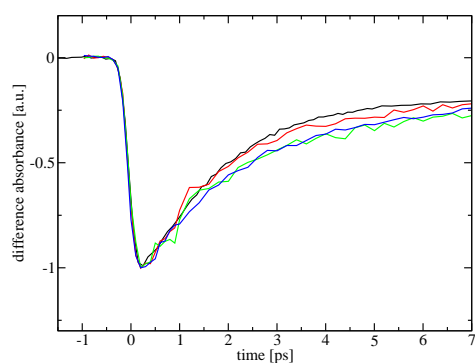
In cases, where ET in either singlet or triplet channel is favoured for energetic reasons, singlet–triplet transitions delay the dynamics of the BET process. Then the kinetics has to be modeled in order to extract the rates of BET and spin relaxation.



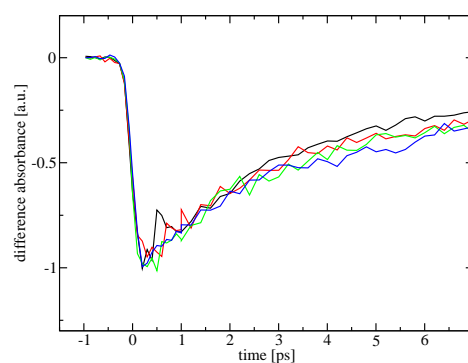
(a) 295 K



(b) 260 K



(c) 230 K



(d) 170 K

**Figure 4.10:** Difference absorbance signals at 610 nm after excitation at 650 nm. Different colors represent externally applied magnetic fields: 0 T (—), 3 T (—), 5 T (—) and 7 T (—)

### 4.3 Analysis of the magnetic field effect

Multieponential increase of ground state absorption and its magnetic field dependence are expected to be due to spin conversion in analogy to the  $\text{OX}^+$ /ethylFC system in solution [11,12]. In case the donor-acceptor distance is 7 Å, this results in an exchange interaction energy as small as  $0.1 \text{ cm}^{-1}$  [12]. Such splittings can be diagnosed in external magnetic fields in the order of a few Teslas ( $1 \text{ T} = 1000 \text{ Gauss}$ ). This type of magnetic field effect is in contrast to hyperfine interaction in radical pairs, which can be diagnosed with magnetic fields of the order of 100 Gauss. Since BET can only occur in the singlet channel the decay of the radical pair is magnetic field dependent. As the local  $T$  state of the  $\text{NB}^+$  moiety is too high in energy ( $E(^1\text{NB}^{+*}) - E(^3\text{NB}^+) = 0.4 \text{ eV} = 3200 \text{ cm}^{-1}$  in analogy to the closely related methylene blue [51]), BET can only occur in the singlet channel.

As the Zeeman splitting for an organic molecule is in the range of only  $10 \text{ cm}^{-1}$  for the magnetic fields applied here, magnetic field dependence of the FET process is not expected.

#### 4.3.1 Model

##### Base of spin system

The radical pair consists of the  $\text{NB}^\bullet$  radical and the  $\text{FC}^{\bullet+}$  cation radical containing the transition metal Fe. For these radicals the electronic wave functions are treated separately. The wave function of  $\text{NB}^\bullet$  is described by the spin states  $\alpha$  and  $\beta$ . For the  $\text{FC}^{\bullet+}$  radical, the spin orbit coupling cannot be neglected because of the presence of the heavy transition metal. In this case it is useful to describe the states in a Kramers representation, where the influence of the spin orbit coupling is already accounted for. It has to be underlined, that the Kramers states  $\alpha'$  and  $\beta'$  do not describe pure spin states any more.

The four spin states of the radical pair in the Kramers representation can then be represented by linear combinations of the two sub-systems:

$$\begin{aligned}
 S' &= \frac{1}{\sqrt{2}}(\alpha\beta' - \beta\alpha') \\
 T'_+ &= \alpha\alpha' \\
 T'_0 &= \frac{1}{\sqrt{2}}(\alpha\beta' + \beta\alpha') \\
 T'_- &= \beta\beta'
 \end{aligned} \tag{4.2}$$

### Stochastic Liouville Equation

A complete quantum-mechanical description by the Schrödinger equation (4.3) of a system as complex as a molecule in solution is impossible.

$$\dot{\Psi} = -\frac{i}{\hbar}\hat{H}\Psi \quad (4.3)$$

In this case, a density matrix approach has to be applied to, nevertheless, be able to account for the important concepts of quantum mechanics. Density matrices  $\rho$  reflect the states of the system rather than its wavefunction  $\Psi$ , and a combination of quantum-mechanical approaches and classical rate concepts is possible. It can be applied to reduce the parameterset of the problem. The differential equation describing the transitions between the spin states of the radical pair is called the stochastic Liouville equation (4.4) (SLE) [8]:

$$\dot{\rho}_\Omega = -\frac{i}{\hbar}[\hat{H}_\Omega, \rho_\Omega]_- + \hat{\mathcal{R}} - \frac{1}{2}[\hat{K}, \rho_\Omega]_+ \quad (4.4)$$

where  $\rho_\Omega$  is the density matrix based on the Kramers spin states defined in equation (4.2) parameterized for the angle  $\Omega$  between the axis of the radical pair and the externally applied magnetic field. The SLE consists of 3 parts, namely:

- the Hamilton term  $-\frac{i}{\hbar}[\hat{H}_\Omega, \rho_\Omega]_-$  describing the influence of the Hamilton operator onto the density matrix
- the relaxation term  $\hat{\mathcal{R}}$  describing relaxation processes between the spin states
- the reaction term  $-\frac{1}{2}[\hat{K}, \rho_\Omega]_+$  describing the ET out of the spin system

The **Hamilton term** accounts for the influence of the Hamilton operator  $\hat{H}_\Omega$  on the density matrix  $\rho_\Omega$ . Only contributions leading to energetic variations on the same time scale as the corresponding<sup>1</sup> lifetime of the radical pair (a few picoseconds, as can be seen in figure 4.10) can influence the recombination dynamics. In terms of energy, this implies that contributions less than  $0.1 \text{ cm}^{-1}$  can be neglected.

The Zeeman interaction leads to an energetic splitting of the spin states in an external magnetic field:

$$\hat{H}_{\text{Zeeman}} = \mu_B \vec{B}_0 \left( \mathbf{g}_{\text{FC}} \hat{S}' + \mathbf{g}_e \hat{S} \right) \quad (4.5)$$

---

<sup>1</sup> $\Delta E = h\nu$  enables to compare energy and time domain

where  $\hat{S}$  is the spin state of the organic radical and  $\hat{S}'$  the Kramers state of the ferrocenophane radical;  $\mathbf{g}_e$  and  $\mathbf{g}_{\text{FC}}$  are the  $g$ -tensors for the organic radical, approximated by the value for a free electron, and for the ferrocenophane radical, respectively.

As the  $g$ -tensors for the two radicals differ, the population of the spin states oscillates with period  $\tau_{\Delta g}$  between the  $S'$  and  $T'$  states, similar to the classical spin chemical  $\Delta g$  mechanism [45]:

$$\tau_{\Delta g} = \frac{h}{\Delta \mathbf{g} \mu_b \vec{B}} \quad (4.6)$$

Since the  $g$ -tensor  $\mathbf{g}_{\text{FC}}$  for the ferrocenophane cation radical is anisotropic, the oscillation depends on the orientation of the radical and the magnetic field  $\vec{B}$ . The values for  $\mathbf{g}_{\text{FC}}$  were measured in ESR experiments (Section 4.1.5).

The **relaxation term** describes transitions between the  $S'$  and  $T'$  states. It depends on the longitudinal and transversal spin relaxation times  $T_1$  and  $T_2$ . In organic molecules, the spin lattice relaxation times are in the range of  $\mu\text{s}$  and thus irrelevant on a ps time scale; in transition metal compounds this process can be much faster. In this case  $T_1$  and  $T_2$  are equal and are replaced by the spin relaxation time  $\tau_S$ . The relaxation rates  $k_1$  and  $k_2$  are given by:

$$\begin{aligned} k_1 &= \frac{1}{2\tau_S} \\ k_2 &= \frac{1}{\tau_S} \end{aligned} \quad (4.7)$$

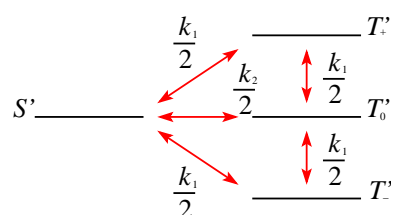


**Figure 4.11:** Spin relaxation process

It is a central goal of the experiments presented here to obtain the spin relaxation time by modeling the kinetic data.

The **reaction term** describes the processes leading to a depopulation of the radical pair. In this case, the only process for this is the BET reaction described by the ET rate  $k_{\text{BET}}$ .

As the only product state which can be reached for energetic reasons has singlet character, this process can only originate from *spin* states with singlet character, opposed to the *Kramers* representation used in this model.



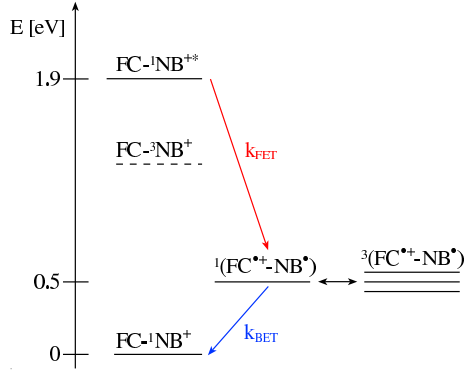


**Figure 4.12:** Magnetic field dependent reaction pathway for  $\text{FC} - \text{NB}^+$  after photoexcitation.

Therefore it is necessary to determine the pure singlet contribution of the  $S'$  and  $T'$  states. To convert Kramers representation to pure spin representation, space and spin contribution to the Kramers state have to be separated. For the  $T'_+$  and  $T'_-$  state, the Kramers representation is equivalent to the spin representation. For the  $S'$  and  $T'_0$  state, this effect can be fully described by the perpendicular part of the  $g$ -tensor  $g_\perp$  of the ferrocenophane radical. According to [12], the singlet character of the  $S'$  state  $p_s(S')$  is:

$$p_s(S') = 0.5 + \frac{g_\perp}{4} \quad (4.8)$$

and the singlet character of the  $T'_0$  state  $p_s(T'_0)$ :

$$p_s(T'_0) = 1 - p_s(S') = 0.5 - \frac{g_\perp}{4} \quad (4.9)$$

The FET process populates the  $S'$  and  $T'_0$  state of the radical pair depending on its singlet character  $p_s(S')$  and  $p_s(T'_0)$ , respectively. In the simulation, this is accounted for by an initial population of these states according to their singlet character.

### 4.3.2 Modeling the experimental data

The time trace for the recovery of the ground state absorption cannot be described by a monoexponential function (Section 4.2.2). As shown in the previous chapter, the BET reaction kinetics are masked by spin processes. It is impossible, at least in this context, to analytically transform the differential equation system of the SLE (equation (4.4)) to a set of equations in the time domain. In order to simulate the problem numerically a software package was developed by D. Bürßner [52] and adapted by P. Gilch [12]. Starting from the initial population of the  $S'$  and  $T'$  states (equations 4.8 and 4.9), the population of the radical states and the product state of the BET process

is calculated iteratively. This allows to reconstruct the repopulation of the ground state.

The kinetics of ground state recovery have been modeled with following variables and assumptions yielding spin relaxation time  $\tau_S$  and the back ET rate  $k_{\text{BET}}$ : (i)  $\Delta g = g_{\perp} - g_{\parallel} = 2.25$  of the  $\text{FC}^{\bullet+}$  cation radical has been determined by EPR experiments (Section 4.1.5); (ii) an isotropic orientation of the molecules with respect to the magnetic field was assumed. In fact, the kinetics did not depend on the orientation of the polarisation axis of the excitation beam towards the magnetic field. A 5% constant offset was assumed at all temperatures derived from the offset of the BET kinetics at long times.

As the lifetime of the excited  $\text{FC} - \text{NB}^{+*}$  state is with 90 fs shorter than the excitation pulse, both processes can in a first approximation be described by a single Gaussian with the response function of the setup of 150 fs.

With this set of input parameters, the ground state depletion signal was simulated with an iteration step size of 10 fs, which is more than 100 times smaller than the shortest time constants expected for the BET and spin relaxation. A further decrease of the step size was not possible, as the simulation of one time trace already took about 5 – 10 s on the computers used.

To find a matching pair of BET and spin relaxation rates, the time traces were simulated for 0 T and 7 T in a 2-dimensional grid of BET and spin relaxation rate covering reasonable values for both parameters. The step size for the BET rate was 0.1 ps, for the spin relaxation rate, 0.5 ps.

As shown in figure 4.13, the simulation of the zero-field and magnetic field experiment reproduces in a satisfactory way the experimental data. The temperature dependence of the BET and spin relaxation rates can be extracted from the Arrhenius plot in Figure 4.14 and are compiled in the following table.

	295 K	260 K	230 K	170 K	$E_A$
$k_{\text{BET}}$	$(1.2 \text{ ps})^{-1}$	$(1.2 \text{ ps})^{-1}$	$(1.7 \text{ ps})^{-1}$	$(2.4 \text{ ps})^{-1}$	24 meV
$k_S$	$(14.3 \text{ ps})^{-1}$	$(18.2 \text{ ps})^{-1}$	$(25.0 \text{ ps})^{-1}$	$(40.0 \text{ ps})^{-1}$	26 meV

**Table 4.1:** Results from simulation for the BET and the spin relaxation rate and their activation energies

Both, the spin relaxation and BET rate are temperature dependent following an Arrhenius type pattern very nicely. A least square fit of both rates reveals very small activation energies only slightly larger than  $kT$  at room temperature.

To the extent to which the simulation satisfactorily describes the measured kinetics, BET can be regarded as a monoexponential process.

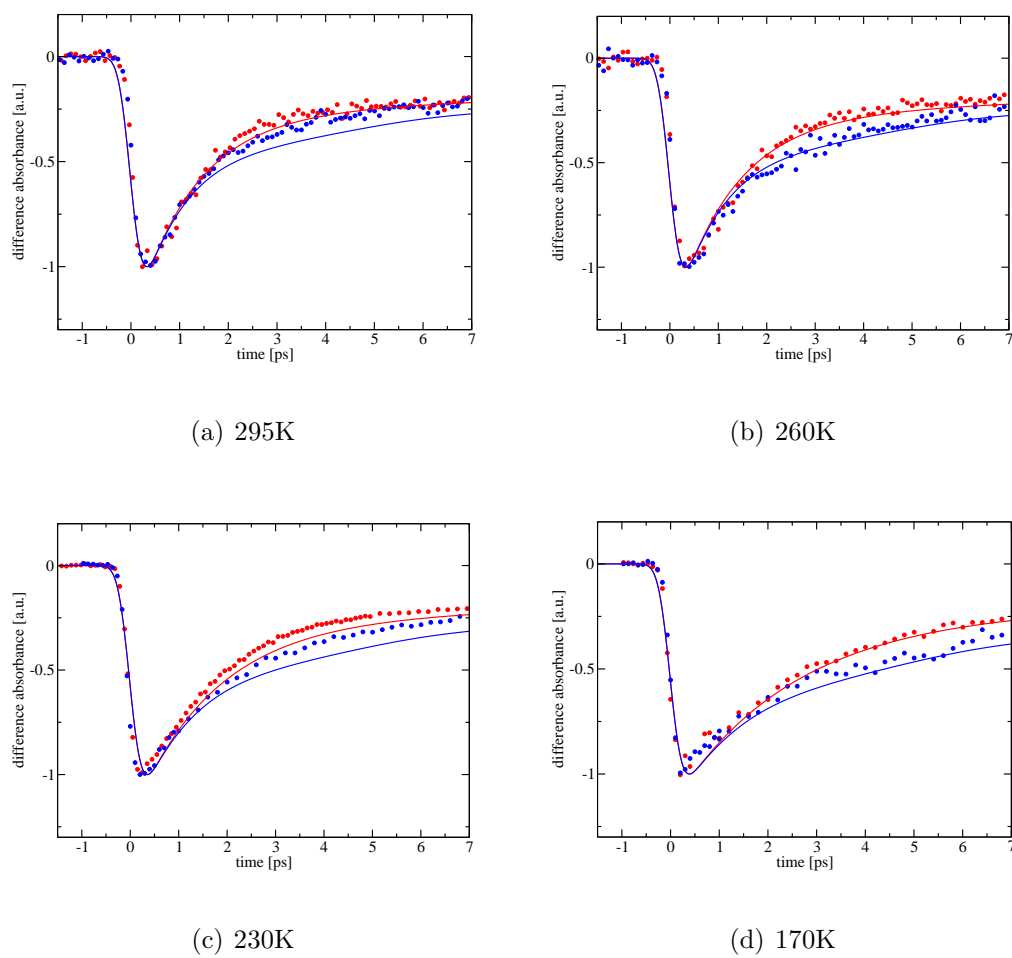


**Figure 4.13:** Ground state recovery at  $0\text{ T}$  and  $7\text{ T}$ . Modeled time traces (—) and difference absorbance signals at  $610\text{ nm}$  (●)

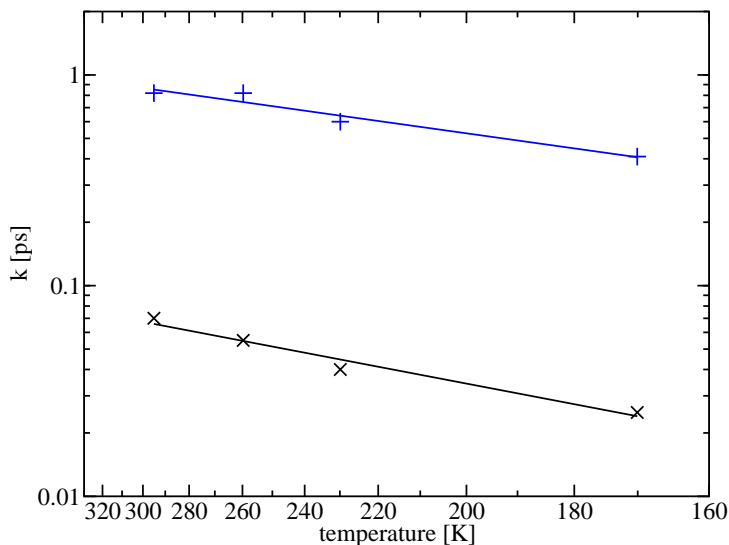


**Figure 4.14:** Temperature dependence of the rates for BET (—) and spin relaxation (—)

## 4.4 Mechanism of spin relaxation

Spin relaxation may be induced by fluctuations of the magnetic (i) or the electric field (ii) [9, 12, 53].

(i) The simplest mechanism of spin relaxation is one where the transition between the spin states is induced by fluctuations of the magnetic field directly inducing transitions between the Kramers states of the radical. These fluctuations in the coordinate system of the molecule can be induced by rotation of the molecule itself in a static external magnetic field. Within this mechanism, the spin relaxation time correlates linearly with the rotational relaxation time  $\tau_r$  [54]. An estimate of  $\tau_r$  by the Debye formalism

$$\tau_r = \frac{8\pi\eta(T)r^3}{kT} \quad (4.10)$$

for  $\text{FC} - \text{NB}^+$  with an hydrodynamic radius  $r = 7 \text{ \AA}$  and a viscosity of  $\eta = 1 \text{ cp}$  as a weighted mean of the literature data for the viscosity of ethanol (1.2 cp) and methanol (0.6 cp) at 295 K [55] yields a rotational relaxation time of  $\tau_r \approx 1 \text{ ns}$ . This seems too high by about a factor of 10, compared to e.g. a rotational relaxation time of  $\text{R6}^+$  in aqueous solution in the order of 100 ps. Even for  $\tau_r$  in the order of 100 ps, this mechanism is disfavoured as the dominant process for spin relaxation, as  $\tau_S$  is still one order of magnitude

shorter than  $\tau_r$  and in agreement with literature [11, 53].

In the present case, a stronger argument can be made based on the temperature dependence of  $\tau_S$ , excluding the uncertainties for the determination of the rotational relaxation time of the flexibly bound FC moiety and the correlation of  $\tau_S$  and  $\tau_r$ .

Based on the temperature dependence of the viscosity of ethanol and methanol [55] and the explicit temperature dependence in equation (4.10), the Debye formalism allows an estimate of the *change* of  $\tau_r$  with temperature without further assumptions about the hydrodynamic radius  $r$ . Figure 4.10 shows this change of  $\tau_r$  compared to the change of the spin relaxation time of FC – NB<sup>+</sup> with temperature normalized to the respective values at 295 K. Based on the different slopes, mechanism linked to rotational relaxation can be ruled out as dominant processes for this system.

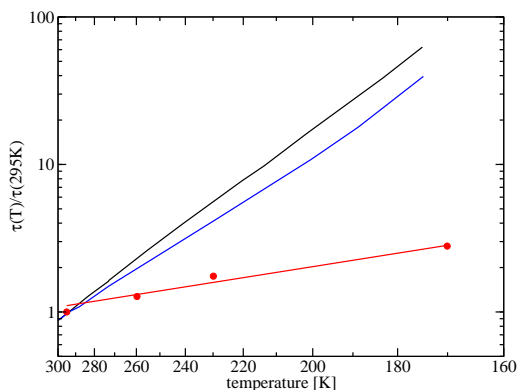


**Figure 4.15:** Experimental values for  $\tau_S(T)/\tau_S(295\text{ K})$  with Arrhenius fit (—) in comparison to  $\tau_r(T)/\tau_r(295\text{ K})$  for viscosity data of ethanol (—) and methanol (—) according to the Debye formalism

(ii) In an extension of the Orbach mechanism, transitions between the Kramers states within one doublet can also be mediated by a transition into a higher Kramers doublet. These transitions can be induced by variation of the electric field due to solvent fluctuations [9]. Spin orbit coupling permits electric field fluctuations to cause electron spin changes. The process itself is temperature independent; in this model, the temperature dependence is reflecting the temperature dependence of the solvent fluctuations. As the energy difference between Kramers doublets of ferrocenes is in the range of several 10 meV [12], thermal energy is sufficient to induce this transition.

## 4.5 Mechanistic aspects of electron transfer

### 4.5.1 Driving forces, ET-rates and their temperature dependence

The time constants for FET and BET ( $k_{\text{FET}} = (90 \text{ fs})^{-1}$  and  $k_{\text{BET}} = (1.2 \text{ ps})^{-1}$  at 295 K) are almost temperature independent within a factor of 2 comparing 295 K and 170 K.

The driving force for the forward ( $\Delta G_{\text{FET}}$ ) and back ( $\Delta G_{\text{BET}}$ ) ET reaction can be estimated based on the Rehm–Weller equation. Since we discuss a charge shift reaction, the Coulomb term is expected to be negligible:

$$\begin{aligned}\Delta G_{\text{FET}} &= E(\text{FC}^{\bullet+}/\text{FC}) - E(\text{NB}^+/\text{NB}^{\bullet}) - E_{0,0}(\text{NB}^+) \\ \Delta G_{\text{BET}} &= -E(\text{FC}^{\bullet+}/\text{FC}) + E(\text{NB}^+/\text{NB}^{\bullet})\end{aligned}\quad (4.11)$$

Usually, the  $E_{0,0}$  transition energy is estimated from the point of intersection between the normalized absorption and fluorescence spectrum. As fluorescence is almost totally quenched in the  $\text{FC} - \text{NB}^+$  compound, half the difference between the maximum of fluorescence and absorption spectra of  $\text{NB}^+$  is added to the position of the maximum of absorption of  $\text{FC} - \text{NB}^+$ , yielding a  $E_{0,0}$  transition energy of  $E_{0,0}(\text{NB}^+) = 1.86 \text{ eV}$ . From  $E(\text{FC}^{\bullet+}/\text{FC}) - E(\text{NB}^+/\text{NB}^{\bullet}) = 520 \text{ mV}$  (Section 4.1.4) the values for  $\Delta G_{\text{FET}}$  and  $\Delta G_{\text{BET}}$  are as follows:

$$\begin{aligned}\Delta G_{\text{FET}} &= -1.35 \text{ eV} \\ \Delta G_{\text{BET}} &= -0.52 \text{ eV}\end{aligned}\quad (4.12)$$

### 4.5.2 Interpretation of ET rates

On the basis of the weak temperature dependence of the back reaction and its small driving force  $\Delta G_{\text{BET}}$ , it is assumed that BET occurs in the activationless region. In the frame of Marcus–Levich–Jortner theory this allows a crude estimate of the reorganisation energy of  $\lambda_{\text{BET}} = 0.5 \text{ eV}$ . The state from which BET originates can be identified as a radical ion pair via the magnetic field effect on the kinetics.

The FET process with a rate of  $k_{\text{FET}} = (90 \text{ fs})^{-1}$ , is by more than a factor of 10 faster than BET with a rate of  $k_{\text{BET}} = (1.2 \text{ ps})^{-1}$ . The driving force for FET is extremely large with  $\Delta G_{\text{BET}} = 1.4 \text{ eV}$ . If this reaction were a single step process and  $\lambda_{\text{BET}} \approx \lambda_{\text{FET}}$ , FET would occur deeply in the Marcus inverted region.

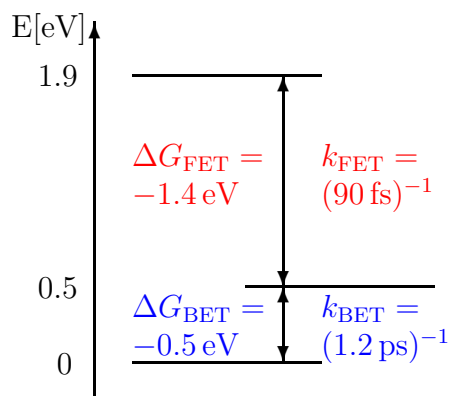


**Figure 4.16:** FET and BET rates together with their driving forces at 295 K

Considering the large driving force and the ultrafast time scale for FET (Figure 4.16), the question arises how the radical ion pair is formed.

The basis for the applicability of the conventional ET theory is the separation of time scales of solvent relaxation and the ET process, with solvent relaxation being faster. This basic requirement is violated when the ET process is as fast as 90 fs and when the shortest dielectric relaxation times for ethanol is 1.8 ps (MeOH: 1.1 ps) [56]. Nevertheless, the ET process can be very fast if it is strongly coupled to quantum modes. In this case, the process can behave like a barrierless process, even if it is deeply in the inverted Marcus regime. Unfortunately, for this case, no definite formalism has been developed yet, due to the fact that a large variety of effects may play a role.

Assuming that the FET process is activationless and the reorganisation parameter  $\lambda_{\text{FET}} = 0.5 \text{ eV}$  as in the BET reaction,  $0.9 \text{ eV}$  ( $7000 \text{ cm}^{-1}$ ) have to be dissipated by the high frequency mode. A potential vibrational mode is detected in resonance Raman spectroscopy and associated with a symmetric vibration of the C atoms on the ring to which the  $\text{NEt}_2$  group is bound with  $\nu = 1600 \text{ cm}^{-1}$  [48]. Independent of the nature of the ET mechanism, the electronic coupling for FET seems to be much larger than for BET ( $V_{\text{FET}} > \sqrt{10} \cdot V_{\text{BET}}$ ). Intuitively, and in some cases *de facto*,  $V_{\text{FET}}$  has been shown to drastically exceed  $V_{\text{BET}}$  [57–59]. Relatively straightforward arguments favour larger couplings whenever excited states are involved, reflecting the extension of the electronic wavefunction. However, this turned out not be a rule of thumb, since electronic coupling depends in a very sensitive way

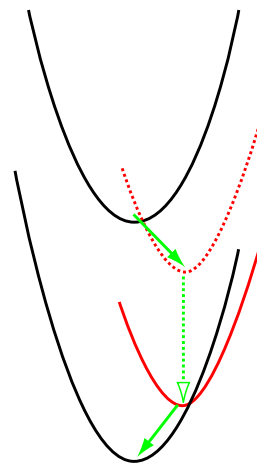


**Figure 4.17:** Reaction pathway from photoexcited reactant state to an intermediate state ( $\cdots$ ) and subsequent relaxation ( $\cdots$ ) forming the radical pair state ( $-$ )

on the charge distribution of the initial excited state and the product duplet states.

However, differences in electronic coupling can also arise from conformational changes in non-rigid ET systems such as  $\text{FC} - \text{NB}^+$  (Section 4.1.2) in the time window between the two processes. There are experimental observations speaking against such a trivial explanation: (i) Conformational fluctuations should lead to a distribution of structural conformations. This usually results in nonexponential kinetics. Within the uncertainties of the simulation, this effect could not be observed. (ii) Conformational fluctuations should strongly depend on the viscosity of the solvent. This is not the case, since an increase of viscosity by a factor of 20 to 40 while cooling the solution to 170 K slows the rates down by a factor of 2 at most. (iii) The quantum beats both on the stimulated emission and on the ground state bleaching signal persist for picoseconds. At the very end, a mechanism where the primary FET leads to an electronically excited product state might be feasible.

In this model, ET from the  $(\text{NB}^+)^*$  moiety of the compound leads to either an excited ferrocenophane cation radical  $(\text{FC}^{+\bullet})^*$  or an excited neutral radical of the dye  $(\text{NB}^\bullet)^*$ . Following FET, the locally excited state then relaxes to its electronic radical ground state ( $\text{FC}^{+\bullet}$  or  $\text{NB}^\bullet$ ), from where the back ET process takes place.

The electronically excited states of the radical can only be efficiently populated, if their  $S_{0 \rightarrow 1}$  energy gap is less or at most equal to the apparent driving force  $\Delta G_{\text{FET}} = 1.4 \text{ eV}$  ( $11300 \text{ cm}^{-1}$ ). However, the ferrocenium cation radical shows an absorption maximum at around 610 nm ( $16400 \text{ cm}^{-1}$ ) in methylene chloride [12] and the neutral radical absorption of methylene blue, which is closely related to  $\text{NB}^+$  is centered around 400 nm ( $25000 \text{ cm}^{-1}$ ). These absorption spectra of the product states indicate a far too large energy



gap between the radical ground state and its electronically excited state to account for an easily accessible excited product state.

A very strong coupling of the excited electronic reactant state with the excited electronic states of the product could eventually lower the energy of the combined state which is assumed to be an electronically excited charge transfer state ( $\text{FC}^+ - \text{NB}$ )\*. This excited charge transfer state has to relax to the radical pair in its ground state on a time scale faster than 1 ps. No spectroscopic evidence could be found for the existence of such an excited charge transfer state.

In recent years, several ET systems with a sub-100 fs FET process and a ps BET rate have been studied, including other nileblue systems [60], rhodamines [61] and oxazine-1 [62, 63]. In all other systems, in contrast to the  $\text{FC} - \text{NB}^+$  system, an intermolecular charge transfer was observed, where the solvent acted as the electron donor and thus, a multiplicity of potential electron donors are present in the environment of the excited electron acceptor. In these intermolecular ET systems,  $\Delta G_{\text{FET}}$  was around 0.5 eV and  $\Delta G_{\text{BET}}$  around 1 eV assigning the BET process to the Marcus inverted region. Temperature dependent experiments with charge transfer rates in these time scales have, to our knowledge, not been reported.

The presented models for FET are based on the Fermi Golden Rule expression for the ET rate, and thus assume that vibrational energy and phase relaxation processes are fast compared to the ET reaction. In the case of ultrafast ET with a large excess of vibrational energy, the Golden Rule description becomes questionable and a nonperturbative treatment of the reaction must be considered [64].



# Chapter 5

## Charge Injection into Rhodamine labeled DNA Duplexes

Distance dependence of ET in DNA has been of interest for several years now [14, 16, 19–24] and has even given rise to fundamental questions concerning ET theory [18]. In this chapter, the distance dependence of charge injection into DNA is studied, where the hole injector Rhodamine 6G is expected to be semi-endcapped on the base stack.

Rhodamine labeled DNA duplexes are often used for indirect structural studies on DNA by Förster transfer [65–67] and now become increasingly interesting for biotechnological applications (“molecular beacon” [68, 69]). Within this context, detailed knowledge about the charge injection properties and the degree of structural definition of the molecular system is of great importance. In a comparison of NMR structure and results from time resolved spectroscopy on identical DNA strands, the degree of structural definition is examined.

### 5.1 Samples

#### 5.1.1 Dyes and buffers

The dyes Rhodamine 6G ( $R6^+$ ) and Rhodamine 19 ( $R19^+$ ) were obtained from Radiant Dyes, Tetramethylrhodamine ( $TMR^+$ ) from Sigma-Aldrich. All dyes were used without further purification or treatment. As shown in Figure 5.1,  $R6^+$  and  $R19^+$  differ only in the side group at the phenoxy ring: compared to  $R6^+$ , in  $R19^+$  the ester group is split off, leaving a  $COO^-$  rest.

Throughout this work, a 10 mM pH 7.0 phosphate buffer with 150 mM NaCl was used. The buffer has been prepared in the laboratory from *p.a.* grade salts with bi-distilled water.

### 5.1.2 Oligomers and reference names

In this work, a number of rhodamine labeled DNA oligomers have been studied. On all samples, the rhodamine modification has been attached to the 5' end of the modified DNA strands by a C<sub>6</sub> linker as depicted in Figure 5.2. The DNA samples with a 5-carboxy Rhodamine 6G isomer were obtained from Eurogentec in *page purified* quality<sup>1</sup>. One oligomer with 5-carboxy-Tetramethylrhodamine was obtained from the laboratory of C. Griesinger at the Max Planck Institute for Biophysical Chemistry (Göttingen) and HPLC purified after NMR studies have been performed on this sample. Although both modifications carry opposite charges on the xanthene ring and the phenyl ring, they are referred to as R6<sup>+</sup> and TMR<sup>+</sup> as the xanthene ring is positively charged and responsible for the optical and charge transfer properties. The rhodamine modified samples are listed in Table 5.1 together with their reference names used throughout this work and their melting temperatures.

As the NMR structure of the duplexes 6CAA and 4CAA has been resolved [H. Neubauer and C. Griesinger at Max Planck Institute for Biophysical Chemistry, Göttingen], the sequences of 6CAA, 4CAA and 6GAA were predefined. For further studies on the replacement of G by Z, several 13 bp duplexes were studied<sup>2</sup>. The length of these duplexes was decreased to facilitate further NMR studies. As the terminus of a DNA duplex is critical for its stability, and G : C base pairs are more stable than A : T base pairs, the duplexes are closed with a GCG sequence.

A sample with G neighboring the R6<sup>+</sup> modification was obtained in 13 bp and 20 bp configuration (s6GAA and 6GAA) in order to study differences of distant basepairs under otherwise equal conditions.

---

<sup>1</sup>During synthesis of the modified DNA strand, the ester group on the phenyl group splits leaving a COO<sup>-</sup> group.

<sup>2</sup>denoted with s for "short"

ref.-name	modified strand (5' to 3') counterstrand (3' to 5')	Number of bp	$T_m$
6GAA	6-GAA AGC GCC ATT CGC CAT TC CTT TCG CGG TAA GCG GTA AG	20	73 °C
6CAA	6-CAA AGC GCC ATT CGC CAT TC GTT TCG CGG TAA GCG GTA AG	20	74 °C
4CAA	4-CAA AGC GCC ATT CGC CAT TC CTT TCG CGG TAA GCG GTA AG	20	72 °C
s6GAA	6-GAA AGC GAT AGC G CTT TCG CTA TCG C	13	50 °C
s6AGA	6-AGA AGC GAT AGC G TCT TCG CTA TCG C	13	47 °C
s6AAG	6-AAG AGC GAT AGC G TTC TCG CTA TCG C	13	47 °C
s6ZAA	6-ZAA AGC GAT AGC G CTT TCG CTA TCG C	13	48 °C
s6(C:Z)AA	6-CAA AGC GAT AGC G ZTT TCG CTA TCG C	13	51 °C
s6AZA	6-AZA AGC GAT AGC G TCT TCG CTA TCG C	13	46 °C
s6AAZ	6-AAZ AGC GAT AGC G TTC TCG CTA TCG C	13	49 °C

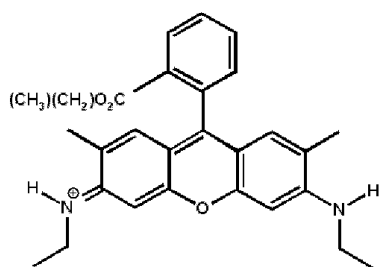
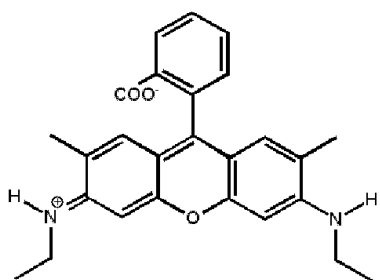
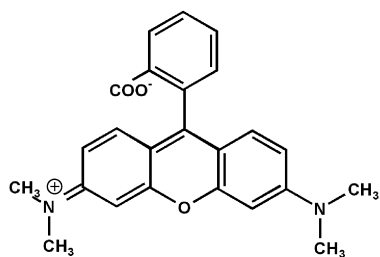
**Table 5.1:** Reference names of Rhodamine capped oligos discussed in this chapter.

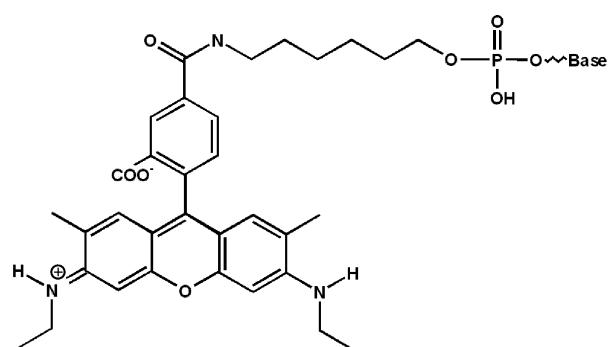
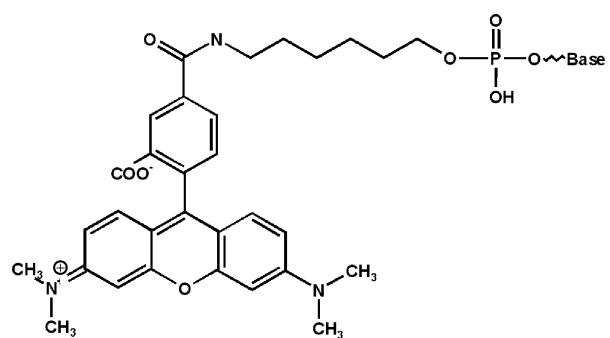
Legend:

6 = R6<sup>+</sup> linked to 5' end of modified strand by C<sub>6</sub> linker

4 = TMR<sup>+</sup> linked to 5' end of modified strand by C<sub>6</sub> linker

Z = 7-deaza-Guanine

(a) R6<sup>+</sup>(b) R19<sup>+</sup>(c) TMR<sup>+</sup>**Figure 5.1:** R6<sup>+</sup>, R19<sup>+</sup> and TMR<sup>+</sup> used as reference samples.

(a) R6<sup>+</sup>-modification(b) TMR<sup>+</sup>-modification

**Figure 5.2:** R6<sup>+</sup> and TMR<sup>+</sup> modifications of the samples presented in Table 5.1. The dyes are attached to the 5' end of the modified strands by a C<sub>6</sub> linker

### 5.1.3 Hybridisation and melting curves

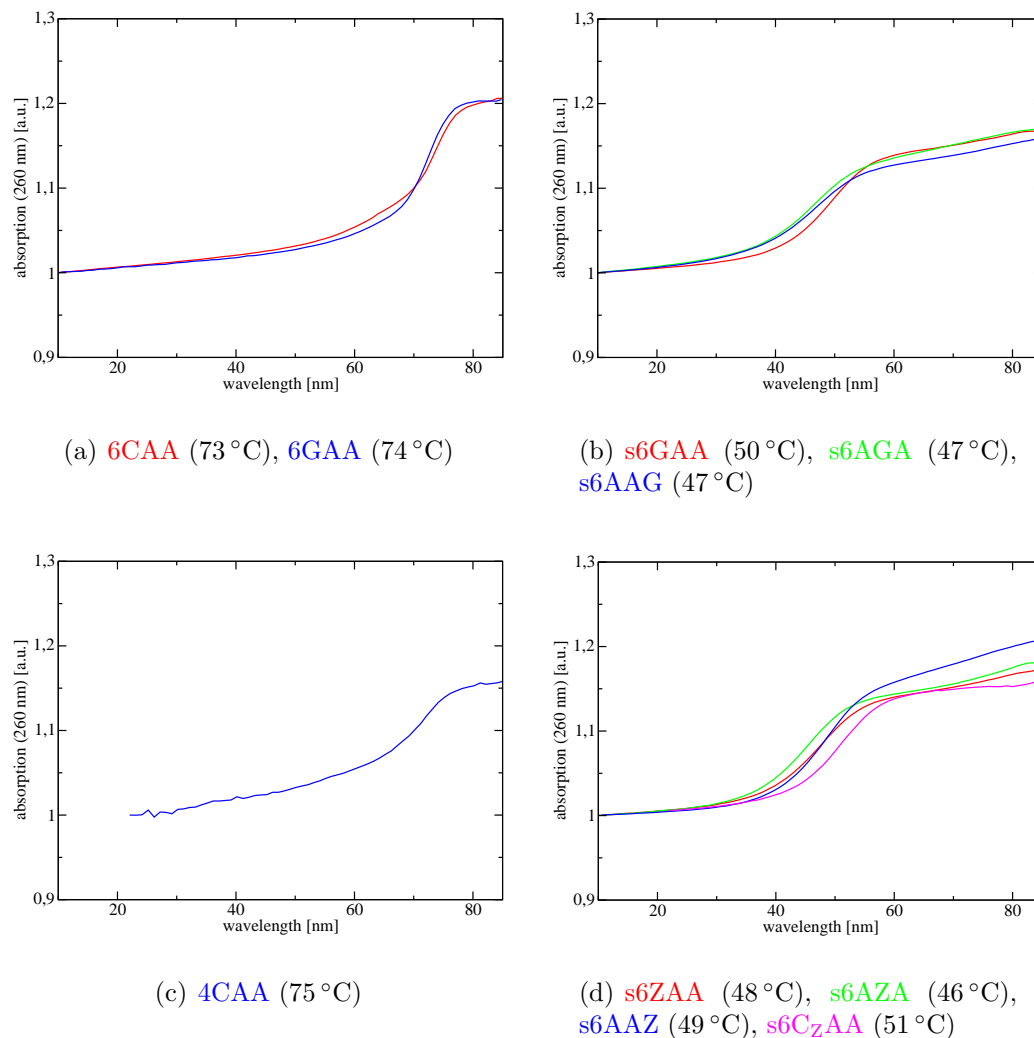


**Figure 5.3:** Melting curves for  $R6^+$  and  $TMR^+$  labeled DNA constructs.  $T_m$  as the maximum of the first derivative is indicated for each sample.

The DNA samples have been hybridised in the pH 7.0 phosphate buffer described in section 5.1.1 at a concentration of 4 mM of single strands. The concentration of counterstrands was in excess by 10 % in order to minimize the presence of non-hybridised modified single strands. After adding the counterstrand to the modified strand, the sample has been heated to 80 °C within  $\approx 45$  min, kept at this temperature for 1 h and then slowly cooled down to RT within hours.



Successful hybridisation and stability of duplexes were checked by determining their melting behaviour. Single stranded DNA has an approximately 40% higher absorption than double stranded DNA at 260 nm, since the heterocyclic rings of the bases absorb more light if they are not piled up or connected by hydrogen bonds inside the double helix. Consequently, duplex formation can be monitored following absorption at 260 nm. This was done under standard conditions at  $OD_{260\text{ nm}} = 1$  on a 1 cm optical path length. The measurements were performed for at least two heating / cooling cycles.

The melting curves of all samples are shown in Figure 5.3. Upon increase of the temperature, the helical structure disintegrates increasing the absorption at 260 nm. The melting points  $T_m$  are defined as the turning point of the sigmoidal curve, their measured values range from 72 to 74 °C for the 20 bp duplexes from 46 to 50 °C for the 13 bp. The melting points of the 13 bp duplexes vary within 5 K, which is in the range of reliability of this method.

#### 5.1.4 NMR-structure

NMR structures of the 20 bp duplexes 6CAA and 4CAA, as well as differential structures of the 13 bp duplexes s6GAA and s6AGA have been resolved. [H. Neubauer and C. Griesingers, Max-Planck-Institute for Biophysical Chemistry, Göttingen]. All samples were examined in the same buffer as the kinetic experiments described in this work at a concentration of  $2.0 \cdot 10^{-3}$  M.

In all cases, B-DNA structure is maintained throughout the base stack. Apart from a minority with a population of up to 15%, the rhodamines take a position in close van der Waals distance on the neighbouring C : G base pair.

The NMR experiment showed interactions between protons of two R6<sup>+</sup> dyes with very high amplitudes in all samples. These signals can only be explained by “head-to-head” dimerization of the R6<sup>+</sup> labeled oligos with the xanthene rings of two dyes in parallel.

For the 6CAA and 4CAA duplexes, two positions of the dye on the base stack are resolved. In the case of 6CAA the relative amplitudes of population had a ratio of 80% and 20% (also within a 10% uncertainty), in the case of 4CAA, the amplitudes of population were about equal. These conformations differ in the position of the dye on the base stack. In one conformation (the 80% majority population for 6CAA), the C<sub>6</sub> linker prolongs the backbone of the modified strand, in the other conformation (the 20% minority population for 6CAA), the linker is rotated by about 90°. Both conformations result in a different position of the xanthene ring of the dyes on the base stack (Figures 5.4 and 5.5).

The < 15% minority population showed no specific interaction of the dye with the base stack. Its position is not predictable by NMR methods.

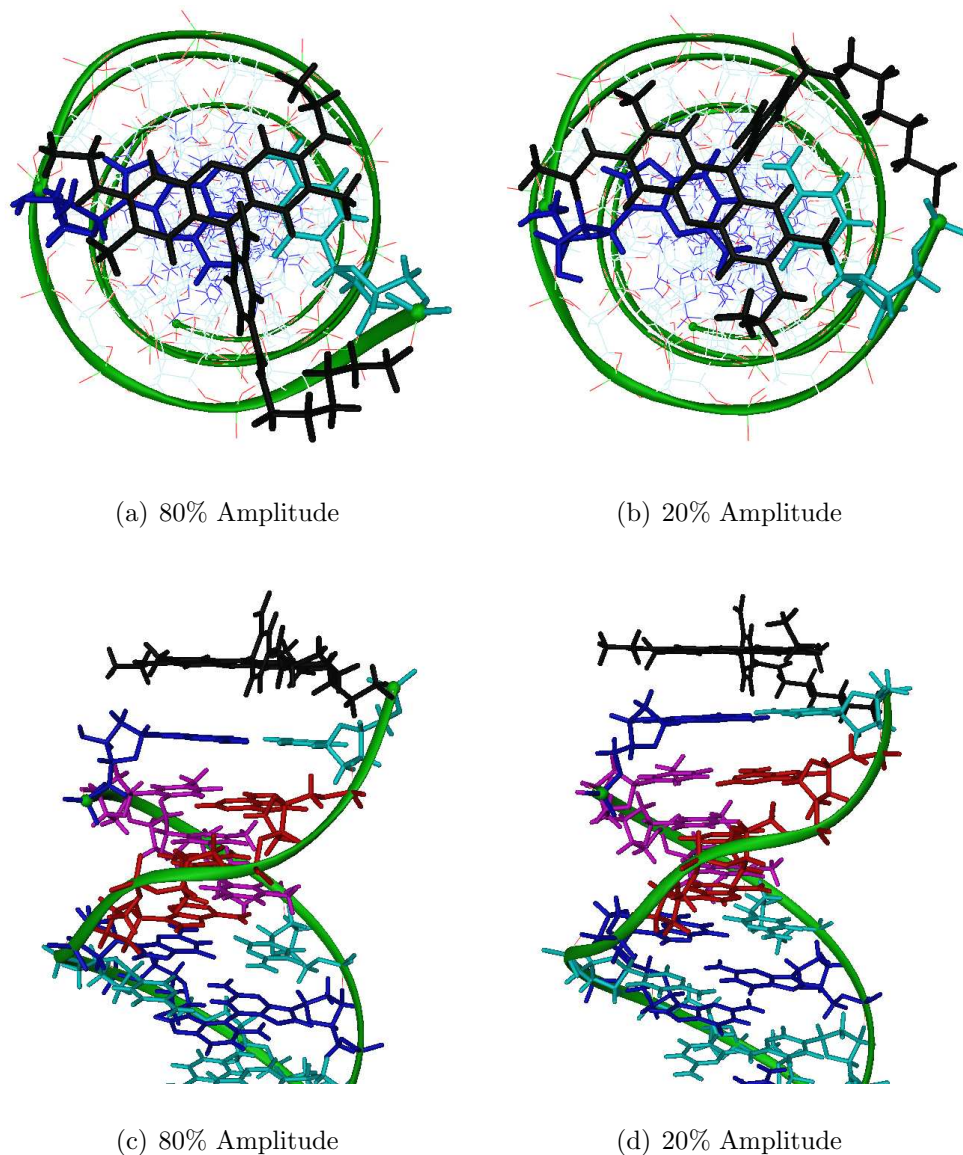


**Figure 5.4:** NMR structure of 6CAA with two conformations.  
Color code: R6<sup>+</sup>, G, C, A, T

The difference structures for s6GAA and s6AGA showed the same two conformations as already resolved for 6CAA and 4CAA with respect to the angle between the linker and the backbone of the modified strand. In contrast

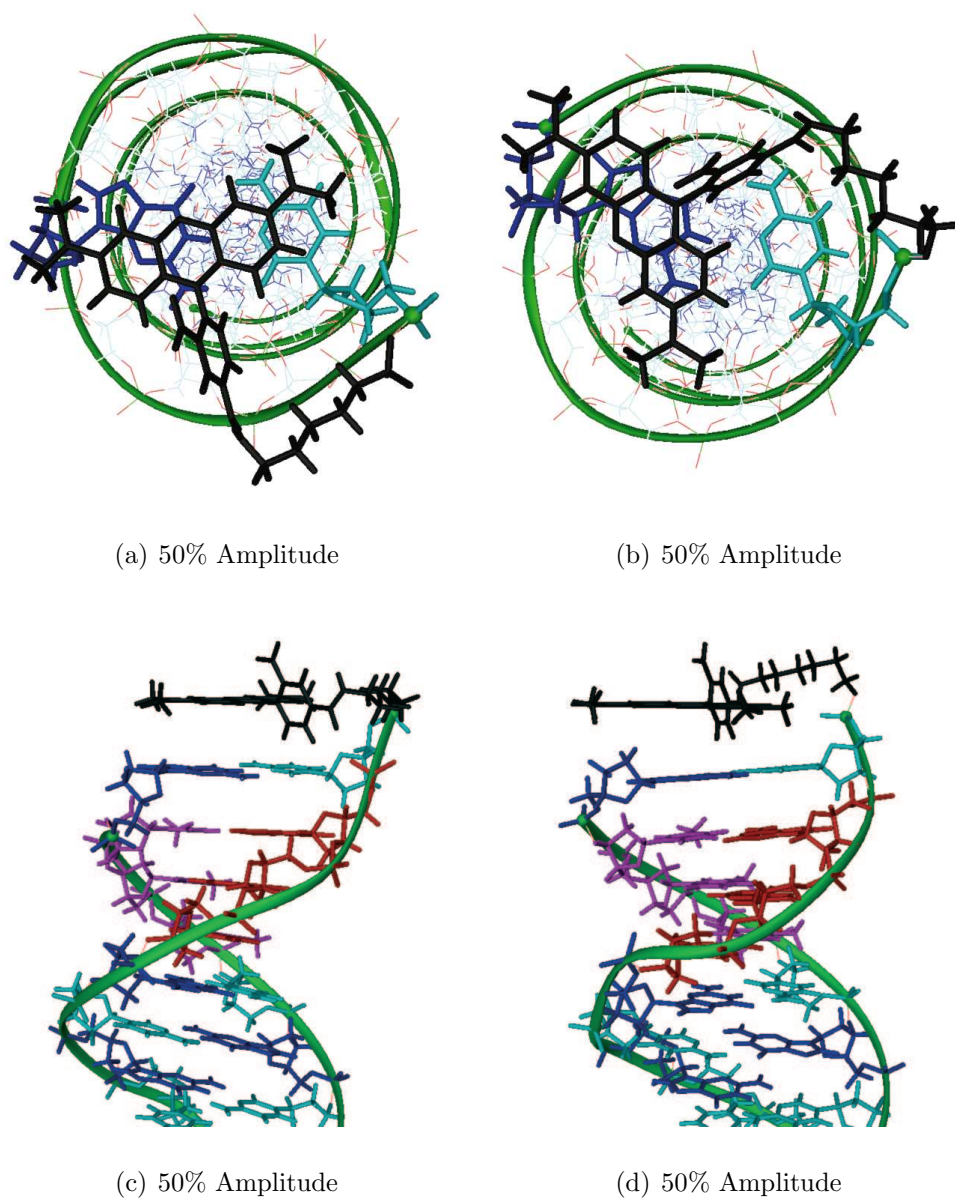


**Figure 5.5:** NMR structure of 4CAA with two conformations.  
Color code: TMR<sup>+</sup>, G, C, A, T

to the long samples, the NMR datasets for the short sequences showed two subpopulations for each of these conformations. The carboxy group on the phenyl ring can be oriented towards the base stack or away from it.

Without further calculation, in a qualitative approach one can predict

different electronic coupling between the dye and its ET partner G for both conformations on the basis of different proximity and orientation. The influence of different orientations of the carboxy group are expected to be minimal.

### 5.1.5 Spectroscopic characterisation

Absorption of  $R6^+$  in aqueous environment at a concentration of  $2 \cdot 10^{-6}$  M peaks at 526 nm with a shoulder around 500 nm. The absorption spectrum of  $R19^+$  is blue shifted by  $180 \text{ cm}^{-1}$  with a center wavelength of 521 nm (Figure 5.6). Fluorescence excitation follows the absorption spectra. Fluorescence emission of  $R6^+$  is centered around 554 nm, of  $R19^+$  around 549 nm, blue shifted by  $160 \text{ cm}^{-1}$ .

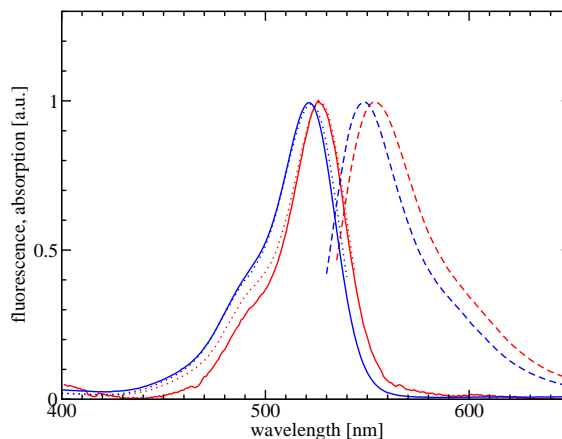


**Figure 5.6:** Absorption (—), fluorescence excitation (···) and emission (---) spectra of  $R6^+$  and  $R19^+$

The shoulder in the absorption spectrum of  $R6^+$  relates to a vibrational progression of  $1100 \text{ cm}^{-1}$ . This assignment is supported by 3 pulse photon echo experiments [61].

An increase of  $R6^+$  concentration leads to an increase of absorption at the position of the vibrational band (Figure 5.7). In [70], this band is assigned to a dimer absorption band, based on absorption spectra taken at a wide range of concentrations. At even higher concentrations, a band at 480 nm is reported to rise, which is assigned to tetramer formation and confirmed by NMR studies [71].

Absorption and fluorescence spectra of the  $R6^+$  labeled DNA duplexes at  $2.5 \cdot 10^{-5}$  M are largely independent of the base sequence (Figure 5.8). The maximum of absorption is red shifted by  $430 \text{ cm}^{-1}$  to 533 nm compared to absorption of  $R19^+$ . The fluorescence maximum of the  $R6^+$  labeled DNA duplexes is at 560 nm.

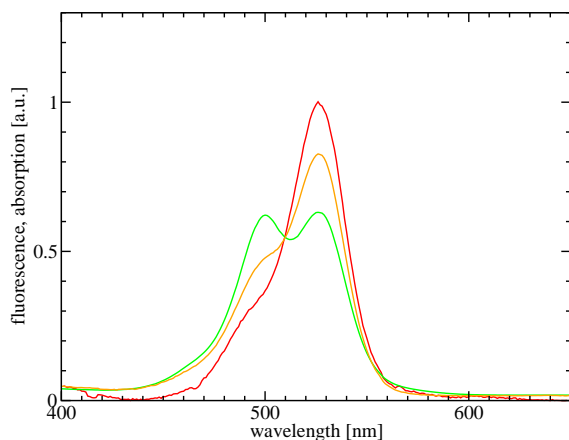


**Figure 5.7:** Absorption spectra of  $R6^+$  at  $2 \cdot 10^{-6} M$ ,  $2.5 \cdot 10^{-5} M$  and  $8.3 \cdot 10^{-5} M$

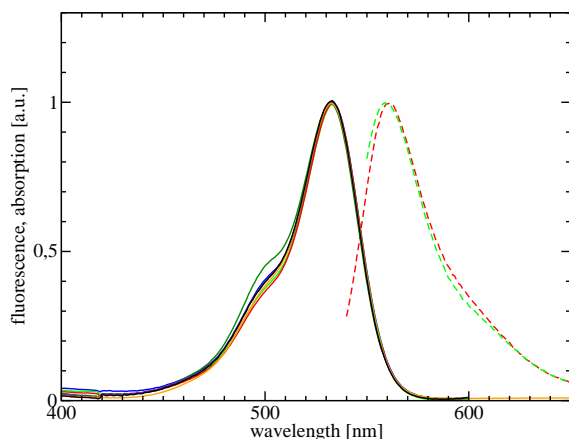


**Figure 5.8:** Absorption (—) and fluorescence (---) spectra of 6CAA, 6GAA, s6GAA, s6AGA, s6AAG, s6CzAA, s6ZAA, s6AZA, s6AAZ. Concentration:  $2.5 \cdot 10^{-5} M$

Taking absorption at 500 nm as a measure for dimer concentration, the tendency towards dimer formation is much less pronounced in  $R6^+$  labeled DNA duplexes (Figure 5.9) than in free  $R6^+$  in solution (Figure 5.7).

The absorption spectrum of  $TMR^+$  in aqueous solution has its maximum at 550 nm, its fluorescence peaks at 578 nm, fluorescence excitation follows absorption (Figure 5.10). The maximum of the absorption spectrum of the  $TMR^+$  labeled duplex 4CAA is red shifted compared to the free dye by  $230 \text{ cm}^{-1}$  to 557 nm. In contrast to  $R6^+$  labeled DNA duplexes, the tendency towards dimer formation is strongly suppressed, as concluded from the magnitude of the shoulder at 510 nm being independent on the concentration in the range from  $1.2 \cdot 10^{-5} M$  to  $2 \cdot 10^{-3} M$ . The fluorescence spectrum of 4CAA peaks at 600 nm, fluorescence excitation also follows absorption.

The red shift of the absorption spectra of both, the  $R6^+$  and  $TMR^+$  modified DNA sequences can be taken as an indication for  $\pi - \pi$  interaction of the

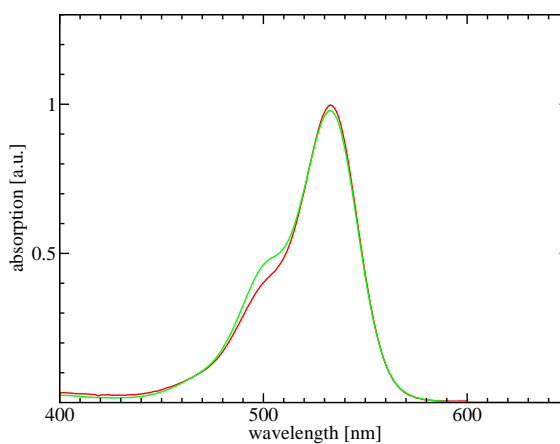


**Figure 5.9:** Absorption spectra of s6AAG at  $2.5 \cdot 10^{-5} \text{ M}$  and  $1.5 \cdot 10^{-4} \text{ M}$

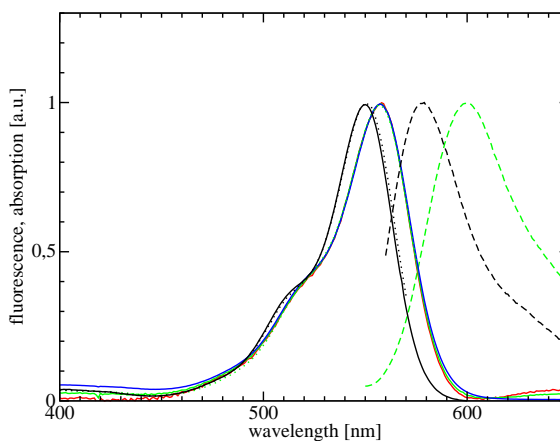


**Figure 5.10:** Absorption (—), fluorescence (---) and fluorescence emission (···) spectra of  $\text{TMR}^+$  at  $2.8 \cdot 10^{-5} \text{ M}$  and 4CAA at  $1.2 \cdot 10^{-5} \text{ M}$ ,  $2.8 \cdot 10^{-5} \text{ M}$  and  $2 \cdot 10^{-3} \text{ M}$

dye and the base stack and, as a consequence, is a spectroscopic indication for capping of the dye [72]. This feature is – in terms of wavenumbers – twice as large for the  $\text{R6}^+$  modified DNA strands as compared to the  $\text{TMR}^+$  modified strand.

### 5.1.6 Redox potentials and driving forces

In order to judge the feasibility of charge transfer reactions between excited  $R6^{+*}$  and nucleobases, the redox potentials of the charge transfer partners are of interest. It is known from quantum-chemical calculations [73] that the oxidation potentials of nucleobases strongly depend on their environment; even replacement of neighbouring bases by other bases (primarily in the 3' direction) can change the ionisation energy by several hundreds of meV. Nevertheless, in the absence of reliable data for the absolute value of oxidation potentials for nucleobases in their respective environment, redox potentials measured in solution have to be used for a first order approximation of driving forces. In [74], C. Seidel systematically investigated the oxidation potentials of nucleosides by cyclovoltammetric experiments in acetonitrile in order to determine the driving force for potential charge transfer reactions with coumarin dyes. The order as in Table 5.2 (G easiest to be oxidised, followed by A) and their relative oxidation potentials are supported by quantum-chemical calculations in [73]. The oldest estimate for 7-deaza-guanine (Z) based on irreversible cyclovoltammetric experiments indicated an oxidation potential of 0.3 V [75]. At present, the most reliable value for the difference between the oxidation potential between G and Z is 0.2 V and derived *in situ* from delayed recombination in DNA of the type stilbene-AAGAZ.

		$E(N^{\bullet+}/N)$ vs. NHE	<b>Table 5.2:</b> Oxidation potentials for nucleobases used in the experiments
guanine	dG	1.47 V	
adenine	dA	1.94 V	
cytosine	dC	2.14 V	
thymine	dT	2.09 V	

Reports on the reduction potential of  $R6^+$  vary on the solvent and range from  $E(R6^+/R6^{\bullet}) = -0.64 \text{ V}_{\text{NHE}}$ <sup>3</sup> in dimethyl formamide (DMA) [76] to  $E(R6^+/R6^{\bullet}) = -0.75 \text{ V}_{\text{NHE}}$  in acetonitrile [67].

Based on the Rehm-Weller equation (3.18) for the charge shift reaction between an excited donor cation  $(D^+)^*$  and a neutral nucleobase **N**, the driving force  $\Delta G$  is:

$$\Delta G = E(N^{\bullet+}/N) - E(D^+/D^{\bullet}) - E_{0,0}(D^+) \quad (5.1)$$

Table 5.3 shows a set of driving forces estimated from an  $E_{0,0}$  transition

---

<sup>3</sup> $E(\text{NHE}) = E(\text{SCE}) + 0.24 \text{ V}$

energy gap<sup>4</sup> between the  $S_0$  and  $S_1$  state of  $R6^+$  (2.25 eV), the oxidation potentials of the bases in Table 5.2 and the lowest reduction potential of the dye.

**Table 5.3:** Driving forces for photo-induced hole injection to nucleobases from  $R6^+$

		$\Delta G$
7-deaza-guanine	Z	-0.23 V
guanine	G	-0.03 V
adenine	A	0.44 V

This estimate suggests that photoinduced ET from G to  $(R6^+)^*$  is possible. It is expected to be faster for Z, while for all other bases ET reactions can be ruled out.

## 5.2 Different modes of kinetic experiments

Femtosecond transient absorption experiments in single wavelength mode (Section 2.1.1) have been used to probe the decay of the excited state and the recovery of ground state depletion following excited state decay and repopulation of the ground state, respectively. This system gives reliable results in time scales from 200 fs to few nanoseconds. At present, this setup is limited to probing wavelengths from about 450 nm to the near infrared at about 950 nm.

To resolve complex kinetics and monitor changes of the difference absorbance spectra, fs-transient absorption experiments in white light mode sensitive to photoproducts absorbing and emitting from 350 nm to 700 nm have been performed on a setup of T. Fiebig<sup>5</sup> [77] which was at our disposal for two months. These experiments give reliable results for kinetics in a range from 100 fs up to tens of picoseconds.

The absorption measurements have been supplemented by fluorescence experiments (Section 2.1.2). Fluorescence techniques are very well suited to accessing data on the decay of the excited state without additional influences from other processes. In addition, our TCSPC setup is very sensitive for processes in the time scale from tens of picoseconds to nanoseconds.

### 5.2.1 Assignment of difference absorbance signals

A reversible photoinduced ET system can – in the simplest case – be described as a 3-level system as shown in Figure 5.11. In this case, the excited  $R6^+$

<sup>4</sup>estimated from the point of intersection between normalized fluorescence and absorption spectra at 550 nm

<sup>5</sup>then at Technical University of Munich



accepts an electron from a nucleobase (G or Z) forming the charge shifted state with an oxidised nucleobase (e.g.  $(R6^\bullet)G^{\bullet+}$ ). Recombination of this charge shifted state populates the ground state (e.g.  $(R6^+)G$ ) (Figure 5.11)

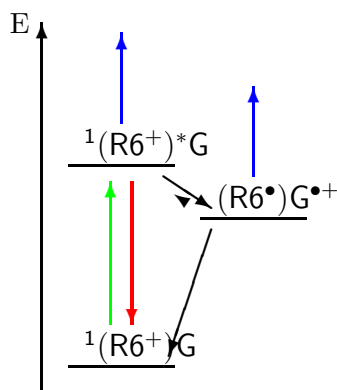


**Figure 5.11:** Scheme for charge injection and recombination. Vertical arrows indicate optical transitions marked in the same color as the corresponding spectral features in Figure 5.12.

These states are visible in the difference absorption experiments. Their spectral characteristics overlap partially and are illustrated in Figure 5.12. Ground state depletion and stimulated emission lead to negative difference absorption ( $\Delta OD$ ) signals, absorption from excited states and products give rise to positive  $\Delta OD$  signals.

**Ground state depletion:** In the spectral region of ground state absorption (i.e. between  $\sim 475$  nm and  $\sim 540$  nm), the difference absorption spectra are dominated by ground state depletion, leading to a negative  $\Delta OD$  signal, which recovers due to repopulation of the ground state. In single wavelength mode, this signal was probed at 520 nm after excitation at 540 nm to exclude influences by stimulated emission not occurring at higher photon energies as the excitation pulse.

**Stimulated emission:** In the region of the fluorescence spectrum (i.e. between  $\sim 550$  nm and  $\sim 650$  nm), the difference absorption spectra are dominated by stimulated emission from the photoexcited  $S_1$  state, also leading to a negative  $\Delta OD$  signal, which decays with the depopulation of the  $S_1$  state. Stimulated emission was probed at 600 nm, where residual influences due to ground state depletion are minimal.

**$S_1$  state absorption:** As reported in [78],  $R6^+$  shows an  $S_{1 \rightarrow n}$  absorption band with a maximum at 428 nm and an extinction coefficient of  $\varepsilon_{1 \rightarrow n} = (4.2 \text{ to } 5.4) \cdot 10^4 \text{ M}^{-1} \text{ cm}^{-1}$  in ethanolic solution detectable as a positive band in the difference absorbance spectrum.

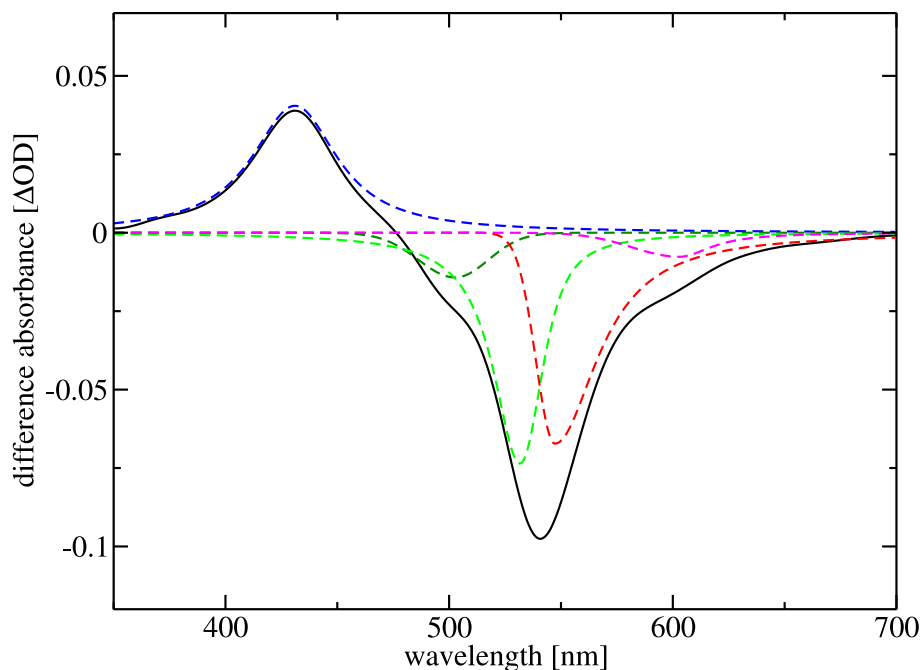


**Figure 5.12:** Difference absorbance spectrum of a non reactive  $R6^+$  tagged DNA sample (s6AAG) taken 200 fs after excitation (—). Assignment of bands:  $(R6^+)^{\bullet}$  and  $R6^{\bullet}$  absorption (---), depletion of  $R6^+$  (---) and stimulated emission from  $(R6^+)^{\bullet}$  (---)

**Neutral radical absorption:** In [79], the absorption of the neutral  $R6^+$  radical was determined in ethanol by pulse radiolysis. Its absorption maximum was reported to be around 410 nm with an extinction coefficient of  $\epsilon_R = 4.8 \pm 0.5 \cdot 10^4 \text{ M}^{-1}\text{cm}^{-1}$ . In case the radical state is populated, this should also be visible as a positive band in the difference absorbance spectrum.

As  $S_1$  state and neutral radical absorption are overlapping each other, experiments in single wavelength mode are not suitable to gain reliable results concerning the processes attributing to these signals.

### 5.2.2 Data analysis

Time traces from difference absorbance experiments in single wavelength mode were analysed by a least square fit of exponential decay functions convolved with a Gaussian function in order to account for the response of the signal as the cross correlation of the excitation and probe pulse. Decay constants in the range of this cross correlation (150 fs) carry an error of a factor

of 2. Decay constants in the ns time scale have an ambiguity in the same order of magnitude, as the system can only probe up to 5 ns after excitation. Between these two extreme situations, the reproducibility of decay constants is in the range of 10%, depending on the multiplicity of decay components.

In order to quantify changes of the difference absorbance spectra recorded in white light probe mode, a band analysis has been performed for each probe position after excitation. Free parameters are the amplitude, center wavelength, width and form<sup>6</sup> of each spectral feature as indicated in Figure 5.12. The complex software package making this analysis possible is maintained by A. Thaller at Technical University of Munich.

For fluorescence experiments in both modes, the instrument response function (IRF) was recorded as the signal of the scattered excitation light. The measured fluorescence signal was deconvoluted with the IRF and then fitted with exponential functions [80]. The reliability of this procedure critically depends on the assumption that the measured IRF corresponds to the “true” IRF for fluorescence. If this is the case, lifetimes shorter than the width of the IRF can still be determined with an ambiguity of a factor of 2. Other lifetimes carry an approximate error of less than 20%.

### 5.3 Excited state dynamics of R6<sup>+</sup> free in solution

The kinetics and spectral changes of R6<sup>+</sup> after photoexcitation have been studied to separate dye intrinsic features from features due to the interaction of the dye with nucleobases. Figures 5.13 (a) and (c) show difference absorbance spectra for various times after excitation at a dye concentration of  $2.5 \cdot 10^{-5}$  M and  $8.3 \cdot 10^{-5}$  M. Figures 5.13 (b) and (d) show the amplitudes of three bands assigned as shown in Figure 5.12.

The positive difference absorption band at 430 nm assigned to excited state absorption in section 5.2.1 undergoes a small red shift by about 1 or 2 nm within about 10 ps. At 475 nm, a clear isosbestic point is visible. In the spectral region of dimer absorption, at 500 nm, the decay pattern of the negative signal differs for the sample at low and at high concentration. This is reflected in a decay of the absorption band for the highly concentrated sample (marked dark-green in Figure 5.13 (d)) faster than for the sample at lower concentration shown in subfigure (b).

The amplitudes of the bands describing ground state bleaching (green) and stimulated emission (red) decay simultaneously for both concentrations.

---

<sup>6</sup>as the weighted sum of a Gaussian and Lorentzian band

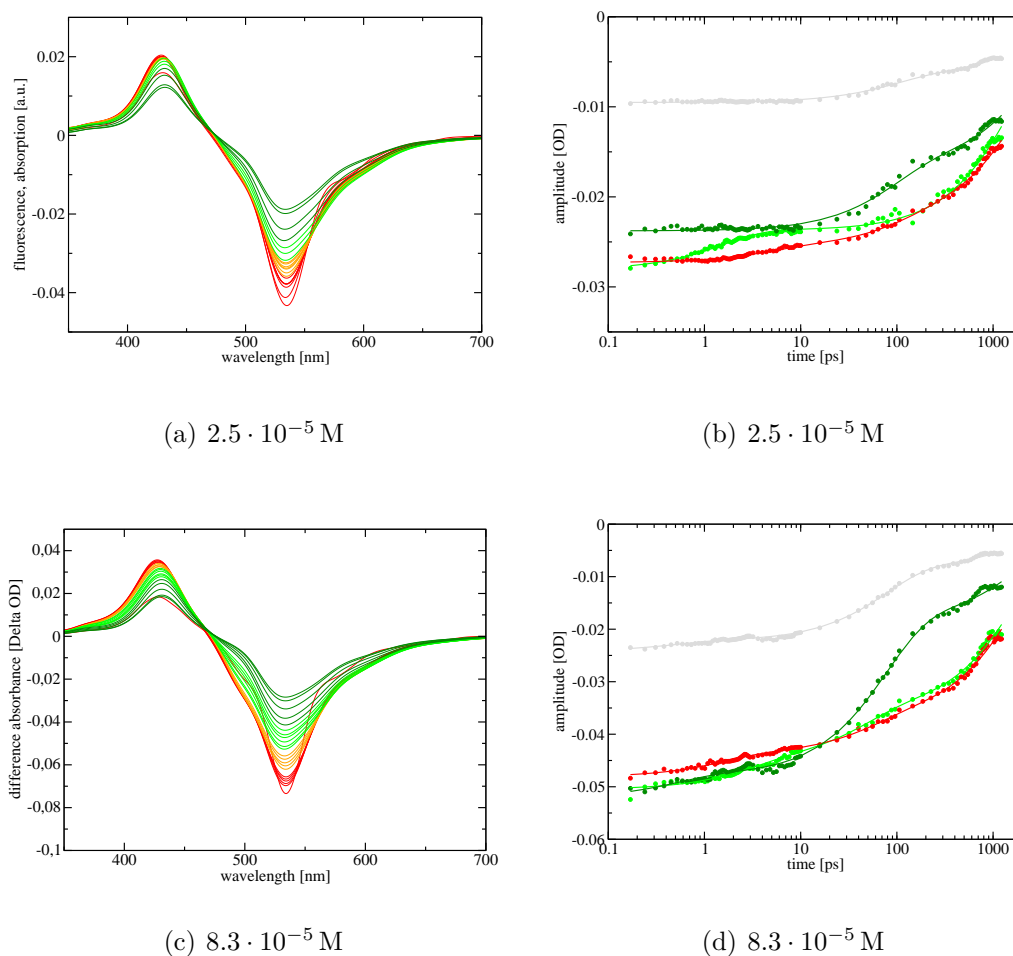


**Figure 5.13:** Left: Difference absorbance spectra of  $\text{R6}^+$  between 100 fs (—) and 2 ns (—) after excitation at 540 nm. Right: Amplitudes of ground state depletion signal (—), stimulated emission (—) and dimer depletion (— and — (with increased amplitude)) as a result of spectral deconvolution fitting procedure. Band assignment as in Figure 5.12

However, at a  $\text{R6}^+$  concentration of  $8.3 \cdot 10^{-5} \text{ M}$ , the decay is faster (on a time scale of 50 ps). As an unusual feature, the spectrum at the red wing of the negative difference absorbance signal changes within the first few ps. Difference absorbance spectra recorded in glycerol at a concentration of  $2.5 \cdot 10^{-5} \text{ M}$  show the same pattern, but on a much slower time scale.

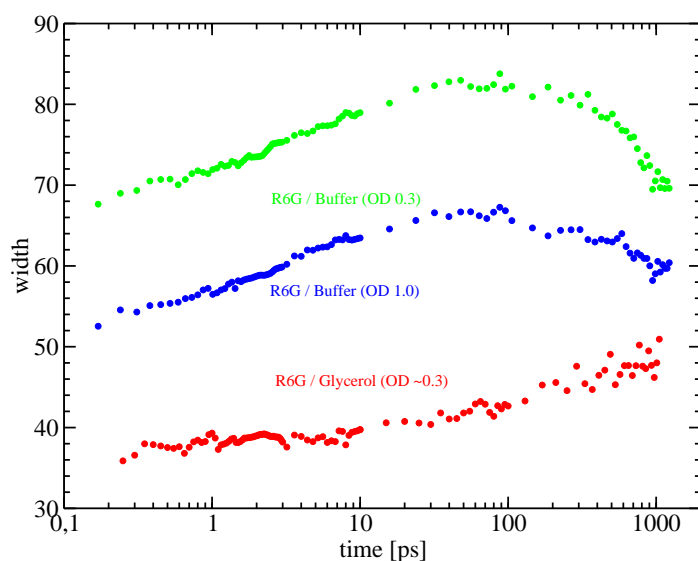


**Figure 5.14:** Width of stimulated emission band as a function of time after excitation for R6<sup>+</sup> in buffer at a concentration of  $2.5 \cdot 10^{-5}$  M and  $8.3 \cdot 10^{-5}$  M and in glycerol at  $2.5 \cdot 10^{-5}$  M

### 5.3.1 Processes in excited state

The change of the stimulated emission spectrum does not coincide with the depopulation of the excited state. This can be concluded from an unchanged amplitude of excited state absorption, ground state bleaching and stimulated emission. The only remaining way to explain this phenomenon is an internal relaxation process within the excited state of R6<sup>+</sup>, which is supported by the red shift of the excited state absorption band on the same time scale.

Already in [81] a change of the difference absorbance spectrum of R6<sup>+</sup> was observed during the first several tens of ps in the wavelength region of stimulated emission. While at around 550 nm, in the minimum of the difference absorbance spectrum, the negative signal decayed faster as the excited state absorption at 430 nm, at wavelengths above 600 nm, the negative signal assigned to stimulated emission actually increased.

Although processes within the excited state of R6<sup>+</sup> are discussed in literature in detail they are still not fully understood. It is surprising that the change of the stimulated emission spectrum, which was published in [81] and reproduced here, is hardly perceived.

As shown in [82], Intramolecular Vibrational Redistribution (IVR) in rhodamines (Rhodamine 700) and oxazines (Oxazine 750) is independent of the solvent and occurs on a 250 fs time scale, much faster than the change of the stimulated emission spectrum.

Fluorescence anisotropy decay of several rhodamine dyes with modification of the substituents on their amino groups at the xanthene ring in various

solvents are studied in [83], where dipolar solvent-solute interactions were found to be at least as important for reorientation dynamics as H-bonding interactions. The finding that H-bonding is larger for dyes, where amino groups are free to rotate and are able to stabilize charges suggests, that these groups could be responsible for relaxation processes within the electronically excited state of the rhodamines.

The phenomenon of excited state relaxation of  $R6^+$  is summarized in [66] and [84], where several models are presented, all of them involving the amino substituents. In all models, its motion is discussed to influence the charge distribution on the xanthene ring and the extent of the conjugated  $\pi$ -system on a time scale shorter than the lifetime of the excited state. These processes could easily change the spectral characteristics of the stimulated emission within several ps in aqueous buffer and explain the strong viscosity dependence:

**TICT** Already in 1951, a twisting motion of the alcyamino group out of the plane of the xanthene ring in the excited state of the chromophore has been proposed by T. Förster in [85]. Later on, this isomerization has been interpreted as a twisted intramolecular charge transfer (TICT) state [86,87]. In this twisted state, the resonance conjunction between the xanthene ring and the amino moiety is broken and the amino link acquires single bond character, resulting in a charge transfer from the amino group to the xanthene ring system. So far, the existence of a TICT state has not been supported spectroscopically for rhodamine dyes.

**Solvent induced 2-level interaction** In [88] and [89] a transition between energetically close excited singlet states induced by a change of the configuration of the amino group is proposed. This model could explain separate fluorescence patterns for the different excited states.

**ULM** Similar to the above mentioned model, a change between two mesomeric states of the amino group are proposed resulting in an “umbrella like movement” (ULM) [90–92]. Similar to the TICT model, the bond between the nitrogen and the xanthene ring carries either single or double bond character influencing the dye - solvent interaction.

**Steric hindrance of rotation** In [93], dual decay patterns of fluorescence have been reported for Rhodamine B in a mixture of glycerol and water ( $\tau_{\text{fast}} = 0.85 \text{ ns}$  and  $\tau_{\text{slow}} = 1.7 - 3.4 \text{ ns}$ ).

### 5.3.2 Dimer formation

The fast decay of the difference absorbance signal in the highly concentrated sample is interpreted as due to dimer formation. This is justified by both the spectral signature – the changes are most prominent in the spectral region of the dimer absorption – and by the fact, that dimers are reported to have decreased fluorescence lifetime [94]. Although the fluorescence lifetime of dimers is reported to be on the ps time scale, the decay of this spectral feature is slower by a factor of 10.

## 5.4 Kinetic characterisation of modified oligomers

### 5.4.1 Femtosecond transient absorption spectroscopy

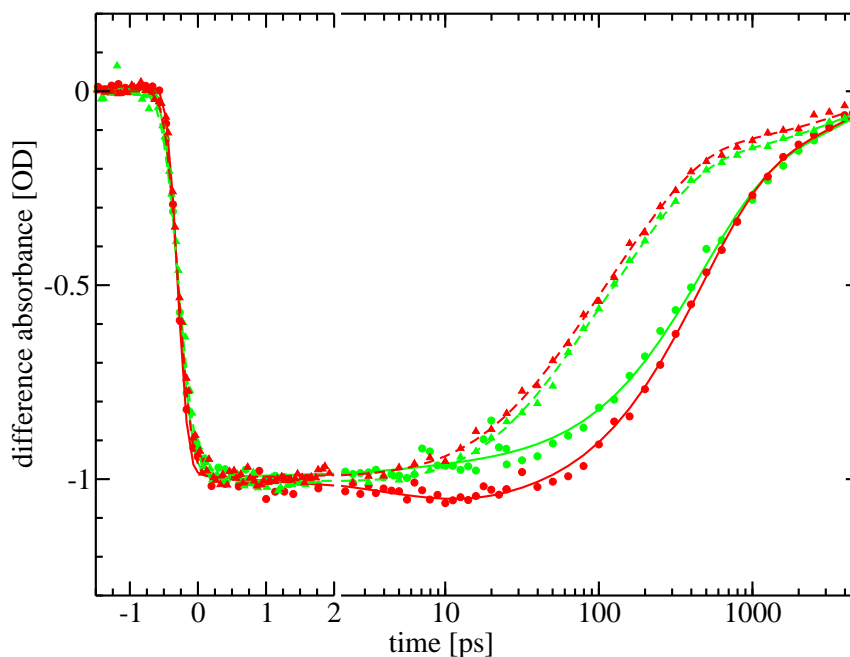


**Figure 5.15:** Difference absorbance signals of 6CAA ( $\circ$ , —) and 6GAA ( $\Delta$ , ---) probing recovery of ground state (520 nm) and stimulated emission (600 nm) with best fits:

6CAA: 600 nm: 5 ps (9%), 468 ps (-77%), 4.1 ns\* (-23%); 520 nm: 406 ps (-74%), 4.1 ns\* (-26%)

6GAA: 600 nm: 80 ps (-52%), 288 ps (-34%), 3.7 ns (-14%); 520 nm: 100 ps (-55%); 247 ps (-26%); 3.7 ns (-19%)

All  $R6^+$  and  $TMR^+$  modified duplexes were characterized by difference absorption experiments in single wavelength mode in order to study the nature of charge injection by the excited dye. The experiments have been performed at a concentration of  $2.5 \cdot 10^{-5}$  M and an excitation wavelength of 540 nm. Experimental time traces and their best fits are presented in Figures 5.15 to 5.19. The results of the best fits (Section 5.2.2) are indicated in the captions and discussed later together with the results from fluorescence experiments<sup>7</sup>.

<sup>7</sup>The ns component was determined by fluorescence experiments and enters the fit as



For samples with a lifetime clearly longer than 50 ps, the time traces probing stimulated emission at 600 ps increase with a time constant of 5 ps. This effect is due to the change of the stimulated emission spectrum as discussed in section 5.3. Apart from this phenomenon, the stimulated emission and ground state recovery signals show the same decay pattern for all samples, except where R6<sup>+</sup> is in direct contact with Z.

G in nearest neighbour position to R6<sup>+</sup> leads to reduced excited state lifetime as compared to the free dye in solution (4 ns). While the lifetime of 6CAA is around 430 ps with an 80% amplitude and a remaining 4 ns component, excited state lifetime of 6GAA – where the G next to the dye is on the modified strand – is considerably shorter and has to be described by a tri exponential decay function (Figure 5.15).

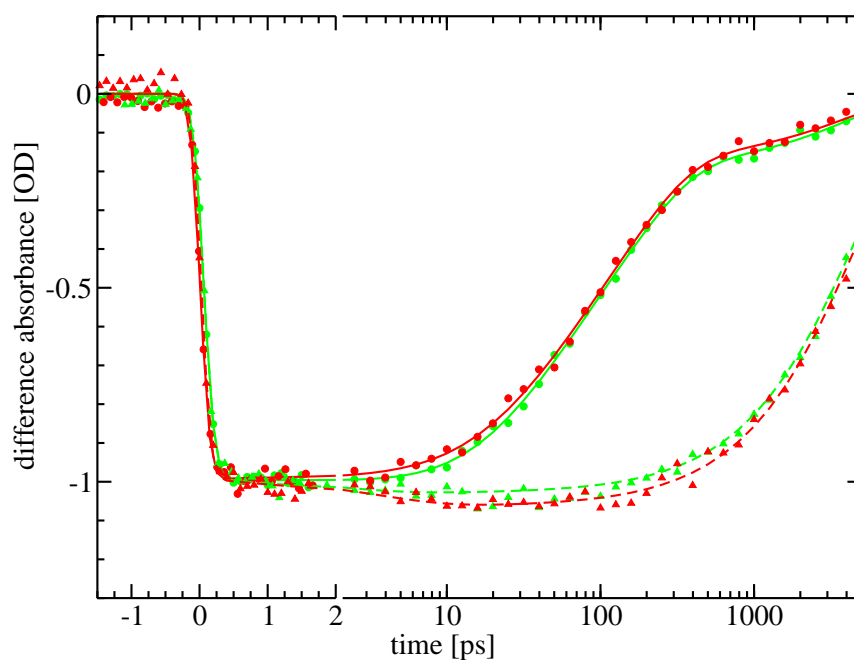


**Figure 5.16:** Difference absorbance signals of s6GAA ( $\circ$ , —) and s6AGA ( $\triangle$ , ---) probing recovery of ground state (520 nm) and stimulated emission (600 nm) with best fits:

s6GAA: 600 nm: 55 ps (-31%), 159 ps (-51%), 2.2 ns\* (-18%); 520 nm: 58 ps (-15%), 116 ps (-62%), 2.2 ns\* (-23%)

s6AGA: 600 nm: 3.8 ns (-100%); 520 nm: 3.8 ns (-100%)

The influence of 13 bp and 20 bp sequences is negligible, as reflected in the  


---

a fixed quantity marked\*

comparable time traces for 6GAA (Figure 5.15) and s6GAA (Figure 5.16). In sample s6AGA, G is placed at the next nearest neighbour position to  $R6^+$ , separated by a single A : T base pair. Charge injection is not observable for this sample as its lifetime corresponds to the natural lifetime of the chromophore. The same holds true for s6AAG with two A : T base pairs between the dye and G (data not shown).

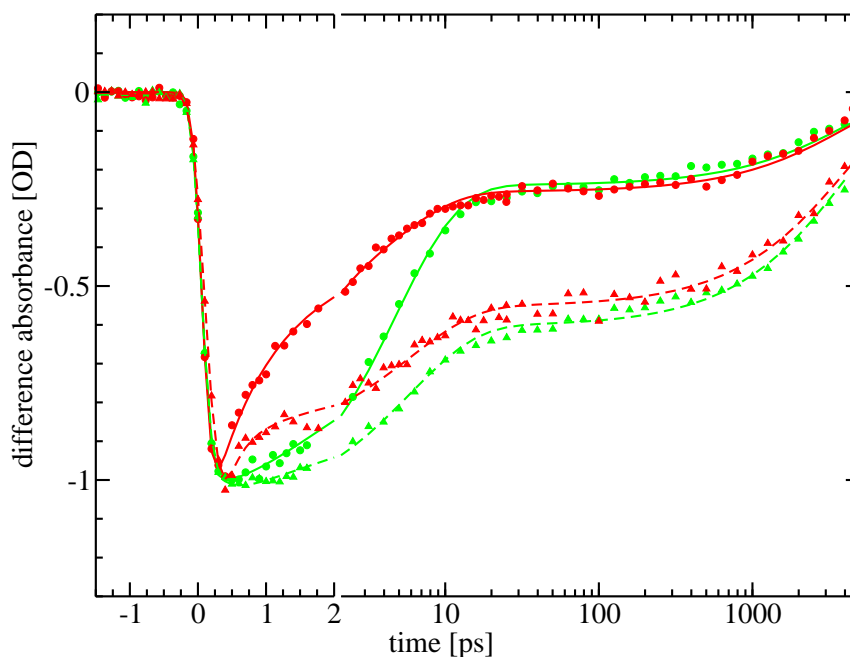


**Figure 5.17:** Difference absorbance signals of s6ZAA ( $\circ$ , —) and s6C<sub>Z</sub>AA ( $\triangle$ , ---) probing recovery of ground state (520 nm) and stimulated emission (600 nm) with best fits:

s6ZAA: 600 nm: 1.0 ps (-80%), 2.8 ns, (-20%); 520 nm: 5.2 ps, (-76), 2.8 ns (-24%)

s6C<sub>Z</sub>AA: 600 nm: 4.2 ps (-43%), 4.0 ns (-57%); 520 nm: 6.7 ps(-43%), 4.0 ns (-57%)

Replacement of G by Z leads to a drastic decrease of excited state lifetime of the charge injector. In the samples s6ZAA and s6C<sub>Z</sub>AA, where Z is in direct contact with the dye, the ground state recovers more slowly than stimulated emission from the excited state. The amplitude of the ns background component of s6C<sub>Z</sub>AA is by a factor of 2 higher than for all other samples where charge injection is observed (Figure 5.17).

For s6AZA charge transfer to the next nearest neighbour could be ob-

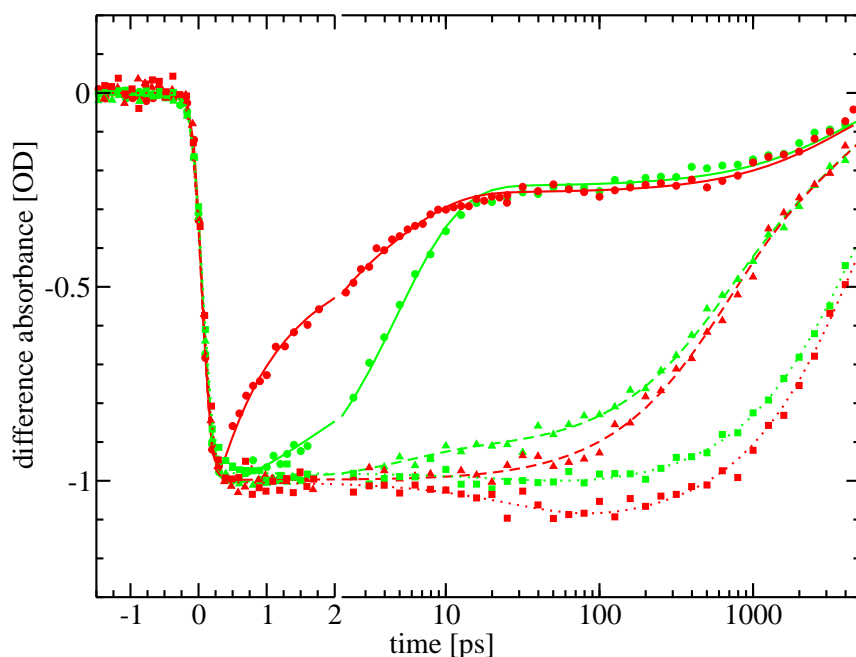


**Figure 5.18:** Difference absorbance signals of s6ZAA ( $\circ$ , —), s6AZA ( $\Delta$ , ---) and s6AAZ ( $\square$ ,  $\cdots$ ) probing recovery of ground state (520 nm) and stimulated emission (600 nm) with best fits:

s6ZAA: as before

s6AZA: 600 nm: 621 ps (-59%), 4 ns\* (-41%); 520 nm: 8.1 ps (-8%), 521 ps (-47%) 4 ns\* (-45%)

s6AAZ: 600 nm: 4.9 ns (-100%); 520 nm: 4.9 ns (-100%)

served (Figure 5.18). This is in contrast to s6AGA where G is not replaced by Z. Excited state lifetime of s6AAZ is not quenched by a charge injection process and comparable to the fluorescence lifetime of the free dye in solution.

Difference absorption data for 4CAA, where the  $R6^+$  is replaced by  $TMR^+$  as compared to 6CAA, had to be fitted bi-exponentially (in addition to the rise component due to relaxation within the excited state) for stimulated emission. An additional short component had to be included in the fit for the recovery of the ground state (Figure 5.19). In contrast to  $R6^+$  labeled DNA samples, no reference sample to 4CAA was available, where fluorescence lifetime of  $TMR^+$  is not quenched by charge injection. Free  $TMR^+$  in solution, however, shows comparable time trace as e.g. s6AAG, however with an excited state lifetime lower by a factor of about 2.

Other than for  $R6^+$  modified oligomers, the difference absorbance time

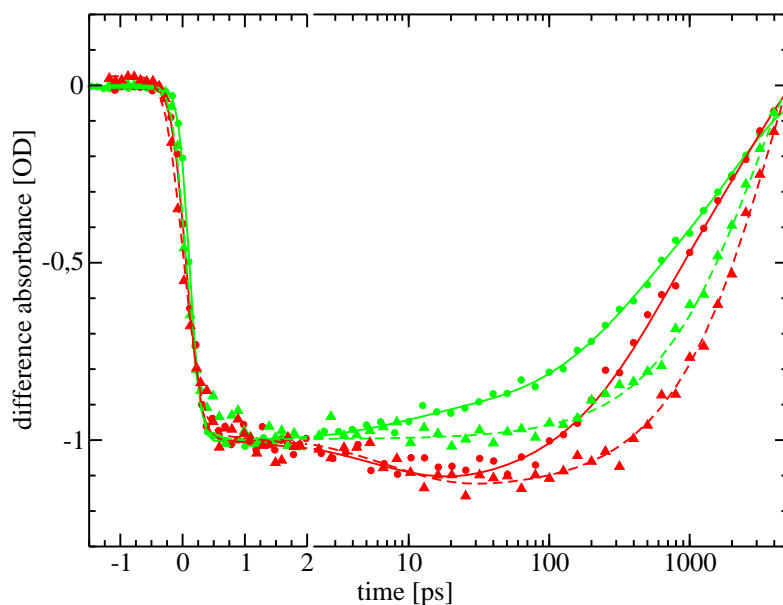


**Figure 5.19:** Difference absorbance signals of 4CAA ( $\circ$ , —) and TMR<sup>+</sup> ( $\Delta$ , ---) probing recovery of ground state (520 nm) and stimulated emission (600 nm) with best fits:

4CAA: 650 nm: 6.5 ps (12%), 358 ps (-40%), 2.3 ns\* (-60%); 520 nm: 8.3 ps (-8%), 267 ps (-40%), 2.3 ns\* (-60%)

TMR<sup>+</sup>: 650 nm: 7.8 ps (10%), 2.3 ns (-100%); [520]nm: 2.3 ns\* (-100%)

traces for TMR<sup>+</sup> and 4CAA had to be fitted with a constant offset of about 10%. This is in agreement with recent literature reporting a triplet quantum yield of 9% for TMR<sup>+</sup> in MeOH [95].

## Difference absorbance spectra

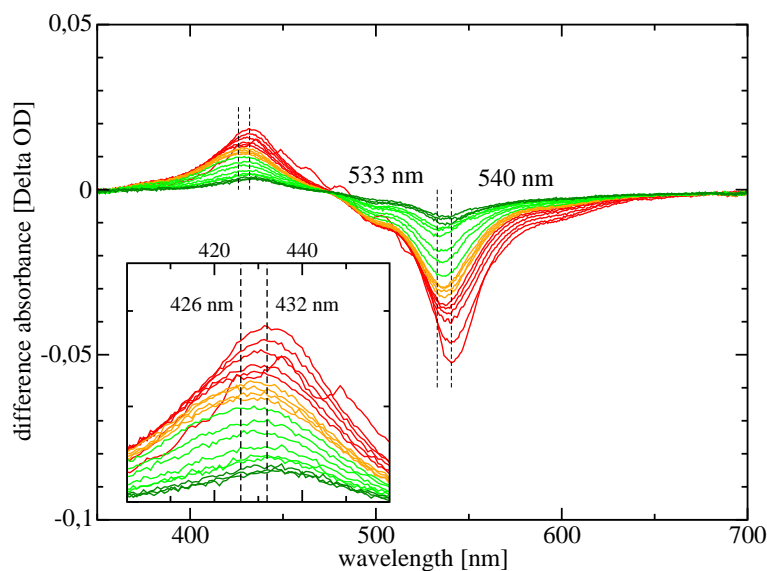


**Figure 5.20:** Difference absorbance spectra of s6ZAA at 100 ps to 1 ns after excitation at 540 nm

When recombination of the charge shifted state is slower than the decay of the excited state it is possible to observe absorption of the neutral  $R6^\bullet$  radical. In contrast to all other  $R6^+$  labeled samples, the transient difference absorption spectra of s6ZAA exhibit a blue-shift of the band at 430 nm by 2 nm within 1 ps after excitation. In the following 5 ps, this process is reverted (Figure 5.20).

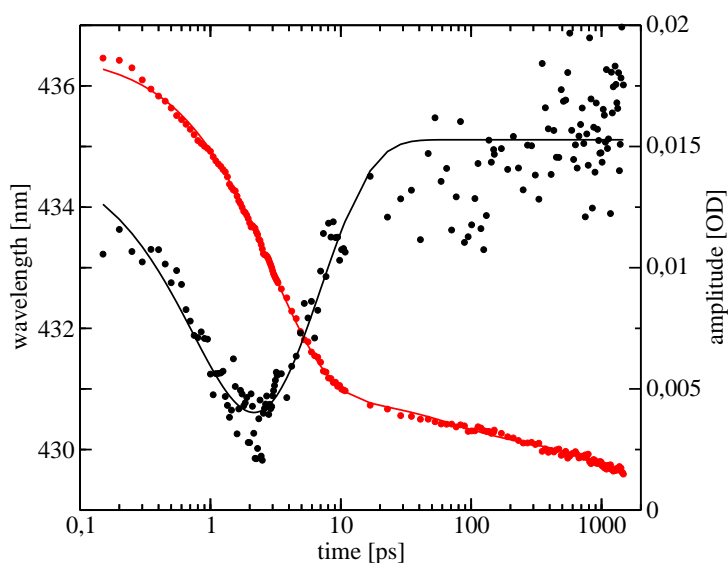
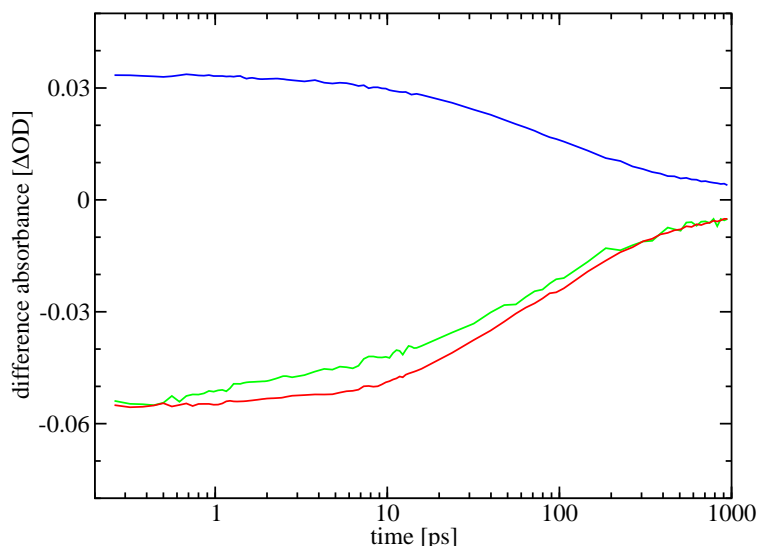


**Figure 5.21:** Position (●) and amplitude (●) of induced absorption band of s6ZAA

This feature is reflected in Figure 5.21 where the center wavelength and amplitude of the band are plotted as a function of time. Simultaneously to the blue shift of the band at 430 nm, the minimum of the difference absorbance spectra shifts from 540 nm to 533 nm. This is regarded as an effect of different relative amplitudes of stimulated emission and ground state bleaching.

Transient absorption time traces in single wavelength mode showed simultaneous decay of stimulated emission and repopulation of the ground state for all samples except when Z was in nearest neighbour position to R6<sup>+</sup>. However, the time traces for stimulated emission are also influenced by an excited state relaxation process, so that this interpretation is questionable. As this information is crucial for the understanding of the charge injection process, band analysis has been performed on the difference absorbance spectra of s6GAA confirming simultaneous decay of stimulated emission and ground state recovery (Figure 5.22).

**Figure 5.22:** Amplitudes for excited/radical state absorption (—), ground state bleaching (—) and stimulated emission (—) of s6GAA as a result of band analysis.



### 5.4.2 Time resolved fluorescence experiments

Transient difference absorbance experiments are impeded by two limitations: (i) To minimize influences by ground state bleaching, stimulated emission has to be probed on the red wing of the stimulated emission spectrum. In this spectral region, there can be significant influence from the spectral changes due to relaxation processes within the S<sub>1</sub> state of R6<sup>+</sup>. (ii) The time resolution on a high 100 ps time scale is limited, as difference absorbance is probed on time intervals exponentially increasing with time after excitation. The

samples which are suitable for fluorescence experiments (i.e. of which excited state has a lifetime longer than 20 ps) have been studied with time resolved fluorescence techniques.

To study the origin of the ns background component observed for all samples, fluorescence depolarisation experiments (Section 2.1.2) have been performed on s6AZA and on s6AAG and R6<sup>+</sup> as reference.

Fluorescence decay of 6CAA is shown in Figure 5.23 together with residuals for bi- and tri-exponential fits. In contrast to transient absorption experiments, where no third decay component could be resolved (Figure 5.15), a tri-exponential fit is in much better agreement with experimental data.

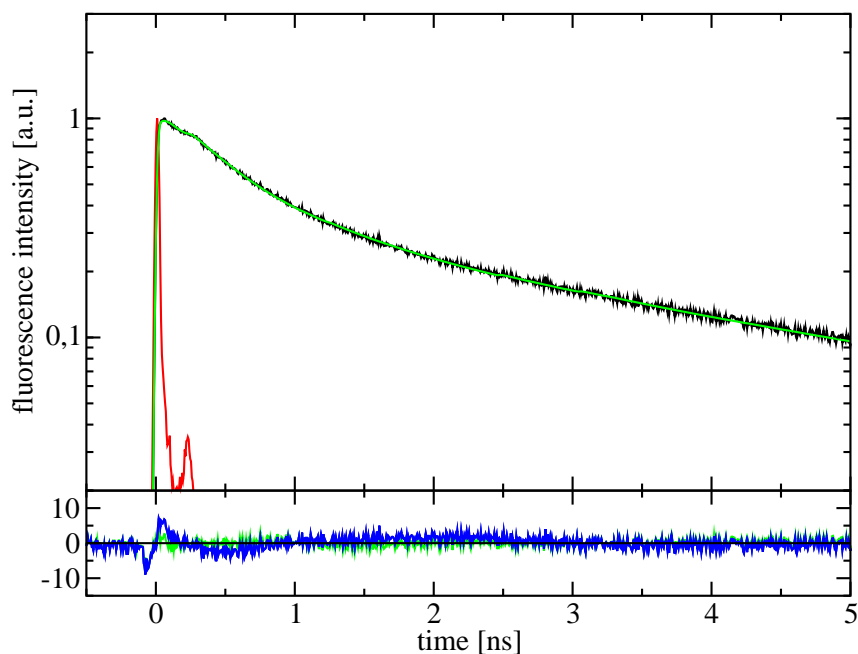


**Figure 5.23:** Top: Fluorescence decay of 6CAA  
 Bottom: Residuals for bi- (—) and tri- (—) exponential fits.  
 Result of fit: 176 ps (31%), 629 ps (47%), 4.1 ns (22%)

For s6GAA, transient absorption experiments could resolve a third decay component (Figure 5.16). This is confirmed by fluorescence experiments (Figure 5.24).

Transient absorption experiments on s6AZA could only resolve a bi-exponential decay pattern (Figure 5.17) on a time scale as 6CAA. Time resolved fluorescence experiments had to be fitted tri-exponentially (Figure 5.25).

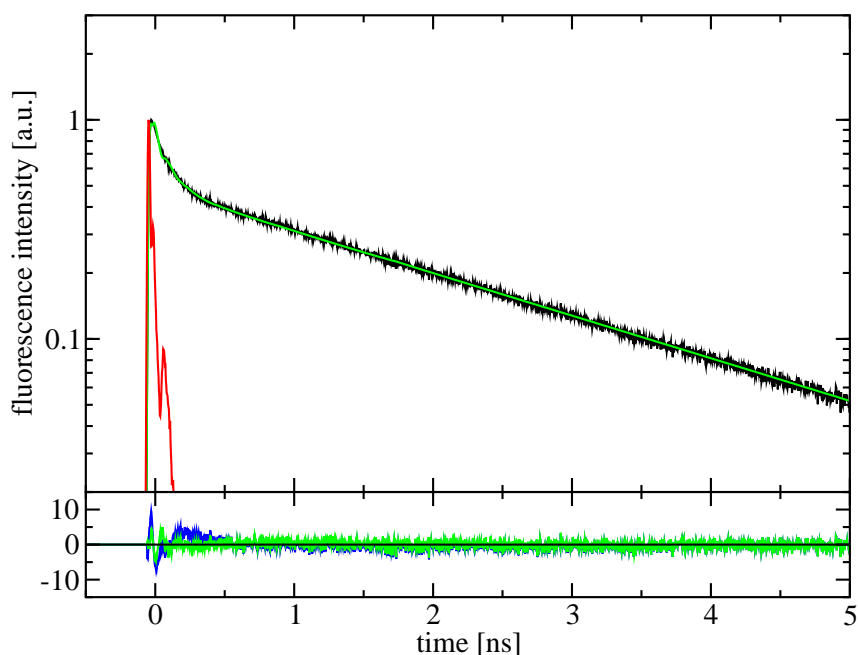


**Figure 5.24:** Top: Fluorescence decay of s6GAA  
 Bottom: Residuals for bi- (—) and tri- (—) exponential fits.  
 Result of fit: 30 ps (71%), 140 ps (11%), 2.2 ns (18%)

In contrast to  $R6^+$ , fluorescence decay of  $TMR^+$  had to be fitted biexponentially. Fluorescence decay of the  $TMR^+$  labeled oligomer 4CAA was also biexponentially (Figure 5.28).

### Fluorescence anisotropy

As the ns component of s6AZA had a rather high amplitude in the transient absorption measurements compared to other modified DNA strands, it was chosen as an example to study the origin of this component. Obviously, the ns component is due to  $R6^+$  not efficiently quenched by charge transfer to Z. This can have two reasons: (i) it cannot be excluded that part of the dyes are not attached to the DNA strands or (ii) as already seen in NMR experiments, a certain percentage of the dyes do not reside on the top of the base stack but take a non-specified position with less favoured charge injection properties.

The rotational diffusion pattern for both situations is expected to be different. Whereas in situation (i) the rotational diffusion of the ns component should reflect the one of the free dye, in situation (ii) rotation should be



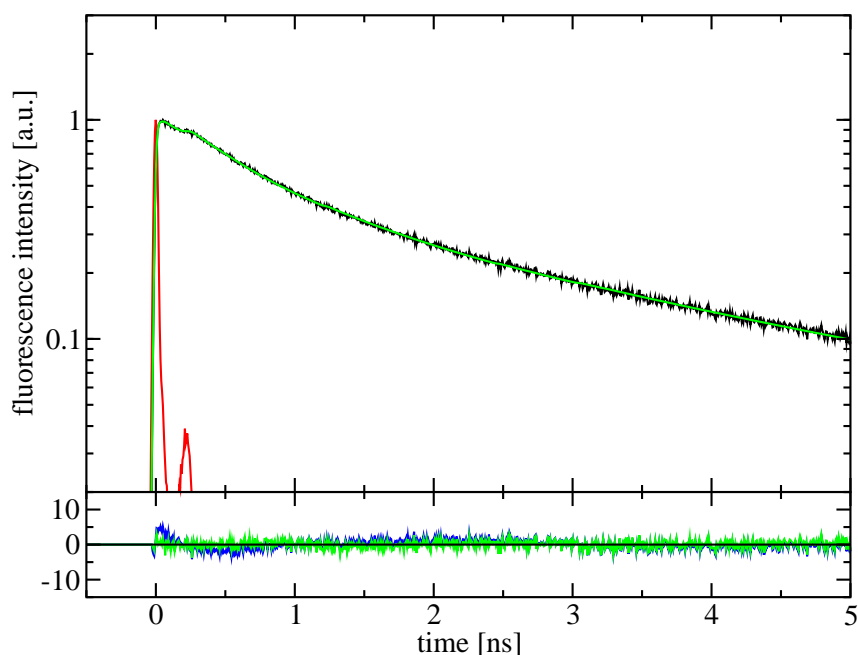


**Figure 5.25:** Top: Fluorescence decay of s6AZA  
 Bottom: Residuals for bi- (—) and tri- (—) exponential fits.  
 Result of fit: 260 ps (24%), 774 ps (47%), 3.7 ns (29%)

slowed down as the dye is still attached to the much larger DNA duplex.

Figure 5.26 shows the results from fluorescence depolarisation experiments for  $R6^+$  and s6AAG, where the majority of fluorescence is expected to be due to dyes attached to the DNA strand. The lower part of both subfigures shows the anisotropy  $r$  as calculated from the fluorescence signal with a polarisation parallel and perpendicular to the polarisation axis of the excitation beam.

Whereas the anisotropy of  $R6^+$  decays monoexponentially with a time constant of 216 ps, anisotropy of s6AAG becomes biexponential and is considerably slower with decay constants of 400 ps and 4.9 ns with relative amplitudes of 39% and 61%, respectively. These time constants are attributed to rotational relaxation times of the oligomer.

As the anisotropy decays with time constants and relative amplitudes of 620 ps (40%) and 1.9 ns (60%) and is therefore considerably slower than for free  $R6^+$ , contamination by unbound dye can be ruled out. However, reduction of the long anisotropy decay time by a factor of 2 could be caused by dyes with additional degrees of freedom compared to chromophores located

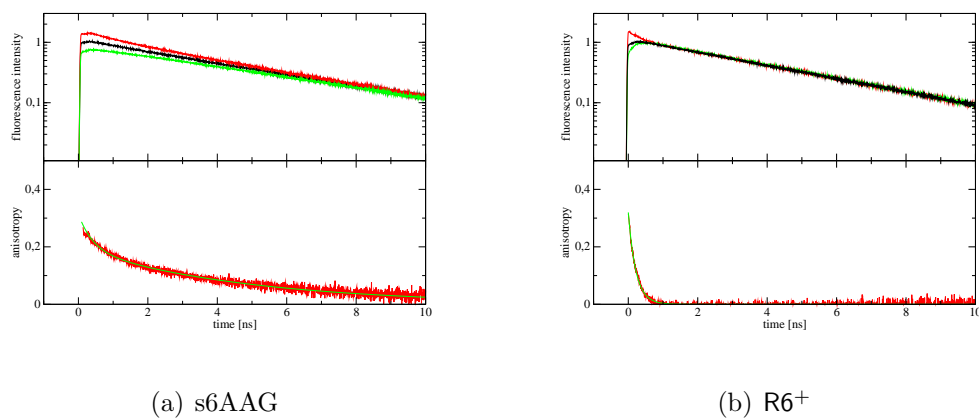


**Figure 5.26:** Top: Fluorescence decay at magic angle (—) (orthogonal —, parallel —)  
Bottom: Anisotropy decay

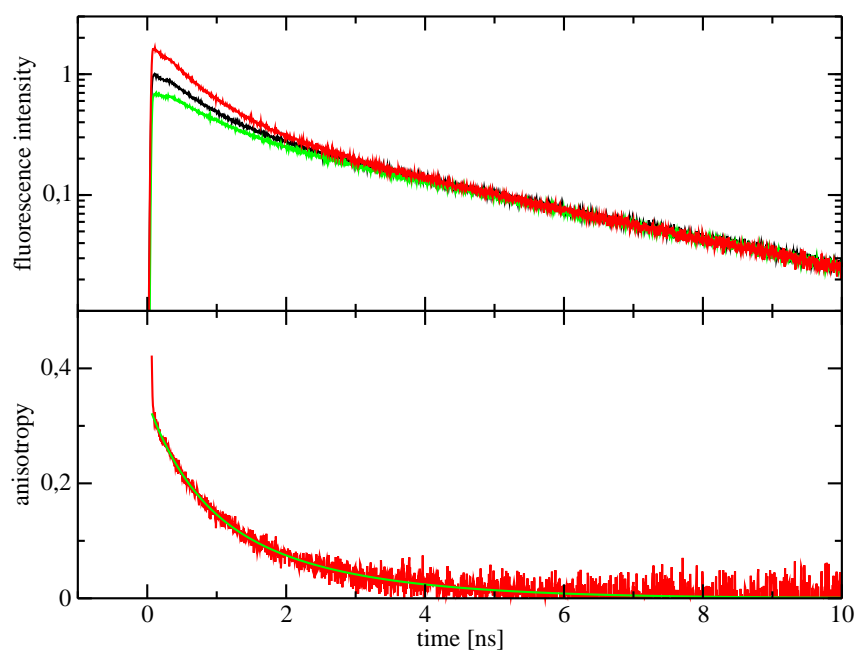


**Figure 5.27:** Top: Fluorescence decay of s6AZA at magic angle (—) (orthogonal —, parallel —)  
Bottom: Anisotropy decay

on top of the base stack.

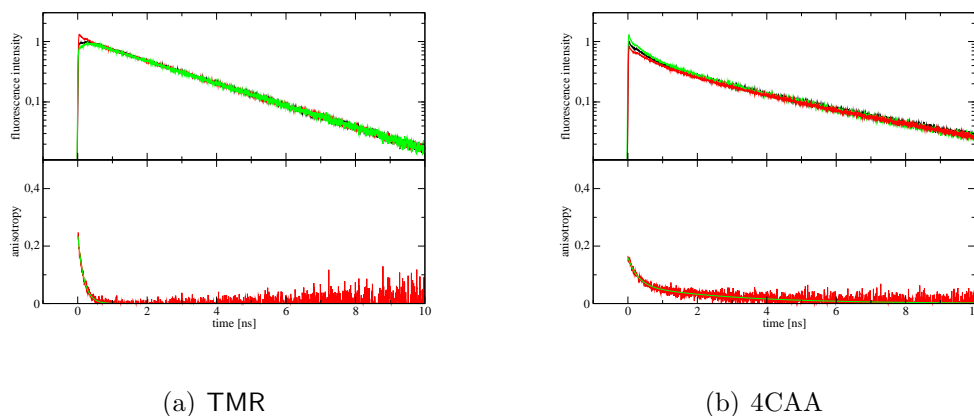


**Figure 5.28:** Top: Fluorescence decay at magic angle (—) (orthogonal —, parallel —)  
Bottom: Anisotropy decay

As shown in the lower part of Figure 5.28 (a), fluorescence anisotropy decay of  $\text{TMR}^+$  is monoexponential and with 179 ps on the same time scale as the one for  $\text{R6}^+$  free in solution. Fluorescence anisotropy of 4CAA decays bi-exponentially with time constants of 286 ps (60%) and 2.9 ns (40%). In analogy to the experiments with  $\text{R6}^+$  labeled DNA duplexes, this points to a larger component of non-capping dyes.

### Temperature dependent experiments

To study the energetics of charge injection dynamics, temperature dependent fluorescence experiments have been performed. Due to the low melting points of the 13 bp duplexes, the temperature window is limited towards higher temperatures. As a consequence, temperature dependence can only be examined towards lower temperatures. Especially for semi-endcapped systems as investigated here, any change of the environment is critical. As the buffer forms ice crystals below 270 K, the micro environment of the duplexes can change dramatically. To increase glass formation, the samples have also been studied in a 35% sucrose solution. NaCl concentration was increased to 500 mM to maintain duplex stability. As both results are divergent, they are not reliable enough to be used for further considerations.

## 5.5 Results

The results of transient absorption and time resolved fluorescence experiments are summarized in Tables 5.4 and 5.5. In these tables, the most reliable results are highlighted as the basis for further discussion. As the fs-transient absorption experiments are not very sensitive on the ns time scale, this component entered the fit as a fixed component\* when derived from fluorescence decay.

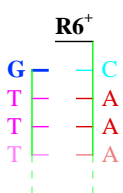
Table 5.4 compares  $R6^+$  in direct neighbourhood with C and G, Table 5.5 the distance dependence of hole injection and influences of replacement of G by Z.

For all sequences, a background signal in the ns time scale was detected, indicating contributions from unquenched dyes. A likely origin of this signal are conformations where the dye is not located properly on the DNA base stack. For 4CAA and s6C<sub>Z</sub>AA, the amplitude of these components was highest, giving rise to doubts about the structural integrity of both systems with respect to the position of the rhodamine. For 4CAA, this is also reflected in a fluorescence depolarisation time between values for capped  $R6^+$  labeled duplexes and  $TMR^+$  free in solution. The other sequences with reduced  $R6^+$  lifetime showed amplitudes of the ns component in the order of 20%. This is in agreement with the result of NMR experiments, that a small percentage of rhodamines do not show resonances with bases.

In this context it is interesting to note that the lifetime of the ns component is not constant. The lifetime of the ns component is longest if the the electron donor is on the unmodified strand (s6CAA and s6C<sub>Z</sub>AA) and increases with donor-acceptor distance for duplexes, where G or Z is on the modified strand Table (5.5). A possible interpretation is a conformation where the dye is in contact with the hole acceptor in a non-capping position.

**6CAA:** In transient absorption experiments, the decay characteristics of 6CAA could be reasonably described by a biexponential function (Table 5.4). In fluorescence experiments the 468 ps decay component had to be separated into two components (Figure 5.23). This apparent contradiction of monoexponential versus biexponential decay can be explained by higher sensitivity of fluorescence experiments compared to transient absorption measurements in this time scale. As the time resolution is the same for ground state recovery, the same argument applies here. The origin of the biexponential decay of the excited state can either reflect an equilibrium between  $R6^{+*}/G$  and  $R6^{\bullet}/G^{\bullet}$  (i) or be due to conformational heterogeneity (ii):

(i) Equilibrium formation seems to be feasible, as the estimate of the driving force for charge injection to G points to an almost isoenergetic process



$\lambda_{\text{probe}}$	$\tau_1$	$A_1$	$\tau_2$	$A_2$	$\tau_3$	$A_3$	$\tau_4$	$A_4$
<b>6CAA</b>								
<b>Fl<sub>560 nm</sub></b>	—	—	<b>176 ps</b>	<b>31%</b>	<b>629 ps</b>	<b>47%</b>	<b>4.1 ns</b>	<b>22%</b>
<b>600 nm</b>	<b>5 ps</b>	<b>(9%)</b>	<b>468 ps</b>	<b>-87%</b>	—	—	<b>4.1 ns*</b>	<b>-23%</b>
<b>520 nm</b>	—	—	<b>406 ps</b>	<b>-74%</b>	—	—	<b>4.1 ns*</b>	<b>-26%</b>
<b>s6GAA</b>								
<b>Fl<sub>560 nm</sub></b>	—	—	<b>30 ps</b>	<b>71%</b>	<b>140 ps</b>	<b>11%</b>	<b>2.2 ns</b>	<b>18%</b>
<b>600 nm</b>	—	—	<b>55 ps</b>	<b>-31%</b>	<b>159 ps</b>	<b>-51%</b>	<b>2.2 ns*</b>	<b>-18%</b>
<b>520 nm</b>	—	—	<b>58 ps</b>	<b>-15%</b>	<b>116 ps</b>	<b>-62%</b>	<b>2.2 ns*</b>	<b>-23%</b>
<b>6GAA</b>								
<b>600 nm</b>	—	—	<b>80 ps</b>	<b>-52%</b>	<b>288 ps</b>	<b>-34%</b>	<b>3.7 ns</b>	<b>-14%</b>
<b>520 nm</b>	—	—	<b>100 ps</b>	<b>-55%</b>	<b>247 ps</b>	<b>-26%</b>	<b>3.7 ns</b>	<b>-19%</b>

**Table 5.4:** Decay constants and amplitudes as a result of best fit from fluorescence experiments and difference absorbance time traces for **stimulated emission** and **ground state recovery**

with  $\Delta G_{\text{FET}} = -0.03 \text{ eV}$  (Section 5.1.6). In this picture, the two components describe the establishment and decay of the equilibrium [96]. If this mechanism were dominant, the ground state should recover monoexponentially with the time constant for the decay of the equilibrium and radical absorption should be detectable in the difference absorbance spectrum. However, experiments showed no indication for radical absorption and kinetics of ground state recovery are clearly shorter than 600 ps. If an equilibrium is not formed even though FET is close to isoenergetic, BET must efficiently depopulate the radical state. This seems reasonable, since  $\Delta G_{\text{BET}}$  must be close to the  $E_{0,0}$  energy of  $\text{R6}^+$  of 2.25 eV and ET processes in the inverted region can be very fast.

(ii) The biexponential kinetic pattern is characteristic for different conformations. Simultaneous decay of the excited state and recovery of the ground state is assigned to a slow FET process and a faster BET process, so that the population of the radical product is small. This ratio of rates  $k_{\text{FET}}/k_{\text{BET}}$  is a fingerprint for a rate determining FET process followed by a faster, less activated BET. The assumption of two different conformations and consequently different electronic coupling between  $\text{R6}^+$  and the electron donor G is in agreement with the NMR structure (Section 5.1.4).

**6GAA, s6GAA:** The results of time resolved measurements for the 20 bp duplex 6GAA and the analogous 13 bp duplex s6GAA are presented in Table 5.4. The variation of time constants for both duplexes allows an estimate for the reliability of fits for kinetics in this time scale. The accuracy of multiexponential fits is the lower, the closer two time constants are. Both, fluorescence and transient absorption experiments in stimulated emission and ground state recovery exhibit a biexponential decay pattern on the ps time scale. These observations support mechanism (ii) for nearest neighbour charge injection between  $R6^{+*}$  and G.

As the energetics for 6CAA and s6GAA should be similar – and as a consequence the Franck Condon factor for both ET processes should be equal – the difference in rates is attributed to the electronic coupling. An approximate factor of 5 for both ps decay times of both 6CAA and s6GAA would correspond to a ratio in electronic coupling  $V_{s6GAA}/V_{6CAA} = \sqrt{5} = 2.2$ .

As shown in Table 5.5, the kinetic pattern of the  $R6^+$  modified DNA strands, where G has been replaced by Z, are different. Assuming similar electronic coupling for G and Z, the acceleration of the excited state decay is attributed to the increased driving force.

**s6ZAA:** In contrast to the analogous sequence s6GAA, the rates for s6ZAA are monoexponential in a range where transient absorption measurements are very sensitive to dispersive kinetics and the back transfer rate measured as the recovery of the ground state can be resolved. This phenomenon is also reflected as formation and decay of radical absorption (Figure 5.20).

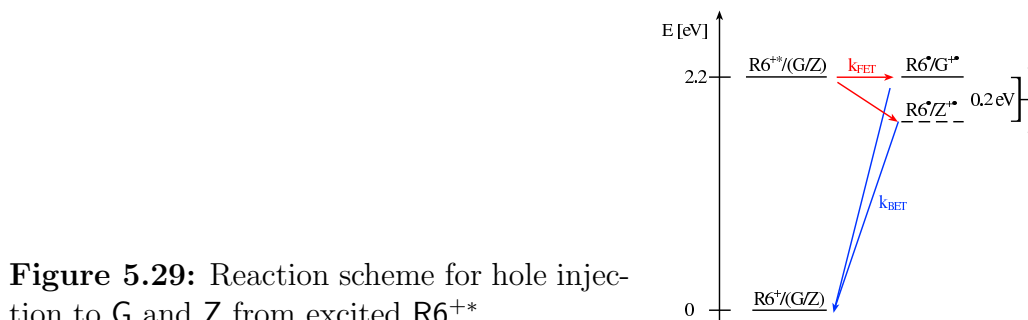


**Figure 5.29:** Reaction scheme for hole injection to G and Z from excited  $R6^{+*}$

As a rough approximation, the energetics of the ET processes can be estimated on the basis of the redox potentials for G and  $R6^+$  measured in solution. G oxidation by excited  $R6^+$  is almost isoenergetic, the difference in oxidation potential between G and Z  $\Delta\Delta G = 0.2$  eV has been determined *in situ*. For an approximate activation energy for hole injection in the sequence s6ZAA being 0, which seems to be a reasonable assumption for such a fast

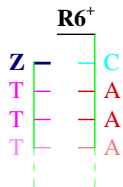
$\lambda_{\text{probe}}$	$\tau_1$	$A_1$	$\tau_2$	$A_2$	$\tau_3$	$A_3$	$\tau_4$	$A_4$
<b>s6C<sub>Z</sub>AA</b>								
600 nm	—	—	4.2 ps	-43%	—	—	4 ns*	-57%
520 nm	—	—	—	—	6.7 ps	-43%	4 ns*	-57%
<b>s6ZAA</b>								
600 nm	—	—	1.0 ps	-80%	—	—	2.8 ns	-20%
520 nm	—	—	—	—	5.2 ps	-76%	2.8 ns	-24%
<b>s6GAA</b>								
Fl <sub>560 nm</sub>	—	—	30 ps	71%	140 ps	11%	2.2 ns	18%
600 nm	—	—	55 ps	-31%	159 ps	-51%	2.2 ns*	-18%
520 nm	—	—	58 ps	-15%	116 ps	-62%	2.2 ns*	-23%
<b>s6AZA</b>								
Fluo	—	—	260 ps	24%	774 ps	47%	3.7 ns	29%
600 nm	—	—	—	—	595 ps	-56%	3.7 ns*	-44%
600 nm	—	—	5 ps*	-0.1%	595 ps	-56%	3.7 ns*	-44%
520 nm	—	—	7.8 ps	-8%	487 ps	-48%	3.7 ns*	-52%
<b>s6AGA</b>								
600 nm	—	—	—	—	—	—	3.8 ns	-100%
520 nm	—	—	—	—	—	—	3.8 ns	-100%
<b>s6AAZ</b>								
600 nm	—	—	—	—	—	—	4.9 ns	-100%
520 nm	—	—	—	—	—	—	4.9 ns	-100%

**Table 5.5:** Decay constants and amplitudes as a result of best fit from fluorescence experiments and difference absorbance time traces for **stimulated emission** and **ground state recovery**

rate, the reorganisation energy has to be in the order of the driving force  $\lambda_{\text{s6ZAA}} = -\Delta G \approx 0.2 \text{ eV}$  (Section 5.1.6).

Under these assumptions, the BET process can be assigned to the inverted region. Since a change of  $\Delta G_{\text{BET}}$  by  $\approx 0.2 \text{ eV}$  should not influence the rate significantly, the BET rate for s6ZAA can also serve as a crude estimate for the BET rate for 6GAA, confirming the interpretation of a fast depopulation of the radical.

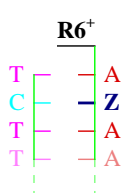
**s6C<sub>Z</sub>AA:** Surprisingly, the sequence s6C<sub>Z</sub>AA shows a very high contribution of non-reactive R6<sup>+</sup>. This can be an indication of weak structural stability with respect to the capping of the dye. The trend towards slower rates for the hole acceptor on the counterstrand reproduces the one observed for 6CAA and s6GAA. More detailed discussion is only possible on the basis of further experiments.



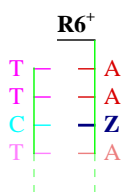
### Distance dependence of ET

**s6GAA-s6AGA:** A Comparison of the excited state lifetimes of R6<sup>+</sup> in s6GAA-s6AGA shows that insertion of one A : T base pair between the dye and G leads to a decrease of the ET rate by a factor of more than 100. Adopting the view of an electronic attenuation factor  $\beta = 0.6 - 0.7 \text{ \AA}^{-1}$  decreased electronic coupling leads to a slow down of rates by a factor of 10 to 14 and a remaining factor of at least 7-10 has to be attributed to the Franck Condon factor.

**s6AZA:** In contrast to G as ET partner for R6<sup>+</sup>, insertion of a A : T base pair between the dye and Z still allows an ET rate below the lifetime of the unquenched dye. With kinetics similar to 6CAA, the fluorescence measurements show two ps components which are again, for sensitivity reasons, not resolved in absorption. Ground state recovery shows a short 8.1 ps component. The origin of this component has to be caused by dyes not residing on the base stack, but in close vicinity to Z, potentially in one of the grooves of the duplex. If this component can be assigned to an ET process, an excited state decay on the same time scale could compensate the apparent increase of stimulated emission due to excited state relaxation. Time resolution of the fluorescence experiment is too low to identify this component. Similar to the other samples, biexponentiality of fluorescence decay on the ps time scale is interpreted as due to structural variation as discussed in detail above, following model (ii).



**s6AAZ:** A central aspect of the present experiments is the distance dependence of the reorganisation energy. Unfortunately, the oxidation of Z is too slow to reduce excited state lifetime of R6<sup>+</sup> in s6AAZ. The comparison of s6AZA and s6AAZ would have been of great importance as in both cases ET follows the superexchange mechanism. Even though experience on stilbene-modified DNA duplexes showed that also for the pair of nearest neighbour and next nearest neighbour charge transfer partners follow exponential distance dependence [97], comparison between s6AZA and s6ZAA is difficult as in one case (s6AZA) structural inhomogeneity is observable and in the other





case (s6ZAA) it is not. Obviously, the binding situations for both cases are different.

If we ignored these limitations, and compared the injection rate of s6ZAA with the fastest rate of s6AZA, they would differ by a factor of at least 260. An upper reasonable value for the decrease of electronic coupling over one A : T basepair is in the order of  $\sqrt{15} = 3.8$ , corresponding to an electronic attenuation parameter of  $\beta = 0.7 \text{ \AA}^{-1}$  for changed electronic coupling [97]. A remaining factor 17 has to be assigned to the Franck Condon factor. Based on a driving force of  $\Delta G = -0.2 \text{ eV}$  and activationless FET for s6ZAA, this corresponds to an activation energy for s6AZA of  $E_a = 56 \text{ meV}$  and a reorganisation energy of  $\lambda = 0.55 \text{ eV}$  as compared to  $\lambda = 0.2 \text{ eV}$  for s6ZAA.

As these considerations are partially based on very crude assumptions, they cannot be regarded as a definite support for a distance dependence of  $\lambda$ , but certainly, they do not contradict.



# Chapter 6

## Summary

In this work, mechanistic aspects of electron transfer (ET) reactions of two covalently linked molecular systems have been studied, applying fs to ns time resolved absorption and fluorescence techniques.

### Ferrocenophane-nileblue

The multiexponential charge recombination kinetics on a ps time scale of the covalently linked ferrocenophane-nileblue (FC – NB<sup>+</sup>) compound depends on an external magnetic field of up to 7 T and on temperature. Based on EPR data of this molecular system, the multiexponential kinetics could be modeled revealing an essentially monoexponential back ET (BET) process and spin relaxation time constants in a temperature range from 170 K to 295 K.

Based on these experiments, and on transient absorption experiments with a ultrahigh time resolution [27,48], following conclusions could be drawn:

1. Spin relaxation in FC – NB<sup>+</sup> occurs with a rate of  $k_S = (14.3 \text{ ps})^{-1}$  at 295 K and is almost activationless with  $E_a = 26 \text{ meV}$ . Based on the value of  $k_S$  at 295 K and, even more on the weak temperature dependence, the Orbach mechanism is supported, which explains spin relaxation as due to solvent fluctuations leading to a fluctuating electric field at the molecule.
2. Forward ET (FET) can be described by a rate of  $k_{\text{FET}} = (90 \text{ fs})^{-1}$  at 295 K; it does not drop below  $k_{\text{FET}} = (150 \text{ fs})^{-1}$  at 170 K. BET, as derived from the simulation of the magnetic field dependent recovery kinetics, is also essentially monoexponential with a rate of  $k_{\text{BET}} = (1.2 \text{ ps})^{-1}$  at 295 K and almost activationless with  $E_a = 24 \text{ meV}$ . Cyclovoltammetry under *in situ* conditions yields driving forces  $\Delta G_{\text{FET}} =$

$-1.4$  eV and  $\Delta G_{\text{BET}} = -0.5$  eV. As transitions from the  $\text{FC} - \text{NB}^{+*}$  reactant state to intermediate states can be ruled out, the ultrafast FET rate together with an extremely large  $\Delta G_{\text{FET}}$  cannot be explained by conventional ET theory.

3. Ultrafast sub-100 fs ET processes are possible with only one electron donor in close vicinity to the electron acceptor. This answers the question, whether ultrafast ET processes in systems where the solvent serves as one ET partner are due to one ET pair in preferred configuration or whether the multiplicity of ET partners is the cause of the fast ET rate.

In future experiments it might be interesting to study the influence of solvent properties and of the excitation wavelength on the FET step. This could help to develop qualitative models for ultrafast ET processes with large  $\Delta G$ .

### Rhodamine end-capping DNA

DNA strands with end-capped rhodamines have been studied by transient absorption and time resolved fluorescence techniques. From these studies, following conclusions could be drawn:

1. Results from time resolved spectroscopy can be related to NMR structures. It has been a central aspect of this work, and a novel approach, to compare NMR structures with the charge injection rates of identical modified DNA duplexes. NMR structures revealed two positions of rhodamine 6G ( $\text{R6}^+$ ) end-capping on a DNA base stack terminated by either a  $\text{C} : \text{G}$  or  $\text{G} : \text{C}$  base pair. This is reflected in a biexponential injection pattern. For  $\text{R6}^+$  end-capping on an  $\text{A} : \text{T}$  terminus followed by a  $\text{G} : \text{C}$  pair, NMR also indicated two conformations; charge injection could not be detected as the injection process is almost isoenergetic and the natural fluorescence lifetime of  $\text{R6}^{+*}$  is shorter than the expected ET time constant. On an equivalent duplex, where  $\text{G}$  is replaced by an easier to oxidize 7-deaza-guanine ( $\text{Z}$ ), charge injection, again, is biexponential. NMR structures have not been resolved in  $\text{Z}$  containing duplexes. Time resolved spectroscopy on duplexes with  $\text{R6}^+$  end-capping on a  $\text{C} : \text{Z}$  and on a  $\text{Z} : \text{C}$  terminus yielded monoexponential injection kinetics, indicating altered capping conditions.

NMR structures showed a small ( $< 15\%$ ) amount of non-capping  $\text{R6}^+$ . This is reflected in a ns background signal with a  $\sim 20\%$  amplitude.

Fluorescence depolarisation experiments showed, that this signal is due to dyes that are bound to the DNA strand, but are not endcapping the duplex.

2. Comparing sequences with Z in nearest neighbour (s6ZAA) and in next nearest neighbour (s6AZA) position to end-capping R6<sup>+</sup> yields a difference in injection rates by a factor of at least 250. Since one cannot compare electronic coupling for s6ZAA (where charge injection is mono-exponential) and s6AZA (where charge injection is biexponential) and temperature dependent measurements are not feasible, one cannot assign the difference in rates to the Franck Condon factor with similar accuracy as for DNA systems where 9-amino-6-chloro-2-methoxyacridine is intercalated into the base stack [23].

These results demonstrate that semi-endcapped DNA systems are structurally much less defined compared to systems where a dye is intercalated into the DNA base stack, although the B-DNA form of the duplex itself is not disturbed, in contrast to intercalated systems. This is of great importance for biotechnological applications. Without knowledge about structural inhomogeneity and changes of the structure for different binding situations, especially experiments based on the determination of fluorescence quantum yields can easily be misinterpreted.



# Bibliography

- [1] R. A. Marcus. On the Theory of Oxidation–Reduction Reactions Involving Electron Transfer. *J. Chem. Phys.*, 24:966 – 978, 1956.
- [2] V.O. Levich. Present State of the Theory of Oxidation–Reduction in Solution (Bulk and Electrode Reactions). *Adv. Electrochem.*, 4:249 – 371, 1966.
- [3] J. Jortner. Temperature dependent activation energy for electron transfer between biological molecules. *J. Chem. Phys.*, 64:4860–4867, 1976.
- [4] D. M. Adams, L. Brus, C. E. D. Chidsey, S. Creager, C. Creutz, C. R. Kagan, P. V. Kamat, M. Lieberman, S. Lindsay, R. A. Marcus, R. M. Metzger, M. E. Michel-Beyerle, J. R. Miller, M. D. Newton, D. R. Rolison, O. Sankey, K. S. Schanze, J. Yardley, and X. Zhu. Charge Transfer on the Nanoscale: Current Status. *J. Phys. Chem. B*, 107:6668–6697, 2003.
- [5] J. Jortner and M. Ratner, editors. *Molecular Electronics*. Blackwell Science, Cambridge (MA), 1997.
- [6] M. E. Michel-Beyerle, R. Haberkorn, W. Bube, E. Steffens, H. Schröder, H. J. Neusser, and E. W. Schlag. Magnetic field modulation of geminate recombination of radical ions in a polar solvent. *Chem. Phys.*, 17:139–145, 1976.
- [7] L. Banci, I. Bertini, and C. Luchinat. *Nuclear and Electron Relaxation. The Magnetic Nucleus-Unpaired Electron Coupling in Solution*. VCH Weinheim, New York, Basel, Cambridge, Tokyo, 1991.
- [8] U. E. Steiner and H.-J. Wolff. *Photochemistry and Photophysics, Volume IV*, chapter I: Magnetic Field Effects in Photochemistry. CRC Press, 1991.

- [9] K. M. Kleinschmidt, J. F. Dobson, and D. M. Doddrell. Vibronic Coupling and Spin Relaxation in Discrete Spin- $\frac{1}{2}$  Transition-Metal Complexes. *Chem. Phys. Lett.*, 68:115–120, 1979.
- [10] U. E. Steiner and D. Bürßner. Theoretical Treatment of Magnetic Field Dependent In-Cage Backward Electron Transfer during Photooxidation of Ru(II) Complexes. *Z. Phys. Chem. NF*, 1990.
- [11] P. Gilch, F. Pöllinger-Dammer, C. Musewald, M.E. Michel-Beyerle, and U.E. Steiner. Magnetic Field Effect on Picosecond Electron Transfer. *Science*, 281:982–984, 1998.
- [12] P. Gilch. *Pikosekunden-Spinchemie. Untersuchungen über die Abhängigkeit der Rekombinationskinetik Ferrocenium-haltiger Radikalpaare von starken Magnetfeldern.* Dissertation, Technische Universität München, 1999.
- [13] P. Gilch, M. Linsenmann, W. Haas, and U. E. Steiner. Magnetic Field Effect on the Photooxidation Efficiency of Ferrocene. *Chem. Phys. Lett.*, 254:139–145, 1996.
- [14] C. J. Murphy, M. R. Arkin, Y. Jenkins, N. D. Ghatlia, S. H. Bossmann, N. J. Turro, and J. K. Barton. Long-Range Photoinduced Electron Transfer Through a DNA Helix. *Science*, 262:1025–1029, 1993.
- [15] C. J. Murphy, M. R. Arkin, N. D. Ghatlia, S. H. Bossmann, N. J. Turro, and J. K. Barton. Fast photoinduced electron transfer through DNA intercalation. *Proc. Natl. Acad. Sci. U.S.A.*, 91:5315–5319, 1994.
- [16] P. J. Dandliker, R. E. Holmlin, and J. K. Barton. Oxidative Thymine Dimer Repair in the DNA Helix. *Science*, 275:1465–1468, 1997.
- [17] M. E. Nunez, D. B. Hall, and J. K. Barton. Long-Range Oxidative Damage to DNA: Effects of Distance and Sequence. *Chem. Biol.*, 6:85–97, 1999.
- [18] J. Jortner, M. Bixon, T. Langenbacher, and M. E. Michel-Beyerle. Charge Transfer and Transport in DNA. *Proc. Natl. Acad. Sci. U.S.A.*, 95:12759–12765, 1998.
- [19] B. Giese, S. Wesseley, M. Spormann, U. Lindermann, E. Meggers, and M. E. Michel-Beyerle. On the Mechanism of Long-Range Electron Transfer through DNA. *Angew. Chem. Int. Ed.*, 38:996–998, 1999.



- [20] F. D. Lewis, T. Wu, Y. Zhang, R. L. Letsinger, S. R. Greenfield, and M. R. Wasielewski. Distance-Dependent Electron Transfer in DNA Hairpins. *Science*, 277:673–676, 1997.
- [21] F. D. Lewis, T. Wu, X. Liu, R. L. Letsinger, S. R. Greenfield, S. E. Miller, and M. R. Wasielewski. Dynamics of Photoinduced Charge Separation and Charge Recombination in Synthetic DNA Hairpins with Stilbenedicarboxamide Linkers. *J. Am. Chem. Soc.*, 122:2889–2902, 2000.
- [22] K. Fukui and K. Tanaka. Distance Dependence of Photoinduced Electron Transfer in DNA. *Angew. Chem. Int. Ed.*, 37:158–161, 1998.
- [23] S. Hess, M. Götz, W. B. Davis, and M. E. Michel-Beyerle. On the Apparently Anomalous Distance Dependence of Charge-Transfer Rates in 9-Amino-6-chloro-2-methoxyacridine-Modified DNA. *J. Am. Chem. Soc.*, 123:10046–10055, 2001.
- [24] W. B. Davis, S. Hess, I. Naydenova, R. Haselsberger, A. Ogrodnik, M. D. Newton, and M. E. Michel-Beyerle. Distance-dependent activation energies for hole injection from protonated 9-amino-6-chloro-2-methoxyacridine into duplex DNA. *J. Am. Chem. Soc.*, 124:2422–2423, 2002.
- [25] Y. P. Liu and M. D. Newton. Solvent reorganization and donor/acceptor coupling in electron-transfer processes – self-consistent reaction field-theory and ab-initio applications. *J. Phys. Chem.*, 98:7162–7169, 1994.
- [26] M. Stöckl. *Synthese von 2-akzeptorsubstituierten [3]-Ferrocenophanen*. PhD thesis, Technische Universität München, 1999.
- [27] E. Baigar, P. Gilch, W. Zinth, M. Stöckl, P. Härter, T. von Feilitzsch, and M.E. Michel-Beyerle. Ultrafast intramolecular electron transfer from a ferrocene donor moiety to a Nile blue acceptor. *Chem. Phys. Lett.*, 352:176–184, 2002.
- [28] P. Bachert. *Zeitaufgelöste, transiente Absorptionsspektroskopie an Elektronentransfersystemen*. Diplomarbeit, Technische Universität München, 1995.
- [29] S. Wahl. *Aufbau eines fs-zeitaufgelösten Absorptionsmeßstands*. Diplomarbeit, Technische Universität München, 1995.
- [30] F. Pöllinger. *Studien zum Elektronentransfer in Cyclophan-verbrückten Porphyrin-Chinon-Systemen*. Dissertation, Technische Universität München, 1993.

- [31] A. Kummer. *Fluorescence Kinetics of the Green Fluorescent Protein (GFP)*. Dissertation, Technische Universität München, 2000.
- [32] R. A. Marcus and N. Sutin. Electron transfer in chemistry and biology. *Biochem. Biophys. Acta*, 811:265–322, 1985.
- [33] J. Jortner. *Electron Transfer - From Isolated Molecules to Biomolecules*. Wiley New York, 1999.
- [34] R.P. van Duyne and S. F. Fischer. A Nonadiabatic Description of Electron Transfer Reactions Involving Large Free Energy Changes. *Chem. Phys.*, 1974.
- [35] H. Heitele. Dynamische Lösungsmittelleffekte bei Elektronentransferreaktionen. *Angew. Chem.*, 105:378–398, 1993.
- [36] H. Heitele und M. E. Michel-Beyerle. *Antennas and Reaction Centers of Photosynthetic Bacteria - Structure, interaction and Dynamics*. Springer Verlag Berlin, 1985.
- [37] M. Bixon, M. E. Michel-Beyerle, J. Jortner, and A. Ogrodnik. A Superexchange Mechanism for the Primary Charge Separation in Photosynthetic Reaction Centers. *Biochem. Biophys. Acta*, 977:273–286, 1989.
- [38] J. Jortner. Dynamics of Electron Transfer in Bacterial Photosynthesis. *Biochem. Biophys. Acta*, 594:193–230, 1980.
- [39] A. Weller. Photoinduced Electron Transfer in Solution: Exciplex and Radical Ion Pair Formation - Free Enthalpies and their Solvent Dependence. *Z. Physik. Chem. NF*, 133:93–98, 1982.
- [40] K. Kumar, I. V. Kurnikov, D. N. Beratan, D. H. Waldeck, and M. B. Zimmt. Use of Modern Electron Transfer Theories to Determine Electronic Coupling Matrix Elements in Intramolecular Systems. *J. Phys. Chem. A*, 102:5529–5541, 1998.
- [41] H. L. Tavernier and M. D. Fayer. Distance Dependence of Electron Transfer in DNA: The Role of Reorganization Energy and Free Energy. *J. Phys. Chem. B*, 104:11541–11550, 2000.
- [42] P. F. Barbara, T. J. Meyer, and M. A. Ratner. Contemporary Issues in Electron Transfer Research. *J. Phys. Chem.*, 100:13148–13168, 1996.
- [43] N. J. Turro. *Modern Molecular Photochemistry*. Benjamin Cummings, Menlo Park, 1978.

- [44] K. Schulten, H. Staerk, A. Weller, H.-J. Werner, and B. Nickel. Magnetic Field Dependence of the Geminate Recombination of Radical Ion Pairs in Polar Solvents. *Z. Phys. Chem. NF*, 101:371, 1976.
- [45] U. E. Steiner and T. Ulrich. Magnetic Field Effect in Chemical Kinetics and Related Phenomena. *Chemical Reviews*, 89:51–147, 1989.
- [46] K. M. Salikhov, Y. N. Molin, R. Z. Sagdeev, and A. L. Buchachenko. *Spin Polarization and Magnetic Field Effects in Radical Reactions*. Elsevier, Amsterdam, 1984.
- [47] M. Volk, A. Ogrodnik, and M. E. Michel-Beyerle. *Anoxygenic Photosynthetic Bacteria*, pages 595–626. Kluwer Academic, Dordrecht, 1995.
- [48] E. Baigar. *Femtosekundenspektroskopie an Farbstofflösungen: Dynamischer Stokes Shift, Elektronentransfer und Wellenpaketbewegungen*. Dissertation, Universität München, 2003.
- [49] R. Prins. Electronic Structure of the Ferrocenium Cation. Electron Spin Resonance Measurements of the Cations of Ferrocene Derivatives. *Mol. Phys.*, 19:603–620, 1970.
- [50] M. Volk, P. Gilch, C. Kompa, R. Haselsberger, P. Härter, M. Stöckl, W. K. Latzel, and M.E. Michel-Beyerle. Carbonyl Spectator Bonds as Sensitive Sensors for Charge Transfer Reactions on the Femtosecond Time Scale. *J. Phys. Chem. A*, 104:4984–4988, 2000.
- [51] S. Tamura, K. Kikuchi, H. Kokubun, and A. Weller. Electron Transfer Reactions between Triplet Methylene Blue and Ferrocenes in Acetonitril. *Z. Phys.Chem. NF*, 121:165–175, 1980.
- [52] D. Bürßner. *Modellrechnungen zur Dynamik spinabhängiger Elektronentransferreaktionen mit Rutheniumkomplexen*. Diplomarbeit, Universität Konstanz, 1989.
- [53] K. A. Hötzer, A. Klingert, T. Klumpp, E. Krissinel, D. Bürßner, and U. E. Steiner. Temperature-Dependent Spin Relaxation: A Major Factor in Electron Backward Transfer Following the Quenching of  $^*Ru(bpy)_3^{2+}$  by Methyl Viologen. *J. Phys. Chem. A*, 106:2207 – 2217, 2002.
- [54] D. M. Doddrell, M. R. Bendall, D. T. Pegg, P. C. Healy, and A. K. Gregson. Temperature Dependence of Proton Spin-Lattice Relaxation Times in Some Paramagnetic Transition Metal Acetylacetonate Complexes. The Possible Influence of the Jahn-Teller Effect on Electron Spin Relaxation. *J. Am. Chem. Soc.*, 99:1281–1282, 1977.

- [55] R. C. Weast, editor. *Handbook of Chemistry and Physics*. CRC Press Inc., Cleveland, Ohio, 58th edition, 1977.
- [56] J. Barthel, K. Bachhuber, R. Buchner, and H. Hetzenauer. Dielectric spectra of some common solvents in the microwave region. Water and lower alcohols. *Chem. Phys. Lett.*, 165:369–373, 1990.
- [57] M. Bixon, J. Jortner, and J. W. Verhoeven. Lifetimes for Radiative Charge Recombination in Donor-Acceptor Molecules. *J. Am. Chem. Soc.*, 116:7349–7355, 1994.
- [58] I. R. Gould, R. H. Young, L. J. Mueller, and S. Farid. Mechanism of Exciplex Formation. Roles of Superexchange, Solvent Polarity, and Driving Force for Electron Transfer. *J. Am. Chem. Soc.*, 116:8176–8187, 1994.
- [59] I. R. Gould, R. H. Young, L. J. Mueller, A. C. Albrecht, and S. Farid. Electronic Structure of Exciplexes and Excited Charge-Transfer Complexes. *J. Am. Chem. Soc.*, 116:8188–8199, 1994.
- [60] H. Kandori, K. Kemnitz, and K. Yoshihara. Subpicosecond Transient Absorption Study of Intermolecular Electron Transfer between Solute and Electron-Donating Solvents. *J. Phys. Chem.*, 96:8042–8048, 1992.
- [61] Q.-H. Xu, G. D. Scholes, M. Yang, and G. R. Fleming. Probing Solvation and Reaction Coordinates of Ultrafast Photoinduced Electron-Transfer Reactions Using Nonlinear Spectroscopies: Rhodamine 6G in Electron-Donating Solvents. *J. Phys. Chem. A*, 103:10348–10358, 1999.
- [62] M. Seel, S. Engleitner, and W. Zinth. Wavepacket motion and ultrafast electron transfer in the system oxazine 1 in N,N-dimethylaniline. *Chem. Phys. Lett.*, 275:363–369, 1997.
- [63] B. Wolfseder, L. Seidner, W. Domcke, G. Stock, M. Seel, S. Engleitner, and W. Zinth. Vibrational coherence in ultrafast electron-transfer dynamics of oxazine 1 in N,N-dimethylaniline: simulation of a femtosecond pump-probe experiment. *Chem. Phys.*, 233:323–334, 1998.
- [64] B. Wolfseder and W. Domcke. Intramolecular electron-transfer dynamics in the inverted regime: quantum mechanical multi-mode model including dissipation. *Chem. Phys. Lett.*, 259:113–118, 1996.
- [65] J.-L. Mergny, A. S. Boutorine, T. Garestier, F. Belloc, M. Rougee, N. V. Bulychev, A. A. Koshkin, J. Bourson, A. V. Lebedev, B. Valeur, N. T.

- Thuong, and C. Helene. Fluorescence energy transfer as a probe for nucleic acid structures and sequences. *Nucl. Acids Research*, 22:920–928, 1994.
- [66] G. Vamosi, C. Gohlke, and R. M. Clegg. Fluorescence Characteristics of 5-Carboxytetramethylrhodamine Linked Covalently to the 5' End of Oligonucleotides: Multiple Conformers of Single-Stranded and Double-Stranded Dye-DNA Complexes. *Biophys. J.*, 71:972–994, 1996.
- [67] A. Dietrich, V. Buschmann, C. Müller, and M. Sauer. Fluorescence resonance energy transfer (FRET) and competing processes in donor-acceptor substituted DNA strands: a comparative study of ensemble and single-molecule data. *Rev. Mol. Biotech.*, 82:211–231, 2003.
- [68] S. Tyagi and F. R. Kramer. Molecular beacons: probes that fluoresce upon hybridization. *Nature Biotech.*, 1996.
- [69] L. G. Kostrikis, S. Tyagi, M. M. Mhlanga, D. D. Ho, and F. R. Kramer. Spectral genotyping of human alleles. *Science*, 1998.
- [70] D. Topygin, B. Z. Packard, and L. Brand. Resolution of absorption spectra of Rhodamine 6G aggregates in aqueous solution using the law of mass action. *Chem. Phys. Lett.*, 277:430–435, 1997.
- [71] S. Dare-Doyen, D. Doizi, Ph. Guilbaud, f. Djedaini-Pillard, B. Perly, and Ph. Millie. Dimerization of Xanthene Dyes in Water: Experimental Studies and Molecular Dynamic Simulations. *J. Phys. Chem. B*, 107:13803–13812, 2003.
- [72] C. R. Cantor and P. R. Schimmel. *Biophysical Chemistry, Part II: Techniques for the Study of Biological Structures and Function*. W. H. Freeman and Company, San Francisco, 1980.
- [73] A. A. Voityuk, J. Jortner, M. Bixon, and N. Rösch. Energetics of hole transfer in dna. *Chem. Phys. Lett*, 324:430–434, 2000.
- [74] C. A. M. Seidel, A. Schulz, and M. H. M. Sauer. Nucleobase-Specific Quenching of Fluorescent Dyes. 1. Nucleobase One-Electron Redox Potentials and Their Correlation with Static and Dynamic Quenching Efficiencies. *J. Phys. Chem.*, 100:5541–5553, 1996.
- [75] S. O. Kelley and J. K. Barton. DNA-mediated electron transfer from a modified base to ethidium:  $\pi$ -stacking as a modulator of reactivity. *Chem. Biol.*, 5:413–425, 1998.

- [76] C. Seidel. *Laserspektroskopische Untersuchungen molekularer Aspekte der nukleobasenspezifischen Löschung von Fluoreszenzfarbstoffen*. Dissertation, Ruprecht Karls Universität Heidelberg, 1992.
- [77] M. Raytchev, E. Pandurski, I. Buchvaroc, C. Modrakowski, and T. Fiebig. Bichromophoric Interactions and Time-Dependent Excited State Mixing in Pyrene Derivatives. A Femtosecond Broad-Band Pump-Probe Study. *J. Phys. Chem. A*, 107:4592–4600, 2003.
- [78] P. C. Beaumont, D. G. Johnson, and B. J. Parsons. Photophysical Properties of Laser Dyes: Picosecond Laser Flash Photolysis Studies of Rhodamine 6G, Rhodamine B and Rhodamine 101. *J. Chem. Soc. Faraday Trans.*, 89:4185–4191, 1993.
- [79] A. K. Pikaev, L. I. Kartasehva, N. S. Vinogradova, and V. V. Rylkov. Pulse Radiolysis of Solutions of Rhodamine Dyes. *Khimiya Vysokikh Energii*, 15:312–317, 1981.
- [80] T. Häberle. *Ultraschnelle Elektrontransferprozesse in künstlichen Donator/Akzeptor-Systemen und photosynthetischen Reaktionszentren*. Dissertation, Technische Universität München, 1995.
- [81] P. Plaza, D. Hung, M. M. Martin, Y. H. Meyer, M. Vogel, and W. Rettig. Ultrafast internal charge transfer in a donor-modified rhodamine. *Chem. Phys.*, 168:365–373, 1992.
- [82] J.-Y. Liu, W.-H. Fan, K.-L. Han, W.-Q. Deng, D.-L. Xu, and N.-Q. Lou. Ultrafast Vibrational and Thermal Relaxation of Dye Molecules in Solution. *J. Phys. Chem. A*, 107:10857–10861, 2003.
- [83] J. L. Dela Cruz and G. J. Blanchard. The Influence of Chromophore Structure on Intermolecular Interactions. A Study of Selected Rhodamines in Polar Protic and Aprotic Solvents. *J. Phys. Chem. A*, 106:10718–10724, 2002.
- [84] D. Magde, G. E. Rojas, and P. G. Seybold. Solvent Dependence of Fluorescence Lifetimes of Xanthene Dyes. *Photochem. Photobiol.*, 70:737–744, 1999.
- [85] T. Förster. *Fluoreszenz Organischer Verbindungen*. Vandenhoeck and Ruprecht, Göttingen, 1951.
- [86] Z. R. Grabowski, K. Rotkiewicz, A. Siemiarczuk, D. J. Cowley, and W. Baumann. Twisted intermolecular charge transfer states (TICT). A

- new class of excited states with a full charge separation. *Nouv. J. Chim.*, 3:443–454, 1979.
- [87] W. Rettig. Ladungstrennung in angeregten Zuständen entkoppelter Systeme – TICT-Verbindungen und Implikationen für die Entwicklung neuer Laserfarbstoffe sowie für den Sehvorgang und Photosynthese. *Angew. Chem.*, 98:969–986, 1986.
- [88] K. A. Zachariasse, T. von der Haar, A. Hebecker, U. Leinhos, and W. Kühnle. Intramolecular charge transfer in amino-benzonitriles: requirements for dual fluorescence. *Pure Appl. Chem.*, 65:1745–1750, 1993.
- [89] T. von der Haar, A. Hebecker, Y. Il'ichev, Y. B. Jiang, W. Kühnle, and K. A. Zachariasse. Excited-state intramolecular charge transfer in donor/acceptor-substituted aromatic hydrocarbons and in biaryls. The significance of the redox potentials of the D/A subsystems. *Recl. Trav. Chim. Pays-Bas*, 114:430–442, 1995.
- [90] F. L. Arbeloa and K. K. Rohatgi-Mukherjee. Solvent effects on the photophysics of the molecular forms of rhodamine B. Internal conversion mechanism. *Chem. Phys. Lett.*, 129:607–614, 1986.
- [91] F. L. Arbeloa, T. L. Arbeloa, M. J. T. Estevez, and I. L. Arbeloa. Photophysics of rhodamines. Molecular structure and solvent effects. *J. Phys. Chem.*, 95:2203–2208, 1991.
- [92] T. L. Arbeloa, M. J. T. Estevez, F. L. Arbeloa, I. U. Aguirresacona, and I. L. Arbeloa. Luminescence properties of rhodamines in water/ethanol mixtures. *J. Lumin.*, 48–49:400–404, 1991.
- [93] S. Bergamesco, G. Calzaferri, and K. Hädener. Solute-solvent relaxation of electronically excited xanthene dyes. *J. Photochem. Photobiol. A. Chem.*, 53:109–125, 1990.
- [94] A. Penzkofer and W. Leupacher. Fluorescence Behaviour of Highly Concentrated Rhodamine 6G Solutions. *J. Lumin.*, 27:61–72, 1987.
- [95] T. Y. Ohulchanskyy, D. J. Donnelly, M. R. Detty, and P. N. Prasad. Heteroatom Substitution Induced Changes in Excited-State Photophysics and Singlet Oxygen Generation in Chalcogenoxanthylum Dyes: Effect of Sulfur and Selenium Substitutions. *J. Chem. Phys. B.*, 108:8668–8672, 2004.

- [96] H. Heitele, F. Pöllinger, T. Häberle, M. E. Michel-Beyerle, and H. A. Staab. Energy Gap and Temperature Dependence of Photoinduced Electron Transfer in Porphyrin-Quinone Cyclophanes. *J. Phys. Chem.*, 98:7402–7410, 1994.
- [97] F. D. Lewis, R. S. Kalgutkar, Y. Wu, J. Liu, R. T. Hayes, S. E. Miller, and M. R. Wasilewski. Driving Force Dependence of Electron Transfer Dynamics in Synthetic DNA Hairpins. *J. Am. Chem. Soc.*, 122:12346 – 12351, 2000.



# List of publications

## Contributions to journals

1. Weicherding, D; Davis, WB; Hess, S; von Feilitzsch, T; Michel-Beyerle, ME; Diederichsen, U  
Femtosecond time-resolved guanine oxidation in acridine modified alanyl peptide nucleic acids  
*Bioorg. Med. Chem. Lett.*, 14: 1629-1632, 2004
2. Baigar, E; Gilch, P; Zinth, W; Stockl, M; Härter, P; von Feilitzsch, T; Michel-Beyerle, ME  
Ultrafast intramolecular electron transfer from a ferrocene donor moiety to a Nile blue acceptor  
*Chem. Phys. Lett.*, 352: 176-184, 2002
3. Schüttrigkeit, TA; Zachariae, U; von Feilitzsch, T; Wiehler, J; von Hummel, J; Steipe, B; Michel-Beyerle, ME  
Picosecond time-resolved FRET in the fluorescent protein from *Discosoma Red* (wt-DsRed)  
*ChemPhysChem*, 2: 325-328, 2001
4. Rückmann, I; Zeug, A; von Feilitzsch, T; Röder, B  
Orientational relaxation of pheophorbide-a molecules in the ground and in the first excited state measured by transient dichroism spectroscopy  
*Opt. Commun.*, 170: 361-372, 1999

## Contributions to conferences

1. von Feilitzsch, T; Michel-Beyerle, ME  
On the distance dependence of charge carrier injection into duplex DNA  
Talk at *International Workshop on Advances in Molecular Electronics: From Molecular Wires to Single Molecule Devices*, Dresden, 2004
2. von Feilitzsch, T; Michel-Beyerle, ME  
Medium Reorganization Energy and Hole Injection Dynamics in DNA  
Talk at *6th International Symposium of the Volkswagen-Stiftung on Intra- and Intermolecular Electron Transfer*, Cologne, 2003
3. von Feilitzsch, T; Härter, P; Gilch, P; Michel-Beyerle, ME  
Electronic Coupling of Forward and Back Electron Transfer in Bridged Ferrocene/Nileblue Donor/Acceptor System  
Poster presentation at *6th International Symposium of the Volkswagen-Stiftung on Intra- and Intermolecular Electron Transfer*, Cologne, 2003
4. von Feilitzsch, T; Härter, P; Gilch, P; Michel-Beyerle, ME  
Electronic Coupling of Forward and Back Electron Transfer in Bridged Ferrocene/Nileblue Donor/Acceptor System  
Poster presentation at *Spectroscopy of nano-size particles and nano-surfaces: Femtobiology, single molecule spectroscopy, correlation spectroscopy - applications and promises*, Aalborg, 2003
5. von Feilitzsch, T  
Magnetic Field Effect on Picosecond Electron Transfer Processes in Solution  
Talk at *TMR-Meeting*, Venice, 2003
6. Gilch, P; Baigar, E; Zinth, W; Stockl, M; Härter, P; von Feilitzsch, T; Michel-Beyerle, ME  
How Fast is the Ultrafast Electron Transfer in Solute-Solvent Systems?  
Poster presentation at *Ultrafast Phenomena XIII*, published in: *Ultrafast Phenomena XIII, Proceedings of the 13th International Conference*, R.D. Miller, M.M. Murnane, N.F. Scherer, A.M. Weiner (Eds), Springer, Berlin, 2002, pp: 437-440

# Acknowledgements

This work would not have been possible without the help and support of many. In particular, I am grateful to:

**Prof. M.-E. Michel-Beyerle** not only for giving me the great opportunity to join her in the labs, but also for her constant and very generous support and for her enthusiasm in developing ever new ideas in science.

**Dr. Peter Gilch** for his efforts in communicating to me the concepts of spin-chemistry and not giving up on discussing the results of the magnetic field dependent experiments with me.

**Prof. R. A. Marcus** for giving me the opportunity to discuss with him the ultrafast charge transfer in the ferrocenophane-nileblue system in depth.

**Prof. C. Griesinger** and **Dr. Heike Neubauer** for the cooperation on the DNA project. Only with their constant readiness to discuss their NMR results with us, it was possible to join the results of our very different experimental approaches.

**PD Peter Härter** for the synthesis of the ferrocenophane-nileblue system and support in chemistry, which is - for me - still close to “black magic”.

**Prof. N. Rösch** and **Prof. A. Voityuk** for quantumchemical calculations on the DNA system.

**Prof. Torsten Fiebig** and **Anton Trifonov** for white light probe difference absorption spectra on rhodamine labeled DNA strands. **Prof. J. Ulstrup** and **Dr. Chi Qijin** for the thorough electrochemical characterisation of the ferrocenophane-nileblue system.

**Dr. Olav Schiemann** for the EPR experiments on the ferrocenophane-nileblue system.

**Dr. Erik Baigar** for communicating his results on the ferrocenophane-nileblue system.

**Dr. Christian Kompa** for ingenious inventions, a lot of help on experimental, computational and scientific problems and many Kirschtaschen; **Dr. Tanja Schüttrigkeit** for endless support on the fluorescence machine and the coffee and tea.

**PD Reiner Feick, Dr. Mirco Götz, Dr. Gagik Gurzadyan, Dr. Reinhard Haselsberger, Dr. Stephan Hess, Dr. Andreas Kummer** and **PD Alexander Ogrodnik** for all the help, discussions and the nice working atmosphere.

**Gabriele Dietrich** for her friendship and for giving us the chance to learn how well an office can be organized.

**Wolfgang Reuther** for carefully reading this manuscript.

Life is more than science. During this work I learned to love my partner **Brigitte Voit**. I am grateful for her patience and support. Last, but not least, I wish to thank my parents **Dietlind** and **Christoph von Feilitzsch** and my brother **Mark**. During all my studies I could count on their help and – not only financial – support.